DOWNWARD INFLUENCE OF STRATOSPHERIC FINAL WARMING EVENTS IN AN IDEALIZED MODEL

BY

LANTAO SUN

DISSERTATION

Submitted in partial fulfillment of the requirements
for the degree of Doctor of Philosophy in Atmospheric Sciences
in the Graduate College of the
University of Illinois at Urbana-Champaign, 2010

Urbana, Illinois

Doctoral Committee:

Professor Walter A. Robinson, Chair
Harry E. Preble Endowed Professor Donald J. Wuebbles
Emeritus Professor Mankin Mak
Assistant Professor Somnath Baidya Roy

Abstract

The stratospheric final warming is the final transition of the zonal winds from wintertime westerlies to summertime easterlies as the solar heating of the high latitude stratosphere increases in the springtime. Recent observational analyses suggested that stratospheric final warming makes a significant contribution to the spring transitions in the lower troposphere, especially in the Northern Hemisphere. It is still not clear, however, whether these transitions are due to the downward influence from the stratosphere.

We first explore the hypothesis that much of the observed tropospheric signal of the final warming is initiated from the stratosphere. Large ensembles of final warmings are simulated in an idealized dynamical core model, by imposing a radiative equilibrium temperature transition from winter to summer only in the stratosphere. Our results suggest that a substantial fraction of the observed tropospheric changes that occur in conjunct with the final warming are induced from the stratosphere.

We further investigate the mechanisms of the downward influence of the final warmings on the tropospheric circulation. Results from our zonally symmetric model suggest that stratospheric wave driving can induce a residual circulation and affect the tropospheric circulation. The tropospheric signals due to this mechanism are, however, very weak and are mostly confined to the upper troposphere. On the other hand, the stratosphere can affect the propagation of planetary waves from the troposphere, resulting in a burst of wave activity and the zonal wind deceleration prior to the final warming in the troposphere.

We also perform a series of perturbation experiments for the sudden and final warmings to test the roles of the troposphere and the stratosphere in determining the predictability of stratospheric warmings. For a late final warming, almost all of the predictability comes from the troposphere. For the rest of the final warmings and for sudden warmings, however, the troposphere determines the predictability until very close to the time of warming onset. This finding, consistent with the conventional view of the warming, reflects that center role of the troposphere in determining the stratospheric warmings.

Results from a comprehensive global climate model, the Whole-Atmosphere Community Climate Model (WACCM), are used to analyze the final warmings in both hemispheres. Although WACCM has zonal winds that are too strong in the spring, which causes the mean onset dates to be delayed at least one month with respect to the observations, the zonal wind evolutions resemble the observations. The similarity between the models and observations suggests that the downward influence of the stratospheric final warming on the tropospheric circulation is real and substantial, especially in the Northern Hemisphere.

To father and mother.

Acknowledgments

This project would be impossible without the support of many people. First, I would like to thank my advisor, Walter A. Robinson, who gives me a lot of guidance in the research. Walter provides me unflinching encouragement and support in various ways. His true scientist intuition has made him as a constant oasis of ideas and passions in sciences, from which I benefit a lot. I am indebted to him more than he knows.

Also, I want to thank my committee members, Donald J. Wuebbles, Mankin Mak, and Somnath Baidya Roy for their valuable suggestions on my thesis. I appreciate greatly the discussions with Gang Chen (Cornell), Robert Black (Gatech). I get diagnose codes of the dynamical core and detailed descriptions from Yucheng Song (NCEP). I also acknowledge academic advices from directors of graduate studies in the past years, Bob Rauber, Larry Di Girolamo, Greg McFarquhar. I would never forget my master's advisor, Huiding Wu (NMEFC), who first led me into the world of stratosphere and still gives me helps now.

During my graduate study, I get a lot of helps from my fellow students in my department, Lijuan Wu, Zhenhua Li, Xian Lu and so on. I also want to thank my friends Qu Wu and Gang Chen, who help a lot when I have a hard time. Last, I would like to thank my families, especially my wife, who accompanies me living through the past several unique years at University of Illinois. Without any of my families, my life will be nothing.

This study is supported by the National Science Foundation (NSF) climate and large-scale dynamical program under grant ATMS-0456157. Any opinion, findings, and conclusions or recommendations expressed in this material do not necessarily reflect the views of the NSF.

Table of Contents

Chapter 1

Introduction

1.1 Introduction

1.1.1 The stratosphere

Earth's atmosphere is divided into layers according to their different temperature gradients. In the troposphere, the layer nearest Earth's surface, the temperature decreases with height. Above the tropopause, until near 50 km altitude, the temperature increases with height, primarily due to the absorption of solar ultraviolet radiation by ozone. This layer is called the stratosphere. Ever since the stratosphere was first discovered in data from balloon observations, in 1903 (Labitzke and Loon, 1999), it has attracted more and more attention from scientists, especially after 1980s when the "ozone hole" was discovered in the Antarctic (Farman et al., 1985). The Montreal Protocol and its Amendments have restricted the production and release of chlorofluorocarbons and other ozone depleting substances, and the stratospheric ozone layer is expected to return to its pre-1980s strength around 2060 - 2075 (WMO, 2006). The study of the stratosphere, however, is not only about ozone, the stratosphere and troposphere are connected dynamically. Planetary-scale Rossby waves from the troposphere reach the stratosphere and affect the zonal wind through wave-mean flow interaction, while the stratosphere influences the troposphere through a variety of mechanisms such as the "downward control" principle (Haynes et al., 1991).

Andrews et al. (1987) used the term of "middle atmosphere" to represent the region from the tropopause (10 - 16 km) to the homopause (110 km), where turbulent eddies produce a nearly uniform mixture of major chemical constituents and where ionization is not important.

As the lowest layer of the middle atmosphere, the stratospheric circulation is also different from that in the troposphere. The winter polar stratosphere is characterized by a huge cold vortex largely isolated from the mid-latitudes. In the summer, however, due to the increased absorption of solar radiation, the stratospheric zonal winds become easterly, and there is a high-pressure center over the pole. The summer stratosphere is quiet, but the winter polar vortex is often perturbed, especially in the Northern Hemisphere.

Consider, first, the geopotential height Φ. By applying Fourier analysis in the longitudinal direction, the geopotential height can be expanded in zonal harmonics,

$$\Phi = A_0(\phi, z) + \sum_{s=1}^{S} A_s(\phi, z) \cos[s\lambda + \alpha_s(\phi, z)]$$

where A_s represents the amplitude of each wave number, α_s is its phase, and A_0 is the zonal mean component (zonal wave number 0). The tropospheric circulation includes both long and short wave numbers, but in the stratosphere only the long waves (wave numbers 1-3) are present. Charney and Drazin (1961) derived the propagation criteria for vertically propagating Rossby waves. Under quasi-geostrophic β plane approximation, vertical propagation occurs only when,

$$0 < \bar{u} - c < \bar{u}_c \equiv \beta(k^2 + l^2 + \epsilon/4H^2)^{-1}$$

where $\bar{u}$ is the zonal mean zonal wind, c is the phase speed of the waves, k, l are the wave numbers in x, y direction. $\epsilon = f_0^2/N^2$ and H is the scale height. Stationary vertically propagating Rossby waves only exist in zonal winds that are westerly and not too strong. Considering a typical stratospheric state, it is estimated in Andrews et al. (1987) that $\bar{u}_c \approx 110/(s^2 + 3)$ m s^{-1} where s is the zonal wave number. Only the longest waves reach the stratosphere and interact with its circulations. This theory is supported by the observations that only planetary-scale waves exist in the winter stratosphere and that the summer stratosphere is quiet and nearly in radiative equilibrium.

1.1.2 Stratospheric vacillations and warmings

The sources of Rossby waves are in the troposphere. Short waves, such as synoptic-scale weather systems, are excited by baroclinic instability. Although these baroclinic eddies cannot reach the stratosphere, because of their small spatial-scales, they can force longer waves through nonlinear interactions. In the Northern Hemisphere, planetary waves are generated primarily by large-scale zonal asymmetries in topography and land-sea contrasts. In the Southern Hemisphere, however, these geographic forcings are relatively weak; nonlinear forcing by tropospheric baroclinic eddies is more important and contributes to the week-to-week variability of the stratosphere. For example, Scinocca and Haynes (1998) used an idealized primitive equation model to investigate the nonlinear long-wave forcing mechanism and the variability it can induce in the winter stratosphere. They suggested that tropospheric baroclinic wave packets might be an important mechanism for forcing higher-frequency wave number 2 disturbances observed in the Southern Hemisphere stratosphere.

The interaction between planetary waves and the mean flow in the stratosphere is complex. Planetary waves can break and destroy the mean flow; on the other hand, their upward propagation also depends on the mean flow (e.g. Charney-Drain criteria). Holton and Mass (1976) used a one-dimensional quasi-geostrophic β-plane channel model to study the wave-mean flow interaction. They found that when the wave forcing is sufficiently weak the stratospheric circulation is steady and very close to radiative equilibrium, but when the tropospheric wave forcing is greater than a threshold value, the mean flow and eddies oscillate quasi-periodically, even though the forcing is steady. More modeling work by Yoden (1987) and Christiansen (2000) revealed the nonlinear bifurcation properties of stratospheric vacillation. The mechanism of the stratospheric vacillation can be understood as the downward extension of the wave critical layer (Christiansen, 1999). In the Holton-Mass model, it is clear that when the tropospheric wave forcing is strong enough, the wintertime stratospheric zonal winds can undergo frequent decelerations from westerly to easterly; this is the so-called stratospheric sudden warming.

Scherhag (1952) first observed the sudden warming in radiosonde observations over Berlin. According to World Meteorological Organization (WMO) criteria, an event is defined as a major sudden warming if the zonal mean temperature at or below 10 hPa increases poleward from 60° latitude and if the zonally averaged zonal wind reverses its signs. If only the temperature gradient reverses, but the zonal winds do not, an event is defined as a minor sudden warming. Most major sudden warmings occur in the Northern Hemisphere during middle or late winter, with an approximate frequency of 0.6 events per year (Charlton and Polvani, 2006). In the Southern Hemisphere, only one major sudden warming was observed, in September 2002 (Scaife et al., 2005). In a typical sudden warming, polar stratospheric temperatures increase dramatically: say 40 - 60 K within one week at 10 hPa. It is now well accepted that sudden warmings are caused by the interaction between upward propagating planetary waves and the mean flow. This was first proposed by Matsuno (1971), who used a quasi-geostrophic model to test this mechanism. Our understanding of the details of the sudden warming, such as its precursors and predictability is still incomplete.

In addition to the sudden warming, the stratosphere experiences a final collapse of the polar vortex in the spring as solar heating increases. This final collapse appears as a polar warming and the reversal of zonal winds from wintertime westerlies to summertime easterlies. It is called the stratospheric final warming. In Fig. 1.1, the final warming is evident in April in the Northern Hemisphere in the seasonal transition of climatological observed high-latitude zonal mean zonal winds and temperatures. Unlike the sudden warming, the final warming occurs every year in both hemispheres. Also unlike the sudden warming, the easterly zonal winds after the final warming do not return to westerly until the fall, when the radiative cooling finally causes the temperature to decrease; this is the so-called stratospheric final cooling. Many studies have focused on the timing of the final warmings (e.g. Waugh and Rong (2002)) because it is important for understanding chemical processes inside the polar vortex during the spring. Recent observational analyses have suggested that the final warming contributes significantly to the spring transition in the lower troposphere, especially in the Northern Hemisphere (Black et al., 2006; Black and McDaniel, 2007a).

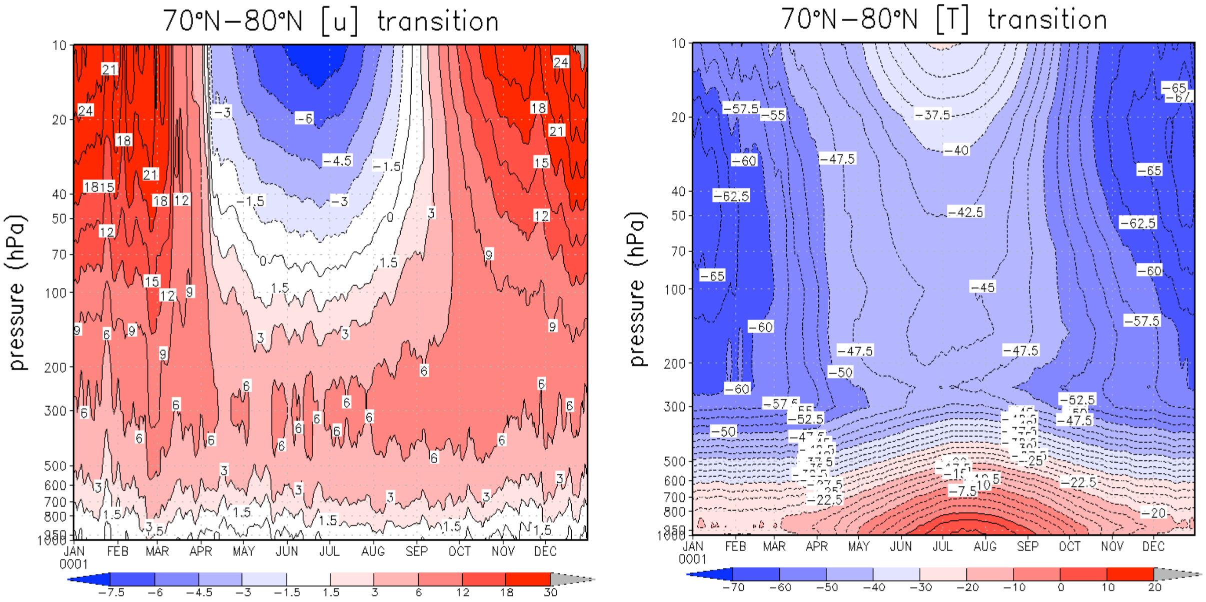

Figure 1.1: Climatological zonal-mean (left) zonal wind and (right) temperature evolutions in the Northern Hemisphere. Both the zonal wind and temperature are averaged from 70°N to 80°N. The wind contour interval is 1.5 m s^{-1} below 3 m s^{-1}, 3 m s^{-1} above that. The temperature contour interval is 2.5 K. Adopted from the NCEP/NCAR reanalysis dataset.

1.1.3 Connection between the stratosphere and the troposphere

The stratosphere and troposphere are closely linked by vertically propagating planetary waves. The distribution of planetary wave activity and, therefore the wave-mean flow interaction in the stratosphere depend on the sources in the troposphere. The sudden warming, the subseasonal break down of the stratospheric polar vortex during middle/late winter, is induced by upward propagation of tropospheric planetary waves. The final warming, by contrast, is mainly caused by solar heating, but waves also play an important role in driving its zonal wind deceleration, especially in the Northern Hemisphere (Black et al., 2006; Black and McDaniel, 2007a). Models and observations indicate a strong heat flux at 100 hPa precedes the sudden warming (Polvani and Waugh, 2004) and the final warming (Sun and Robinson, 2009) in the stratosphere. Recent studies on the links between tropospheric blocking and sudden warming events by Martius et al. (2009) revealed that blocking events are precursors to sudden warmings. At the same time, however, Mattewman (2009) used a single-layer quasi-geostrophic model to argue that if the stratospheric climate and planetary waves evolve slowly, for example due to seasonal cycle, sudden warming can occur even without an anomalous tropospheric planetary wave source.

For many years, the stratosphere was regarded as the passive recipient of influences from the troposphere. Recent observations, however, have revealed that both the sudden and final warmings in the stratosphere may influence the tropospheric circulation (e.g.: Limpasuvan et al. (2004); Black et al. (2006)). The annular mode, which is defined as the leading empirical orthogonal function (EOF) of the geopotential height, has provided a good diagnostic of the links between the stratospheric polar vortex and tropospheric climate (Thompson and Wallace, 2000). The stratospheric annular mode characterizes the strength of the polar vortex. In the troposphere, the surface annular mode is called the Arctic Oscillation (AO), and North Atlantic Oscillation (NAO) in the Atlantic region. Observational analyses indicate that changes in the stratospheric annular modes are precursors for some tropospheric anomalous weather regimes (Baldwin and Dunkerton, 2001) and could contribute to the tropospheric weather forecast (Baldwin et al., 2003). Understanding the physical mechanisms of this downward influence is essential if this effect is to be exploited.

1.2 Motivations and hypotheses

1.2.1 Stratospheric influence on the tropospheric circulation

Most of the observational evidence of stratospheric influence on the tropospheric circulation relate to the weakening (e.g. sudden warming and final warming) and strengthening of the polar vortex. Baldwin and Dunkerton (2001) calculated the annular mode index in the Northern Hemisphere using 42 years of data. They defined the stratospheric weak and strong vortex “events” using 10-hPa thresholds of -3.0 and +1.5. It was found that during the 60 days after these events, the surface pressure pattern closely resembles that of the Arctic Oscillation. The weak and strong vortex events also precede a shift in the probability distribution of extreme values of Arctic Oscillation and North Atlantic Oscillation, the location of storm tracks, and the likelihood of mid-latitude storms. This suggests that circulation anomalies in the stratosphere can be used to predict tropospheric weather regimes. The downward influence itself, however, is complex. Some stratospheric signals that can have an impact on the troposphere are also affected by the troposphere. Fletcher et al. (2007) used a General Circulation Model (GCM) to show that the thermal forcing from snow cover in Siberia can transmit signals up to the stratosphere and then back to the surface on timescales of weeks. The response depends on the state of the stratosphere prior to the initial forcing, but the source comes from the troposphere, not the stratosphere. Plumb and Semeniuk (2003) found that the stratospheric response to time-varying planetary waves takes the form of a downward migration, and they argued that the downward migration of the Arctic Oscillation (Baldwin and Dunkerton, 2001) might not imply any stratospheric forcing. They did not, however, rule out the possibility that the stratospheric perturbations due to stratospheric changes, ozone depletion say, could influence the troposphere. Hardiman (2006) made a distinction between the downward phase propagation due to a disturbance in the troposphere and downward group propagation in the stratosphere. The former downward influence, like that discussed by Plumb and Semeniuk (2003) and Fletcher et al. (2007), although important as a predictor of tropospheric change, may be influenced by conditions within the troposphere itself, while the real (information) downward influence is independent of tropospheric conditions, until the stratospheric disturbance reaches the troposphere.

Even if the stratosphere influences the tropospheric circulation, not all stratospheric events extend downward into the troposphere (e.g. Plate 2 in Baldwin and Dunkerton (1999)). Black and McDaniel (2004) did some diagnostic case studies for stratospheric annular mode events and suggested that whether or not the stratospheric influence reaches the troposphere depends on (i) whether the stratospheric potential vorticity (PV) anomalies descend to sufficiently low altitudes within the stratosphere and (ii) the preexisting state of the tropospheric annular modes.

Black et al. (2006); Black and McDaniel (2007b) used National Centers for Environmental Predication / National Centers for Atmospheric Research (NCEP/NCAR) re-analysis and

European Centre for Medium-Range Weather Forecasts re-analysis (ERA-40) dataset to study the influence of the stratospheric final warming events on the tropospheric circulation in the Northern and Southern Hemispheres. As shown in Fig. 1.2, the Northern Hemisphere has a coherent pattern of significant zonal wind anomalies (defined as deviations from the climatological seasonal cycle) in the high-latitude stratosphere extending downward to the surface. In the Southern Hemisphere, however, only marginally significant anomalies are observed in the troposphere. These observational analyses suggest that the stratospheric final warming makes a significant contribution to the springtime transition in the lower troposphere, especially in the Northern Hemisphere. The springtime transition is complex, however, and it is not possible, in observations, to unambiguously separate stratospheric influence from those governed by tropospheric processes alone. In a model, it is possible to induce a spring transition - a final warming - only in the stratosphere, and the resulting tropospheric changes are then unquestionably attributed to the stratospheric influence. In other words, only in a model it is possible to perform a clean test of the hypothesis, which is supported by strong, though circumstantial, observational evidence, that **much of the observed tropospheric signal in the final warming is initiated from the stratosphere**. This is our first motivation for the present study. Considering such simulations with different topographic forcing can reveal the possible different patterns of downward influence, like those observed in the Southern and Northern Hemispheres.

1.2.2 Mechanisms of the downward influence

In support of the observations of the downward influence from the stratosphere, many numerical modeling experiments have demonstrated a tropospheric response to the circulation anomalies imposed at stratospheric levels (e.g., Chen and Robinson (1992); Kushner and Polvani (2004); Song and Robinson (2004)). Several possible mechanisms have been proposed to explain how the stratosphere can affect the tropospheric circulation. One such mechanism is associated with the reflection and refraction of planetary waves. Chen and Robinson (1991) use a linear time-dependent, primitive equation model to investigate the

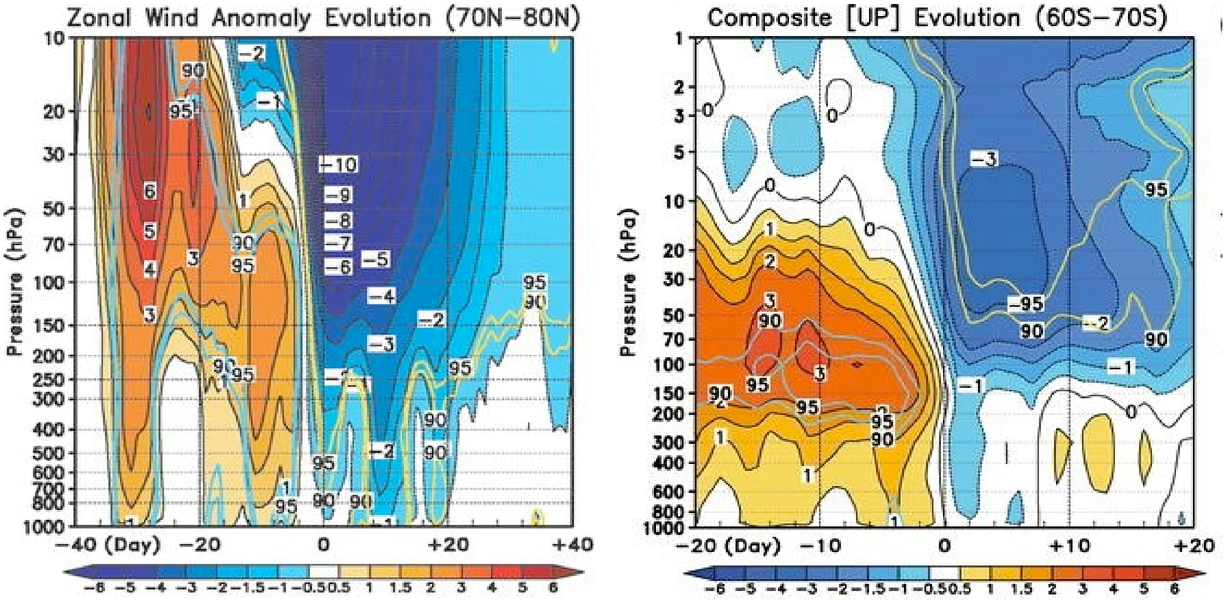

Zonal Wind Anomaly Evolution (70N–80N)

Composite [UP] Evolution (60S–70S)

Figure 1.2: Time evolution of the zonal mean zonal wind anomalies with respect to the final warming onset for (left) Northern Hemisphere and (right) Southern Hemisphere. The zonal mean zonal wind anomalies are defined as the deviation from the climatological seasonal transition and averaged from 70°N to 80°N in the Northern Hemisphere and 60°S to 70°S in the Southern Hemisphere (Shading: m/s). Colored contours indicate the 90% and 95% confidence levels for a two-sided Student's t test. Left figure comes from Black et al. (2006), right figure comes from Black and McDaniel (2007b). (c)American Meteorological Society. Reprinted with permission.

propagation of planetary waves and found two maxima in the convergence of Eliassen-Palm (E-P) flux (which indicates the flux of wave activity): one in high latitudes below the stratospheric polar jet associated with the dissipation of planetary waves, and the other in low latitudes due to the absorption of the planetary waves. Further studies by Chen and Robinson (1992) revealed that the tropopause acts as a valve for tropospheric planetary waves; the wind shear and jump in buoyancy frequency (N^2) determine the refractive index at the tropopause, and therefore affect the propagation of waves into the stratosphere. Baldwin and Dunkerton (1999) suggested that the downward propagation of annular mode anomalies might involve the modulation of the wave-guide for planetary waves through anomalies in the high-latitude zonal flow. Perlwitz and Harnik (2003), by combining statistical and dynamic diagnostics of Northern Hemisphere observations, found evidence for the reflection of stratospheric planetary waves in the structures of tropospheric planetary wave. This theory involves the impact of the stratosphere on the refraction index of the troposphere. When the zonal flow in the lower stratosphere is stronger, the vertically upward planetary waves tend to be deflected equatorward and *vice versa* (Limpasuvan et al., 2004).

Considering both the angular momentum balance and mass conservation, Haynes et al. (1991) proposed that persistent wave driving in the stratosphere induces a secondary circulation that transmits the stratospheric signal downward to the surface. This circulation closes in the planetary boundary layer; the Coriolis force associated with the circulation balances the wave driving in the stratosphere and the zonal drag in the boundary layer. This mechanism is called “downward control” principle, and it has been used to explain phenomena related to stratosphere-troposphere exchange, such as the Brewer-Dobson circulation (Plumb and Eluszkiewicz, 1999). “Downward control” experiments by Kushner and Polvani (2004), however, revealed that the stratospheric eddy forcing itself did not yield the full response in the tropospheric circulation, although the stratospheric anomalies penetrated into the upper troposphere. They suggested that the tropospheic synoptic-eddy feedback processes (Robinson, 1994, 1996, 2000) are also crucial for the full downward influence.

The real downward influence, however, is even more complex. Song and Robinson (2004) tested the hypothetical mechanism of "downward control with eddy feedback", which involves the tropospheric eddy reinforcement of a weak signal transmitted downward from the stratosphere by the secondary circulation. Their experiments indicated that, in addition to these two mechanisms, the planetary waves themselves also transmit a significant part of the dynamical signal from the stratosphere to the troposphere, even when these waves are weak.

Other possible mechanisms include downward influence through the redistribution of mass (Baldwin and Dunkerton, 1999) and potential vorticity (Black, 2002) in the stratosphere. Black and McDaniel (2007a) used piecewise potential vorticity inversion to study the downward influence across the final warming. They suggested that the tropospheric change during the stratospheric deceleration stage is a direct response to the latitudinal redistribution of potential vorticity, while in the tropospheric deceleration stage, the stratosphere affects the tropospheric circulation by vertically trapping the tropospheric waves. Chen and Held (2007) proposed that the stratospheric anomaly could modify the eastward propagation of tropospheric eddies thus affect the tropospheric eddy momentum flux. This mechanism could explain the recent poleward shift of the Southern Hemisphere surface westerlies in recent decades.

Here we investigate the mechanisms through which the final warming can influence the tropospheric circulation. Gerber et al. (2008) suggested the intrinsic time scale of the annular mode is shorter in the presence of topography or other stationary wave forcing. This implies a weaker transient eddy feedback when the jet is not zonally symmetric. As a transient event, it is possible that final warming does not allow enough time for the synoptic-eddies to respond systematically, so that the mechanism of the tropospheric eddy feedback in the presence of topography will be weaker than its absence (e.g. Song and Robinson (2004)). On the other hand, Song and Robinson (2004) suggested that the importance of planetary waves in coupling the troposphere to the stratosphere would increase in the presence of realistic planetary waves. In our final warming simulations, if the topographic forcing is strong enough, it is expected that the planetary waves will be more important than the synoptic eddies in exerting downward influence from the stratosphere. Thus our second hypothesis is that **the planetary waves are crucial in the observed downward influence of the final warming**.

Such hypothesis can be tested using ensembles of realistic final warmings in our model runs. By "realistic" we mean that the final warming onset dates and zonal wind and wave evolutions are similar to those in observations. We can compare the long waves with short waves in the troposphere to see whether the tropospheric eddy feedback is as important as Kushner and Polvani (2004) and Song and Robinson (2004). Then a detailed momentum budget analysis of the final warming will be performed, in order to understand the roles of the waves in determining the tropospheric changes. In addition, a zonally symmetric model will be used to rerun the final warming, applying the eddy forcing from the full model ensembles but disaggregated by wave numbers and altitudes (troposphere and stratosphere). Thus we will be able to discriminate between tropospheric signals due to "downward control" from the stratosphere and those due to tropospheric waves, as well as between the contributions from different wave numbers. In summary, it is expected that the role of the planetary waves in the downward influence from the stratospheric final warming will be clear and our second hypothesis will be tested.

1.2.3 Predictability of the stratospheric warmings

The final warming and sudden warming events, although occurring in the stratosphere, are affected by the troposphere. The polar vortex break-up date, the so-called final warming onset time, varies from year to year in both hemispheres (see Figure 4-4 in WMO (2006)). Variations in the timing of the final warming could have a large impact on the ozone depletion. A late final warming is often associated with a reduced ozone amount in the polar region, because of reduced transport into the polar stratosphere and increased chemical destruction. The interannual variability in the timing of the final warming is found to depend on the strength of planetary wave forcing (Farrara and Mechoso, 1986). Since the final warming is mostly determined by the annual cycle of solar radiation, it is not clear to what extent, the predictability of the final warming is controlled by the troposphere and/or by the stratosphere.

To improve predictions of sudden warmings, many studies focused on tropospheric precursors. Recent work links tropospheric blocking events to the sudden warmings. A blocking event is often defined as a temporally and spatially independent region of negative zonal index (500-hPa height at 60^o latitude higher than 40^o latitude) spanning at least 20^o longitude and persisting at least five days. Diagnostic analyses of cases (O'Neill, A. and Taylor, 1979; Quiroz, 1986) showed that blocking events could trigger the enhancement of upward propagating planetary wave activity and induce sudden warmings. Martius et al. (2009) reported that 25 of the 27 events objectively identified in the ERA-40 dataset for the period of 1957 - 2001 are preceded by blocking patterns. Although Taguchi (2008) does not find any statistical significant connection between the two events, Martius et al. (2009) argued that the absence of statistically significant connection comes from the fact that 500-hPa wave amplitudes are too weak; 200 hPa or above are needed to obtain a clear signal. They suggested that tropospheric blocking events are a necessary but not sufficient condition for the occurrence of sudden warmings.

On the other hand, some sudden warming studies focus more on the stratospheric internal vacillations. Mattewman (2009) found in a single-layer quasi-geostrophic model that a sudden warming could happen even without an anomalous tropospheric planetary wave source. These two different views of the dynamics of the sudden warmings lead to different deductions regarding the roles of troposphere and the stratosphere in determining their predictability.

An interesting question emerges: is the predictability of the sudden warming determined more by the stratosphere or by the troposphere? For final warmings, where both planetary waves and diabatic heatings are involved, a similar question arises. Since the final warming and sudden warming occur in the stratosphere, it is not surprising that the stratosphere itself should determine, at least in part, their predictability. On the other hand, since the tropospheric waves propagate into the stratosphere and interact with the mean flow, the state of the troposphere should also influence the predictability of the stratospheric warmings. Which layer is more important? In order to answer this question, we hypothesize that **much of the predictability of stratospheric warming events comes from the troposphere**. By carrying out a series of perturbation experiments of the tropospheric and stratospheric initial condition prior to the final and sudden warming and looking at how their timing changes in response to the different perturbations, we can obtain a better understanding of the different roles of the stratosphere and troposphere in determining the predictability of stratospheric warming events, and the hypothesis can be tested.

1.3 Model Appropriateness

In order to well test these three hypotheses, an appropriate general circulation model must be chosen. We hope to obtain a realistic seasonal transition in the stratosphere, but the model must be simple enough to keep the troposphere unchanged, so that we can determine how stratospheric final warming events affect the tropospheric circulation. For the specific purposes of testing our dynamical hypotheses a dynamical core has distinct advantages over a full global climate model. It is relatively simple but includes the key processes relevant to our problem. The stratospheric equilibrium temperature changes, with "radiation" parameterized by Newton cooling, can drive the seasonal transition only in the stratosphere while keeping the troposphere unchanged. By regulating the topographic forcing, planetary waves with different amplitudes can be induced. Finally, it is easy to carry out the large ensembles of final warming events and perturbation experiments we need to test our hypotheses rigorously and to study the predictability of the final and sudden warmings.

Full global climate models, on the other hand, provide a state-of-the-art depiction of every detail of Earth's climate system and, therefore, should be able to carry out more realistic simulations. The Whole-Atmosphere Climate Community Model (WACCM) incorporates a chemical transport model, a radiation model, and numerous parameterizations to characterize processes in middle atmosphere (Garcia et al., 2007). Many of the signals of recent climate change can be observed in output from its simulations. Fortunately, WACCM results simulating the years from 1950 to 2003 are available from http://cdp.ucar.edu for comparisons with our dynamical core results and with the NCEP/NCAR reanalysis dataset.

1.4 Outline

This thesis comprises seven chapters. Following this introduction, Chapter 2 gives a detailed description of the Geophysical Fluid Dynamic Laboratory (GFDL) dynamical core model. Chapter 3 describes results from our ensembles of simulated final warmings, which are used to test our first hypothesis. In Chapter 4, we discuss the mechanisms of the downward influence of the final warming. A series of perturbation experiments are discussed in Chapter 5 in order to investigate the predictability of the final and sudden warmings. Chapter 6 compares results from the 1950 to 2003 run of WACCM with the observations and with our dynamical core results. The final Chapter 7 presents conclusions and discusses some possible avenues for further research.

Chapter 2

Dynamical core model

Here we need a model for testing our hypothesis that the tropospheric manifestations of the final warming originate in the stratosphere. One important consideration is that we can induce the stratospheric seasonal transition alone, with the troposphere unchanged. The dynamical core model provides this flexibility, along with simplicity and computational efficiency. The Newton cooling parameterization simplifies radiative processes, representing diabatic heating by relaxing the temperature to a pre-assigned radiative equilibrium temperature T_{eq}. The stratospheric seasonal transition, then, is easily obtained by imposing T_{eq} changes only in the stratosphere. In section 2.1, we give a detailed description of the dynamical core model and the diagnostic methods we use to analyze our results. Perpetual season runs with different thermal and topographic forcings are described in section 2.2, followed by the summary and discussions in section 2.3.

2.1 GFDL dynamical core description

The dynamical core GCM is a primitive equation, hydrostatic, spectral model derived from the 1990s version of the Geophysical Fluid Dynamics Laboratory (GFDL) atmosphere model (Gordon and Stern, 1982). The model has a dry atmosphere and the radiative processes are represented by the Newton cooling parameterization. The same model has been used by Song and Robinson (2004) to study the mechanisms for the stratospheric influences on the troposphere. For our studies we have made some changes to the equilibrium temperature and Newton cooling rate.

2.1.1 Resolution and integration equations

The model runs at rhomboidal 30 (R30) spherical harmonic truncations (equivalent to 96 and 80 grid points in zonal and longitudinal directions), Rhomboidal 60 (R60) truncation is used to study the robustness of the results. σ coordinates are adopted in the vertical, where $\sigma = p/p_s$, p is the pressure and p_s is the surface pressure. We use the same levels as Scinocca and Haynes (1998), Song and Robinson (2004), in which there are $n_F = 30$ "full" levels and $n_F - 1$ "half" levels. The model domain extends from the surface of the Earth up to about 105 km. The forward integrations of prognostic equations occur on the full levels while the vertical velocity is computed at half levels every time step.The location of the $n_F - 1$ half levels are:

$$\sigma_i = \begin{cases} \dfrac{\sigma_{\text{tran}} - \sigma_{\min}}{n_{\text{trop}} - 1}(n_F - 1 - i) + \sigma_{\min} & (n_F - n_{\text{trop}} \leq i < n_F - 1) \\ \exp[\dfrac{\ln(\sigma_{\max} - \ln(\sigma_{\text{tran}}))}{n_F - n_{\text{trop}} - 1}(n_F - n_{\text{trop}} - i) + \ln(\sigma_{\text{tran}})] & (1 < i < n_F - n_{\text{trop}}) \end{cases}$$

where $n_{\text{trop}} = 9$ is the number of levels in the troposphere, which are linearly spaced up to $\sigma_{\text{tran}} = 0.1$. $\sigma_{\min} = 1 - (1 - \sigma_{\text{tran}})/n_{\text{trop}}$ and $\sigma_{\max} = 6.0 \times 10^{-7}$ (Scinocca and Haynes, 1998). Unless specified otherwise, the time step for the perpetual run is 14.4 minutes.

The dynamical core model is a typical spectral model, in which four variables: vorticity ζ, divergence D , temperature T and logarithmic surface pressure $\ln P_s$ are prognostic variables; geopotential height Φ and sigma vertical velocity $\dot{\sigma}$ are diagnosed every time step. The four prognostic model equations are:

$$\frac{\partial \zeta}{\partial t} = -\nabla \cdot (\mathrm{k} \ \times \frac{\mathrm{S}}{\cos\phi}) + \mathrm{k} \cdot \nabla \ \times \mathrm{F}_{\mathrm{vl}} - \upsilon \nabla^6 \zeta \tag{2.1}$$

$$\frac{\partial D}{\partial t} = \nabla \cdot (\frac{\mathrm{S}}{\cos\phi}) - \nabla^2 E - \nabla^2(\Phi + R\bar{T} \ln P_s) + \nabla \ \cdot \mathrm{F}_{\mathrm{vl}} - \upsilon \nabla^6 D \tag{2.2}$$

$$\frac{\partial T}{\partial t} = -\nabla \cdot (\mathrm{v}T') + T'D + \frac{R}{C_p}\{T[\frac{\dot{\sigma}}{\sigma} + (\mathrm{v} - \tilde{\mathrm{v}}) \cdot \nabla \ln P_s - D]\} - \dot{\sigma}\frac{\partial T}{\partial \sigma} + F_T - \upsilon\nabla^6 T \quad (2.3)$$

$$\frac{\partial \ln P_s}{\partial t} = -\tilde{\mathrm{v}} \cdot \nabla \ln P_s - \tilde{D} \quad (2.4)$$

where

$$\mathrm{S} = [(\zeta+f)\mathrm{V} - RT' \cos\phi \frac{\partial \ln P_s}{\partial x} - \dot{\sigma}\frac{\partial U}{\partial \sigma} + F_u \cos\phi]\vec{i} + [-(\zeta+f)\mathrm{U} - RT' \cos\phi \frac{\partial \ln P_s}{\partial y} - \dot{\sigma}\frac{\partial V}{\partial \sigma} + F_v \cos\phi]\vec{j}.$$

$E = \frac{U^2 + V^2}{2}$ is the kinetic energy. F indicates forcing terms with corresponding subscripts. The tildes represent vertical averages. The diagnose equations for geopotential height Φ and sigma vertical velocity $\dot{\sigma}$ are:

$$\frac{\partial \Phi}{\partial \sigma} = -\frac{RT}{\sigma} \quad (2.5)$$

$$\frac{\partial \dot{\sigma}}{\partial \sigma} = -(\mathrm{v} - \tilde{\mathrm{v}}) \cdot \nabla \ln P_s - (D - \tilde{D}) \quad (2.6)$$

Detailed deductions of these equations can be found in Gordon and Stern (1982).

2.1.2 Newton cooling parameterization

Radiative processes are parameterized by the Newton cooling. The temperature is relaxed to a zonally symmetric equilibrium temperature field, so that

$$\frac{\partial T}{\partial t} = \cdots - \alpha(z)(T - T_{\mathrm{eq}}(\phi, z))$$

where $\alpha(z) = 1/\tau(z)$ is the relaxation rate, and $\tau(z)$ is the relaxation time. The relaxation rate in the dynamical core is that used by Holton and Mass (1976). It is a function of height, given by $\alpha(z) = [1.5 + \tanh((z - 35\text{ km})/7\text{ km})] \times 10^{-6}\ \mathrm{s}^{-1}$, where z is the mean altitude of the model sigma level. The relaxation time ($\tau(z)$) varies from about 23 days in the troposphere to around 4 days in the stratosphere.

The equilibrium temperature is a function of latitudes and pressure. In the troposphere, the equilibrium temperature is similar to Held and Suarez (1994), in which

$$\mathrm{T_{eq}} = \max\{T_{\mathrm{pt}}, [315\mathrm{K} - (\Delta T)_y \sin^2\phi - (\Delta\theta)_z \log(\frac{p}{p_0})\cos^2\phi](\frac{p}{p_0})^\kappa\}$$

where $T_{pt} = 216.43$ K is the reference temperature at 100 hPa from the 1976 standard atmosphere. $(\Delta T)_y$=60 K, $(\Delta\theta)_z$=10 K, $\kappa = 2/7$.

In the stratosphere, the equilibrium temperature is calculated from the radiative zonal winds, following Scott and Haynes (1998), using the thermal wind relation. The mid-winter (Northern Hemisphere) and mid-summer (Southern Hemisphere) radiative zonal winds are:

$$U_R(\phi, z) = \cos\phi\cos(\frac{\pi}{2}\frac{z - z_B}{z_U - z_B})[u_0\tanh(b_0(\phi - \phi_0)) + J1 + J2 + J3]$$

for constant u_0, b_0, ϕ_0, with $z_B = 11.4$ km, $z_U = 105$ km and the $J_i(\phi, z)$ are defined as

$$J_i = u_i \mathrm{sech}(b_i(\phi - \phi_i))\mathrm{sech}(a_i(z - z_i)),\ i = 1, 2, 3$$

for constant u_i ,b_i, ϕ_i, a_i, z_i. The values of the constants for the velocity profile used in our calculation are:

$$u_0 = 20\,\mathrm{m\ s^{-1}},\ b_0 = 0.1,\ \phi_0 = 20^{\mathrm{o}},$$

$$u_1 = 280\,\mathrm{m\ s^{-1}},\ b_1 = 0.04,\ \phi_1 = 60^{\mathrm{o}}, a_1 = 0.05, z_1 = 65\,\mathrm{km},$$

$$u_2 = -20\,\mathrm{m\ s^{-1}},\ b_2 = 0.1,\ \phi_2 = 15^{\mathrm{o}}, a_2 = 0.3, z_2 = 30\,\mathrm{km},$$

$$u_3 = -220\,\mathrm{m\ s^{-1}},\ b_3 = 0.03,\ \phi_3 = -55^{\mathrm{o}}, a_3 = 0.04, z_3 = 70\,\mathrm{km}.$$

The equatorial equilibrium temperature profile in the stratosphere is adopted from the 1976 standard atmosphere and the equilibrium temperature in other regions is calculated by integrating the radiative zonal winds starting from the equator. The stratospheric and

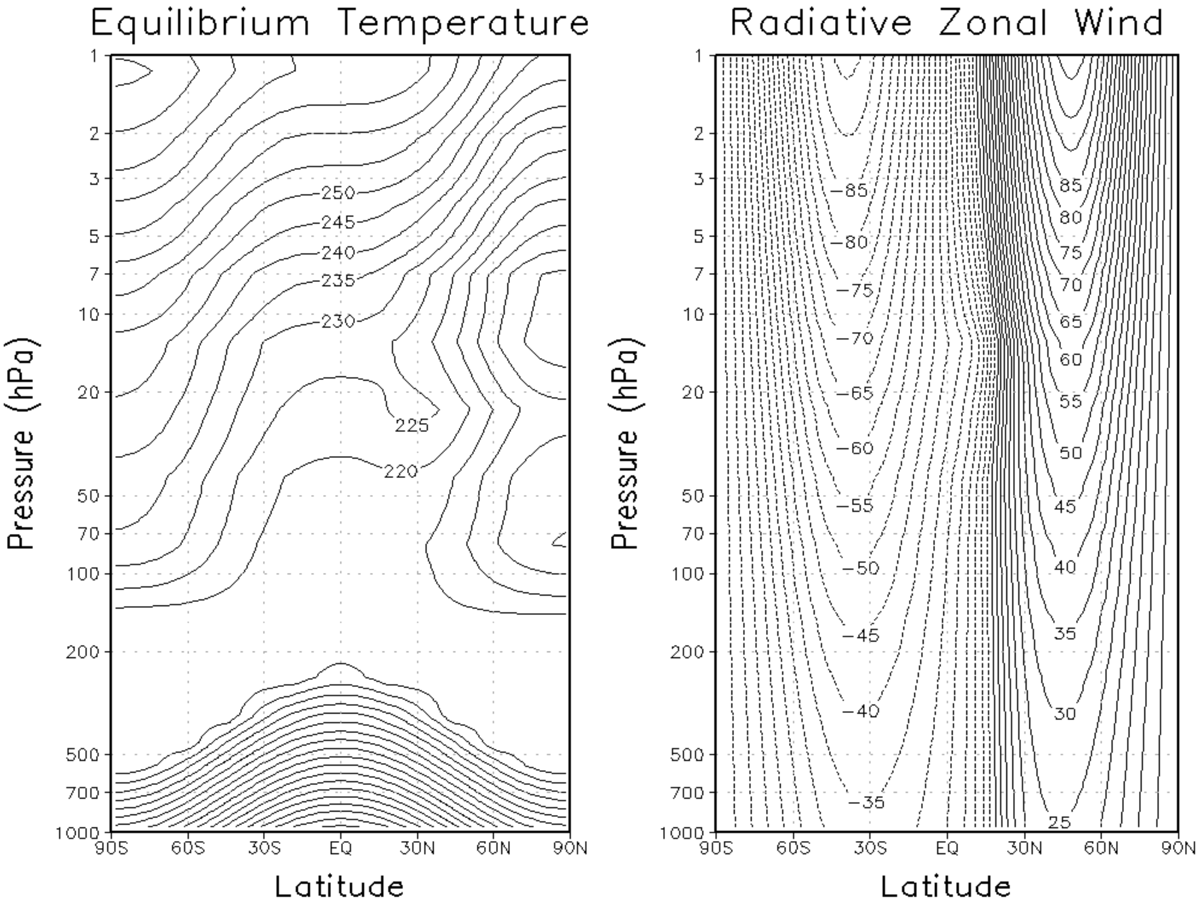

Figure 2.1: (Left) Radiative equilibrium temperature and (right) the radiative zonal wind by which equilibrium temperature is calculated in the stratosphere. The Northern Hemisphere and Southern Hemisphere are in the mid-winter and mid-summer, respectively. The contour interval is 5 K for the equilibrium temperature and 5 m s^{-1} for the radiative zonal wind. The stratospheric radiative zonal wind is adopted from Scott and Haynes (1998) with slight changes.

tropospheric T_{eq} are separated at 100 hPa. Fig. 2.1 shows the equilibrium temperature and the stratospheric radiative equilibrium zonal wind, for which Northern Hemisphere is in mid-winter and Southern Hemisphere is in mid-summer. When we run the model for a sufficiently long enough time with this T_{eq} fixed, we expect to obtain mid-winter and mid-summer state in the Northern Hemisphere and Southern Hemisphere stratosphere, respectively. When T_{eq} evolves from winter to summer, there will be seasonal transition in the model that enables our analysis of the resulting final warming.

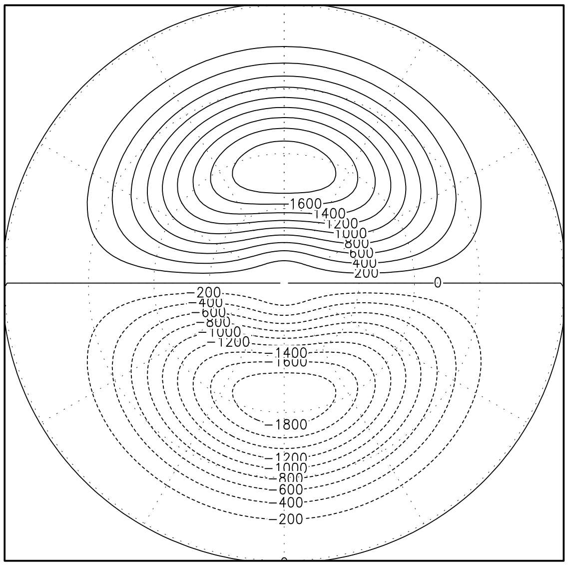

Figure 2.2: Northern Hemisphere topography with m=1 and 2000-m amplitude. The contour interval is 200 m. The peak of the mountain is at 45°N and extends to the equator and pole. Formula comes from Taguchi et al. (2001).

2.1.3 Topographic setting

The topography in the dynamical core is idealized and similar to that used by Taguchi et al. (2001), which is

$$h(\lambda,\phi)=\begin{cases} 4\mathrm{h}_0\mu^2(1-\mu^2)\ \sin(m\lambda) & (\mu\geq 0)\\ 0 & (\mu<0)\end{cases}$$

where $\mu=\sin(\phi)$ and m is the zonal wavenumber. Northern Hemisphere observations indicate that the wave number one is more important in the final warming processes (Figure 5 in Black and McDaniel (2007a)). Here, unless specified otherwise, we set m to one, though we also provide a brief discussion of wave number two final warmings. The amplitude of the topographic forcing is represented by h_0. We test seven different amplitudes from 0 m (no topography) to 3000 m every 500 m. For each h_0 value, 80 ensembles of seasonal transitions have been carried out, and these are used to analyze the final warming events. The Northern Hemisphere topography for h_0=2000 m is shown in Fig. 2.2, in polar stereographic projection. Other topographic forcings have the same spatial structure but different amplitudes.

2.1.4 Other settings

In the dynamic core, Rayleigh friction provides a linear treatment of near-surface drag. This is a common way to simplify the friction within the boundary layer, though the choice of the parameter can have a large impact on the model results. For example, Robinson (1997) found that the surface westerlies and midlatitude jet shift poleward as the friction is reduced. This shift, mostly due to the barotropic component of the zonal wind, is found to be controlled by the effect of drag on the zonal mean flows, as opposed to the effect of drag on the eddies. Further studies by Chen et al. (2007) showed that an increase in eastward phase speed of midlatitude eddies plays a crucial role in this shift. They suggested that the jet shift comes from the poleward shift of the subtropical critical latitude associated with the faster eastward phase speed in the dominant midlatitude eddies. Here we follow Song and Robinson (2004) to consider the near-surface drag $\kappa(\sigma)\vec{V}$ for $\sigma > 0.8$. The damping coefficient is given by

$$\kappa(\sigma) = \begin{cases} 0 & \sigma \leq 0.8 \\ \dfrac{1}{\tau}\dfrac{\sigma - 0.8}{0.2} & \sigma > 0.8 \end{cases}$$

where τ is the damping time scale 0.5 days.

As mentioned in Song and Robinson (2004), the inertial instability in the equatorial mesosphere may cause numerical instability. In order to prevent that, vertical diffusion is used in the momentum and thermodynamic equations. The same coefficient is used given by:

$$\mathrm{R_{vh}} = \mathrm{R_{vm}} = 0.5\ [1 + \tanh((\frac{z - 50\ \mathrm{km}}{20\ \mathrm{km}}))] \times \cos^4\phi \times 20(\mathrm{m^2\ s^{-1}})$$

where z is the logσ approximate altitude. Six-order horizontal diffusion is used throughout the model; the damping time for the smallest horizontal time scales resolved in the model (wave number 30 in R30 truncation) is 0.1 days.

2.1.5 Diagnostics

The dynamical core output includes the daily spectral fields for vorticity, divergence, temperature and surface pressure. When diagnosing the zonal mean and eddy terms, all of the calculations are performed within σ coordinates, to avoid any inaccuracies. The zonal wind, meridiondal wind, temperature and surface pressure are directed obtained from the spectral field by Fast Fourier Transform (FFT); the other variables, such as σ vertical velocity $\dot{\sigma}$, potential temperature θ, geopotential height Φ can be diagnosed in the same way as in the model.

The Transformed Eulerian Mean form of the momentum equation under σ and spherical coordinates is very similar to Song and Robinson (2004) with slight simplifications, in which

$$\overline{P_s}\frac{\partial \bar{u}}{\partial t} + \alpha\,\bar{v}^* + \beta\,\bar{\omega}^* = -\nabla\cdot \mathrm{F} - \frac{\partial(\overline{P_s' u'})}{\partial t}$$

where

$$\alpha = \frac{1}{a\cos\phi}\frac{\partial(\bar{u}\cos\phi)}{\partial\phi} - 2\Omega\cos\phi$$

$$\beta = \bar{u}_\sigma$$

$$\bar{v}^* = \overline{P_s v} - \psi_\sigma$$

$$\bar{\omega}^* = \overline{P_s\dot{\sigma}} + \frac{1}{a\cos\phi}\frac{\partial(\psi\cos\phi)}{\partial\phi}$$

are the two residual circulation terms and $\psi = \dfrac{\overline{(P_s v)'\theta'}}{\bar{\theta}_\sigma}$. The Eliassen-Palm divergence term is:

$$-\nabla\cdot\mathrm{F} = -\frac{1}{\cos\phi}\{\frac{1}{a\cos\phi}\frac{\partial[\mathrm{F}^{(\phi)}]}{\partial\phi} + \frac{\partial[\mathrm{F}^{(\sigma)}]}{\partial\sigma} + \frac{1}{a}\overline{P_s'\frac{\partial\Psi'}{\partial\lambda}}\}$$

where

$$\text{Horizontal Eliassen-Palm flux: } \mathrm{F}^{(\phi)} = [\overline{(P_s v)'u'} - \beta\psi]\cos^2\phi$$

$$\text{Vertical Eliassen-Palm flux: } \mathrm{F}^{(\sigma)} = [\overline{(P_s\dot{\sigma})'u'} + \alpha\psi]\cos\phi$$

Comparing with the Eliassen-Palm flux in pressure coordinates, there is an extra term that cannot be explained as the divergence of a flux. Detailed deductions for the Eulerian mean and Transformed Eulerian Mean equations under σ and spherical coordinates are presented in appendix A.

2.2 Perpetual run

We run the model in perpetual-season mode by fixing the equilibrium temperature and applying different settings for the topographic forcing and the strength of the stratospheric vortex. The purpose of these runs is to check the variability of the zonal wind and waves under different external forcings and to test the sensitivity of the winter state to values of the parameters. In the mid-summer Southern Hemisphere, the zonal winds are quite calm and have much less variability than in the Northern Hemisphere, due to the relative absence of planetary waves. Therefore, only the Northern Hemisphere mid-winter is considered in these perpetual-season runs.

2.2.1 Topographic amplitudes

We first fix the T_{eq} as shown in Fig. 2.1 and run the model for 4000 days with seven different topographic amplitudes (h_0=0 m, 500 m, 1000 m, 1500 m, 2000 m, 2500 m, 3000 m). The resulting Northern Hemisphere circulation will be in a typical mid-winter state. Fig. 2.3 shows the average zonal mean zonal wind. The main differences among these simulations with different topographic amplitudes are in the stratosphere. Fig. 2.4 (a) shows the 10-hPa zonal wind, from which the poleward shift and the weakening of the jet with increasing topographic amplitudes is clear. Fig. 2.5 shows the 10-hPa 70°N zonal mean zonal wind variability. Without topographic forcing or with weaker topography, the variability in the zonal wind is small. The zonal wind becomes larger as the topography increases from 0 m to 1500 m, due to the poleward shift of the stratospheric jet. At greater topographic amplitudes, the zonal wind becomes much more active and frequent transitions from westerly to easterly winds are evident, indicating the occurrence of sudden warmings. From Fig. 2.4 (a) it appears that when h_0 is larger than 2000 m, the stratospheric jet shifts equatorward slightly, though this is misleading. In fact, the occurrence of sudden warmings causes the average zonal wind near the polar region to weaken; between warming events, the winter jet is still around 70°N.

When the topographic forcing increases, the tropospheric circulation also changes. Fig. 2.4 (b) shows the 1000-hPa zonal mean zonal wind for different h_0. With the increase of the h_0, the 1000-hPa zonal wind becomes weaker between 40°N and 60°N. This reduction is associated with an equatorward shift of the tropospheric jet from around 40°N to 35°N, shown in Fig. 2.3.

The zonal wind variations in the stratosphere are closely connected with planetary waves. Fig. 2.6 shows the long-term mean Eliassen-Palm divergence for different topographic amplitudes. The most obvious difference is in the stratosphere. The Eliassen-Palm convergence magnitude increases with the increase of topographic amplitudes, suggesting the presence of stronger planetary waves in the stratosphere. The 10-hPa 70°N variations are shown in Fig. 2.7, where the more abrupt changes of waves with the increase of topographic amplitudes are clear. In addition, when a sudden warming occurs, a large Eliassen-Palm convergence can be observed: for example, the two sudden warmings around day +3250 and day +3800 for h_0=2000-m perpetual run.

2.2.2 Vortex strengths

We explore the sensitivity of the average long-term zonal-mean zonal wind and its variability to changes in the radiative vortex strength parameter u_1 (see section 2.1.2) to 120, 200, 240, 320 and 360 m s^{-1}, together with h_0 = 2000-m topographic forcing. This is similar to the thermal forcing experiment in Song and Robinson (2004) and Kushner and Polvani (2004). The stratospheric jets with different u_1 are shown in Fig. 2.8, and the 10-hPa zonal wind variations are shown in Fig. 2.9. When the stratospheric jet parameter u_1 increases, the induced stratospheric jet also increases, similar to results shown in Fig. 2.4 for different h_0. The latitudes of the stratospheric jet, however, change much less here than when the

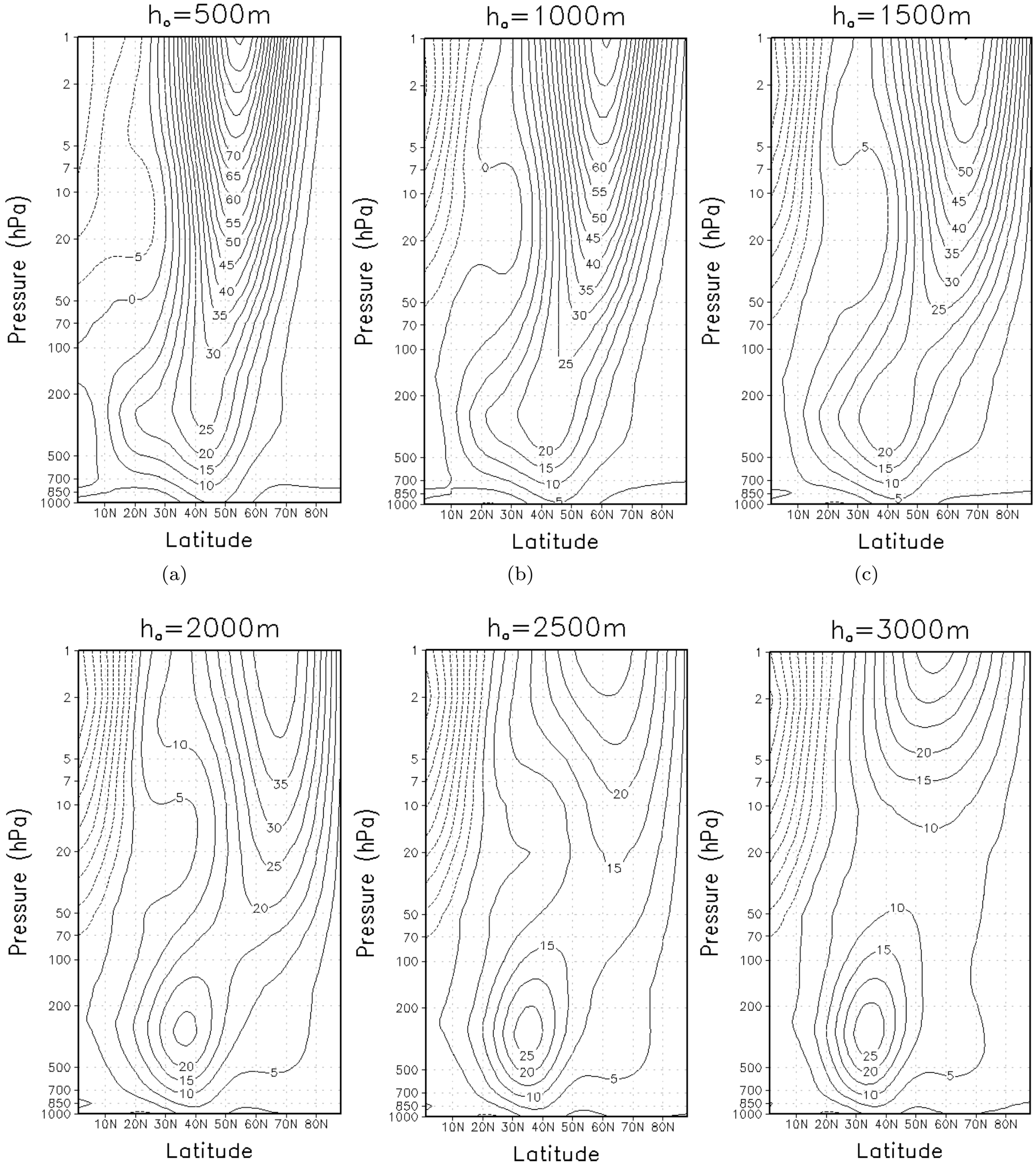

(a) (b) (c)

(d) (e) (f)

Figure 2.3: Perpetual winter long-term zonal mean zonal wind for different h_0 cases in the dynamical core model. (a) h_0=500 m; (b) h_0=1000 m, (c) h_0=1500 m, (d) h_0=2000 m, (e) h_0=2500 m, (f) h_0=3000 m. The contour interval is 5 m s^{-1}.

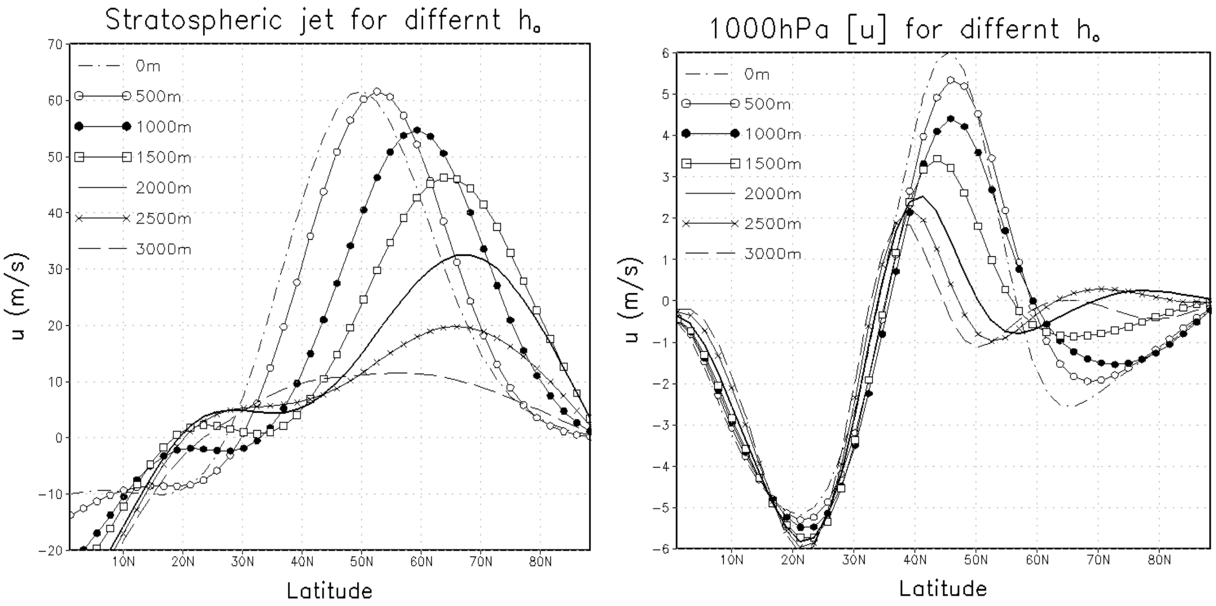

(a) (b)

Figure 2.4: Perpetual winter long-term mean zonal mean zonal wind for different h_0 cases at (a) 10 hPa and (b) 1000 hPa in the dynamical core model.

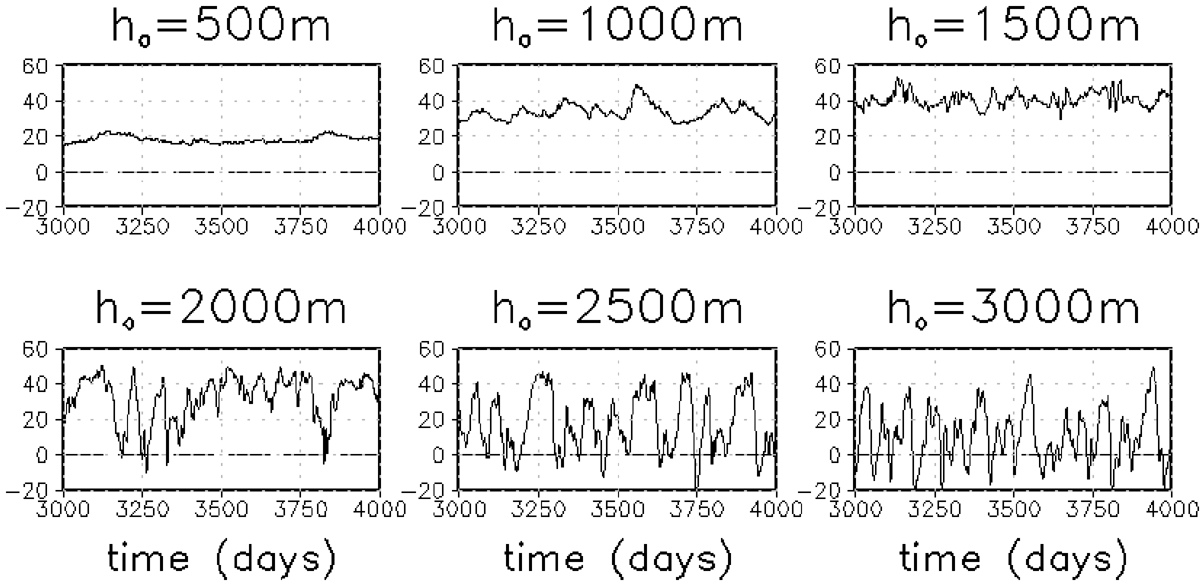

Figure 2.5: Perpetual winter zonal mean zonal wind variability at 10 hPa and 70°N for different h_0 cases in the dynamical core model.

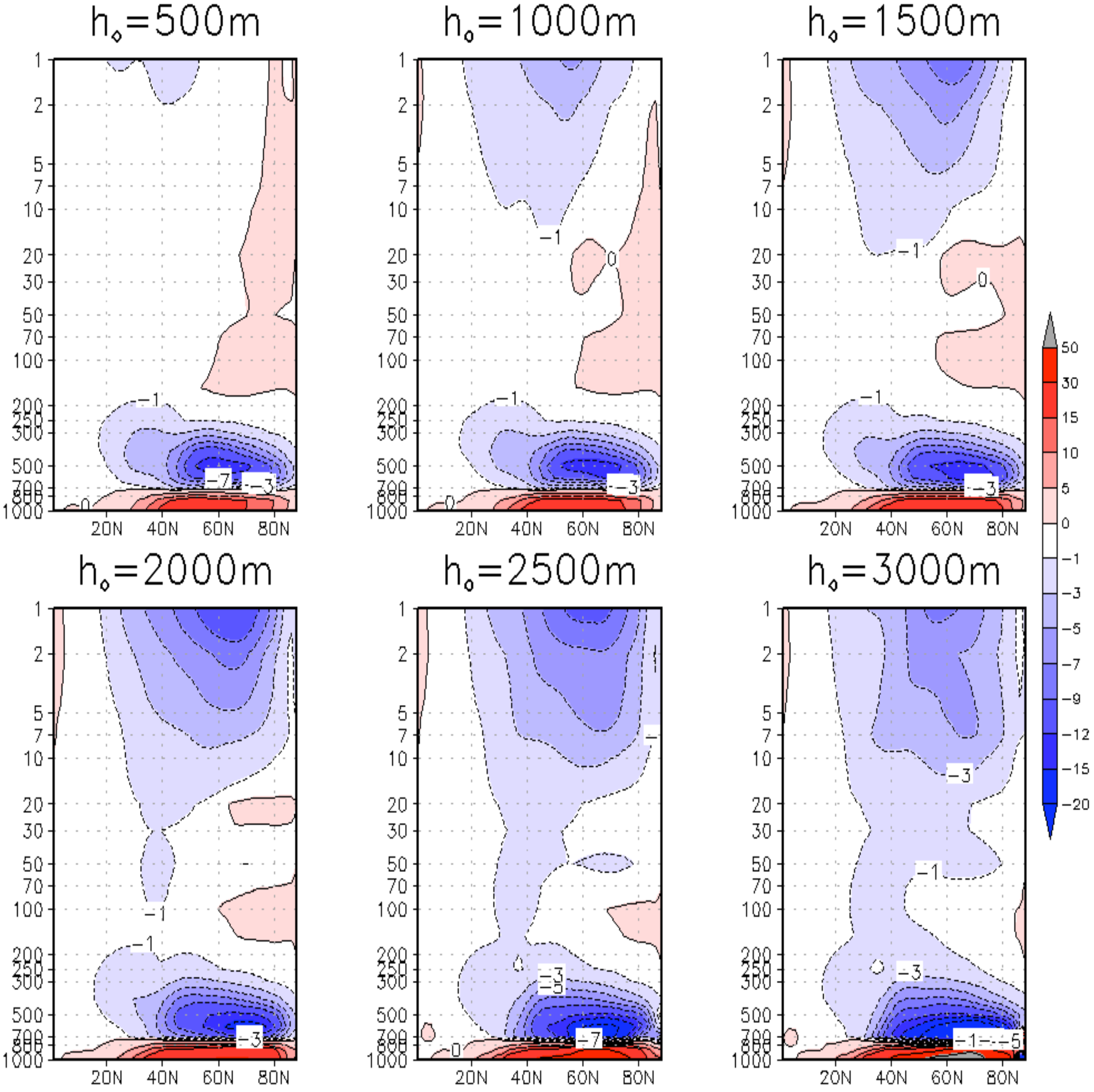

Figure 2.6: Perpetual winter long-term Eliassen-Palm divergence for different h_0 cases in the dynamical core model. The unit is m s^{-1} day $^{-1}$.

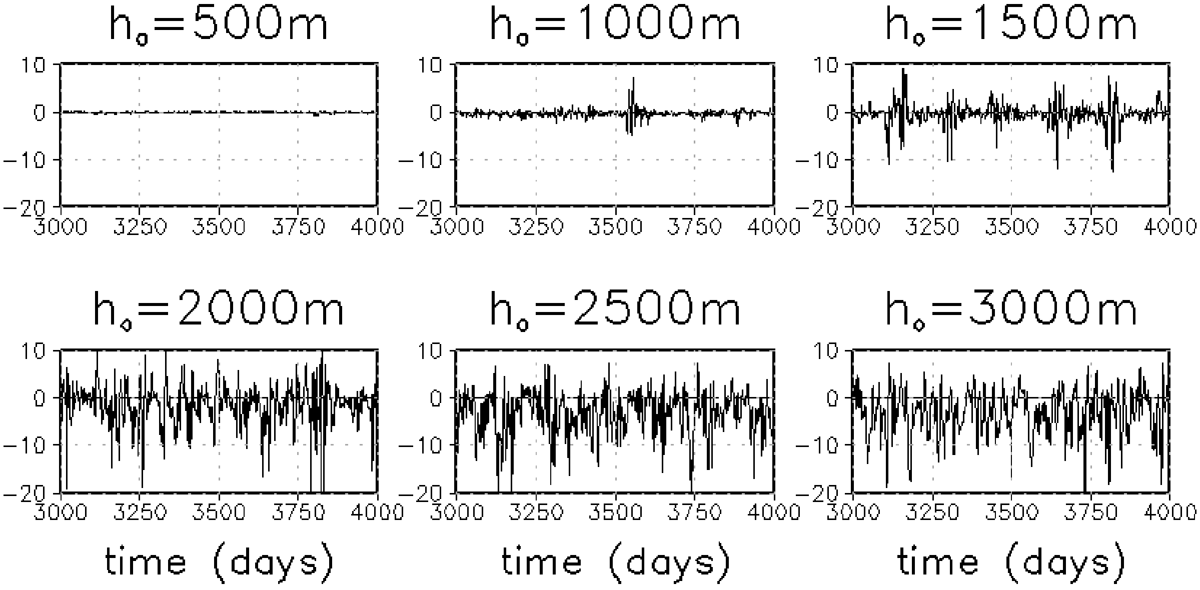

Figure 2.7: Perpetual winter 10-hPa 70°N Eliassen-Palm divergence variability for different h_0 cases in the dynamical core model. The unit is m s^{-1} day $^{-1}$.

topographic forcing is changed. In addition, the stratospheric zonal wind variations are larger than the topographic forcing cases, even when the vortex is very strong (Fig. 2.9).

When the stratospheric jet strengthens due to the increase of u_1, unlike in the topographic forcing cases, the tropospheric zonal wind changes are small, as can be seen from the 1000-hPa zonal wind in Fig. 2.8. We also consider the stratospheric jet strengthening without topography, with results shown in Fig. 2.10, which can be compared with the topographic results in Fig. 2.8. Without topography, the stratospheric jet shifts equatorward when it is strengthened. In the troposphere, the zonal wind changes are much larger than in the topographic cases in 2.8. The increase of zonal wind between 40°N and 60°N due to the poleward shift of the tropospheric jet is very clear.

2.2.3 Forcing wave numbers

We test the sensitivity to the form of topographic forcing by considering wave numbers 1, 2 and 3 with the same 2000-m amplitude. Fig. 2.11 shows the 10-hPa 70°N zonal wind variations for different wave numbers. Wave number 1 and 2 forcings are much more effective in interacting with the stratospheric flow than wave number 3. The stratospheric jet with

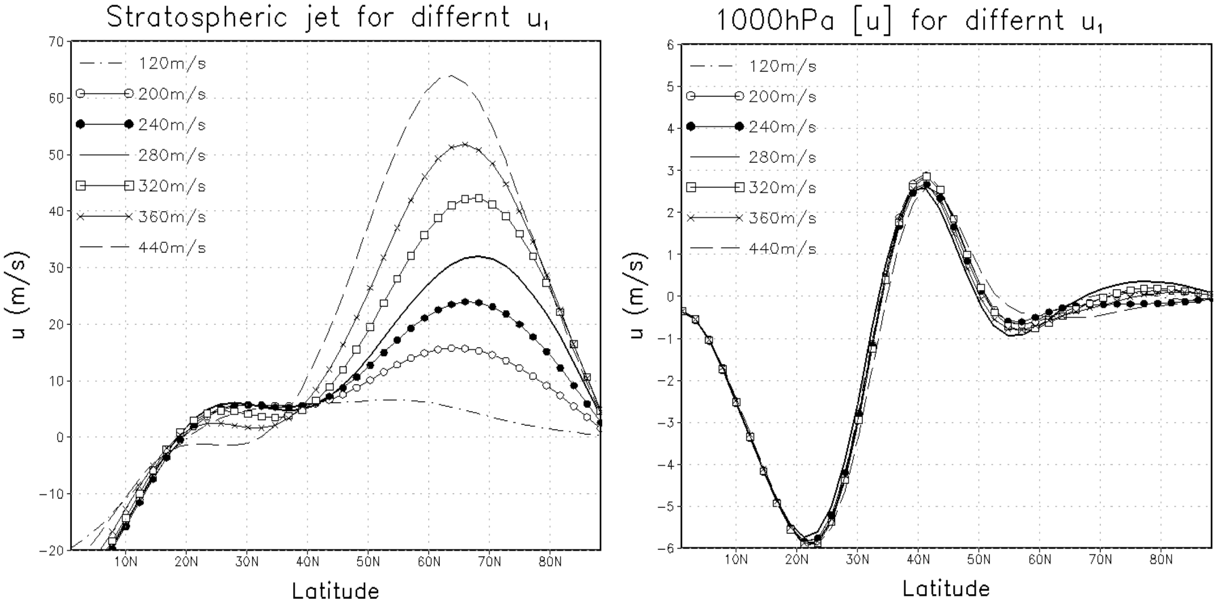

(a) (b)

Figure 2.8: Perpetual winter long-term mean zonal mean zonal wind for different u_1 cases at (a) 10 hPa and (b) 1000 hPa in the dynamical core model. Wave-1 2000-m amplitude topographic forcing is used in the perpetual run. u_1 is a parameter to characterize the radiative stratospheric jet strength, see section 2.1.2 for details.

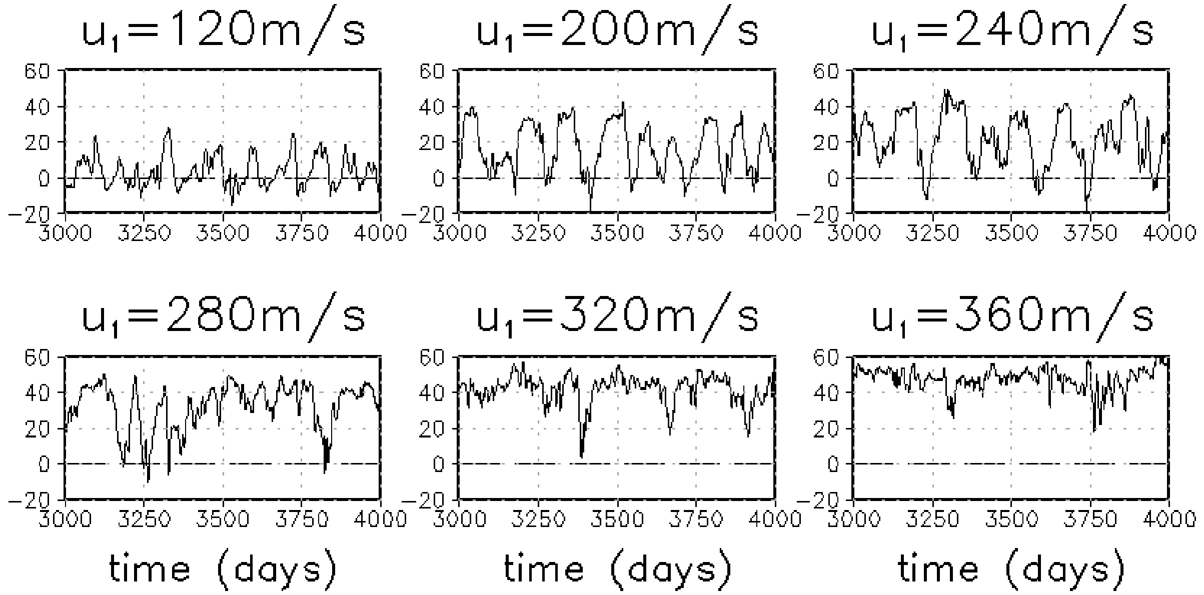

Figure 2.9: Perpetual winter zonal mean zonal wind variability at 10 hPa and 70°N for different u_1 cases in the dynamical core model. Wave-1 2000-m amplitude topographic forcing is used in the perpetual run. u_1 is a parameter to characterize the radiative stratospheric jet strength, see section 2.1.2 for details.

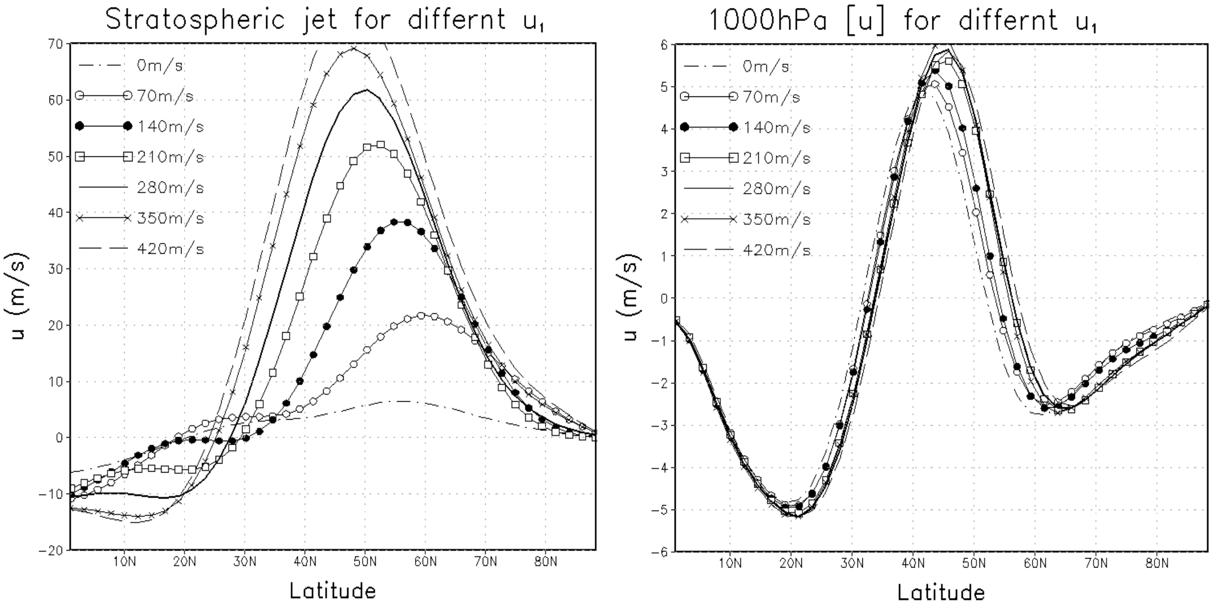

(a) (b)

Figure 2.10: The same with Fig. 2.8, but for non-topographic perpetual runs.

wave number 3 topography is similar to the h_0=500 m wave number 1 forcing. Variations in the zonal wind are weak, and no sudden warming occur within the 4000-day run. The stratospheric zonal wind due to wave number 1 topography has a shorter decorrelation time than with wave number 2 topography, and the stratospheric jet due to wave number 1 topography is slightly weaker than wave number 2 topography. The sudden warming in the wave number 1 case are of the "vortex displacement" type, while the wave number 2 forcing results in "vortex splitting" sudden warmings. If the sudden warming is defined as the reversal of the 10-hPa 70°N zonal mean zonal wind, the frequency of sudden warmings for both wavenumber 1 and 2 topography is approximately one event every 300 days.

2.2.4 Sensitivity experiments

We test the model sensitivity to the Newton cooling rate and to the horizontal resolution. The Newton cooling relaxation time determines the rate of thermal damping for both the waves and the mean flow, and so is expected to affect the zonal wind and its variability. A unrealistic relaxation time can result in model results that deviate significantly from

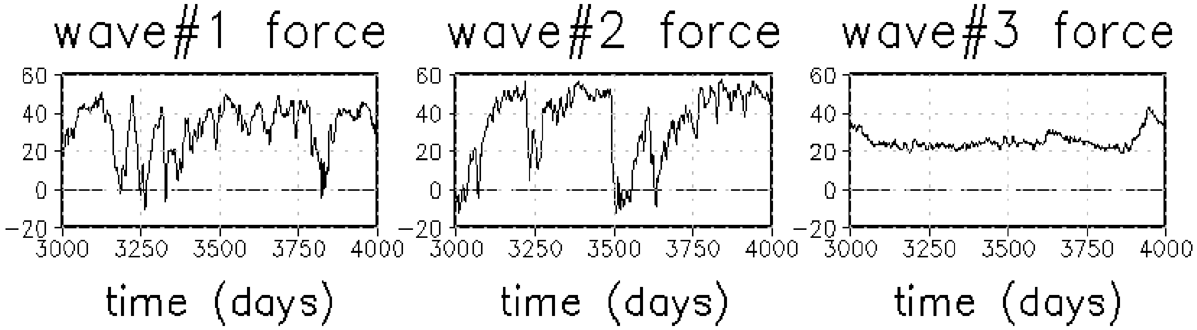

Figure 2.11: Perpetual winter zonal mean zonal wind variability at 10 hPa and 70°N for different wave number (1, 2, 3) forcings in the dynamical core model. The topographic amplitude is 2000 m.

observations. For example, a long relaxation time may allow unrealistic cold layers develop near the surface, particularly in the tropics (Held and Suarez, 1994). Scott and Polvani (2006) compare the relaxation formula of Holton and Mass (1976) with a fixed relaxation time of 10 days in the stratosphere. They found the zonal wind variability under the former setting is more regular and more sudden warming occur than with the constant 10 days relaxation rate. The relaxation rate by Holton and Mass (1976) is more realistic but it is of interest to look at other settings, to understand their impact on the model. Here we test three other different relaxation time, 25 day^{-1} as used by Song and Robinson (2004), 10 day^{-1} from Scott and Polvani (2006), and the formula of Held and Suarez (1994), in which the relaxation rate is

$$K_T = K_a + (K_s - K_a)\max(0, \frac{\sigma - \sigma_b}{1 - \sigma_b})\cos^4\phi$$

where $K_s = 1/4$ day^{-1}, K_a=1/40 day^{-1}, $\sigma_b = 0.7$. So above 0.7 σ level, the relaxation time is 40 days, below it, there is a transition to 4 days near the surface at the equator.

All three simulations produce similar tropospheric jet, albeit at different latitudes, as shown in Fig. 2.3, the structure of the stratospheric zonal wind, however, is very sensitive to the Newton cooling rates. Fig. 2.12 shows the 10-hPa 70°N zonal wind variability for different settings. The frequency of the variability decreases with increasing radiative time scale (Scott and Polvani, 2006). Under the Held and Suarez (1994) setting, the stratospheric

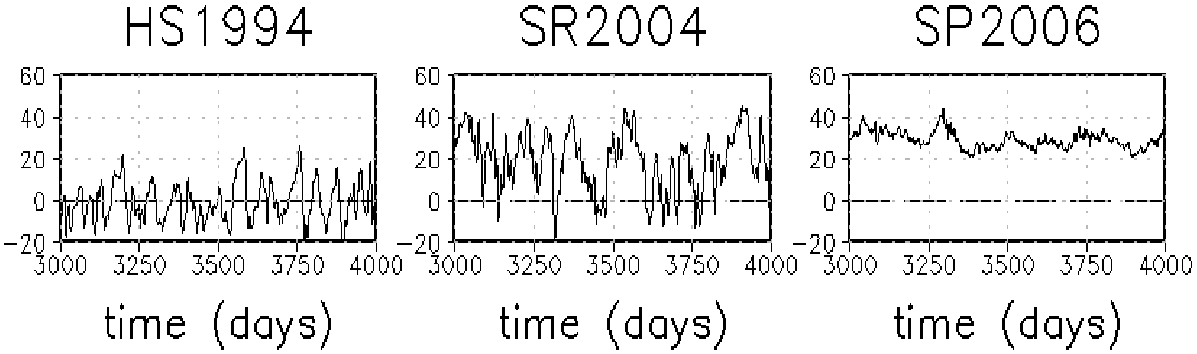

Figure 2.12: Perpetual winter zonal mean zonal wind variability at 10 hPa and 70°N for different Newton cooling rates (Held and Suarez, 1994; Song and Robinson, 2004; Scott and Polvani, 2006) in the dynamical core model. Wave-1 2000-m amplitude topographic forcing is used in the perpetual run.

jet disappears, due to strong wave-mean flow interaction. The Song and Robinson (2004) setting gives a slightly more active stratosphere and weaker stratospheric jet. The Scott and Polvani (2006) setting, on the other hand, shows a much stronger polar vortex with less variability. The zonal wind structure and variability resemble the results obtained for different topographic amplitudes. The relaxation time of Holton and Mass (1976) is 4 days above 0.01 σ level, which is much shorter than these three cases. The relaxation time below 0.01 makes a transition to 23 days, a value between those used by Scott and Polvani (2006) and by Song and Robinson (2004). Thus, the fact that the zonal wind structure and variability using the value in Holton and Mass (1976) are between those obtained using the values by Song and Robinson (2004) and Scott and Polvani (2006) suggests the stratospheric jet strength and variability are determined more by the radiative relation time in the lower stratosphere and than in the upper stratosphere.

Simulations run with rhomboidal 15, 30 and 60 truncations are used to test the sensitivity of the circulation and its variability to the horizontal resolution. The 10-hPa 70°N zonal wind variability is shown in Fig. 2.13. At R15 truncation, the stratospheric jet is strong and the zonal wind varies regularly with a period around 30 days. At R60 resolution, the stratospheric jet becomes much weaker than at R30, and the variability is also larger with more frequent sudden warmings.

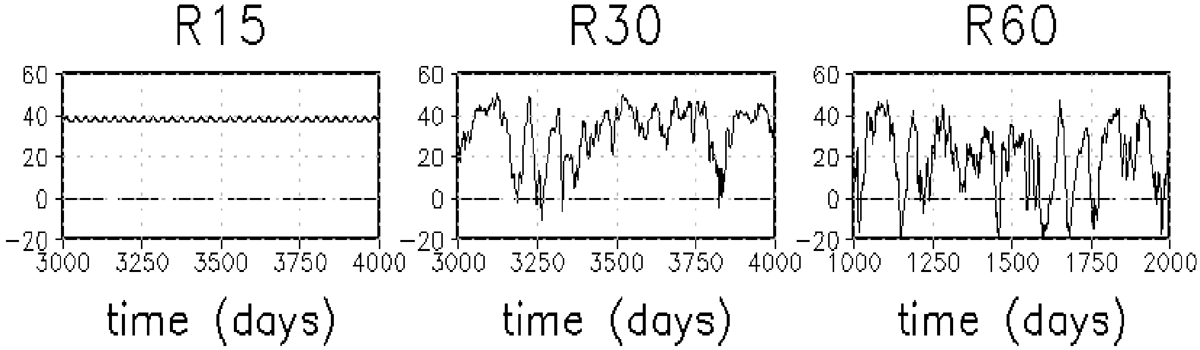

Figure 2.13: Perpetual winter zonal mean zonal wind variability at 10 hPa and 70°N for different horizontal resolutions (R15, R30, R60) in the dynamical core. Wave-1 2000-m amplitude topographic forcing is used in the perpetual run.

2.3 Summary and discussion

In the previous section, the perpetual winter runs with different topographic amplitudes display the weakening and poleward shift of the stratospheric jet with increased topographic forcing. This is as expected. Without topography, the planetary waves in the stratosphere result only from the wave-wave interaction among baroclinic eddies in the troposphere, and the planetary wave amplitudes are relatively small. These results, with weak wave-mean flow interactions and a strong stratospheric jet, are similar to that in radiative equilibrium (Fig 2.1), and the high-latitudes zonal winds have little variability. When the topographic amplitude is increased, stationary planetary waves becomes more and more important. They propagate upward into the stratosphere and interact with the mean flow, causing the stratospheric jet to become weaker and to shift poleward from 50°N to 70°N. At the same time, the zonal wind variability also becomes stronger, sudden warmings occur above 2000-m amplitude. Fig. 2.3 shows the positive feedback between the tropospheric planetary waves and the stratospheric mean flow. The stationary waves propagate only within the window of $0 < u < u_c$. When the waves are weak, the stratospheric zonal mean flow is strong and only small fraction of the tropospheric wave activity can penetrate the tropopause. When the waves become stronger, however, the strong interaction weakens the mean flow, permitting more waves into the stratosphere and further weakening the mean flow.

When the stratospheric jet parameter u_1 is changed, the stratospheric jet changes, similar to the response to changes in the topographic amplitude. Changes in u_1, however, yield only small changes in the jet latitude. Changes in the tropospheric zonal winds are much smaller in response to changes in u_1 compared with their response to changes in topographic amplitude, though these changes are greater when there is no topographic forcing. The tropospheric changes for the non-topographic cases are, in fact, unrealistic, due to the very long decorrelation time scale of the annular mode. When the time scale associated with the annular mode is reduced, the tropospheric response to the stratospheric forcing is weaker (Chan and Plumb, 2009). With topography, the time scale of the annular mode is reduced to values similar to observations, and the steady tropospheric response to the stratospheric forcing is smaller. Our stratospheric thermal forcing results with topography are similar to those obtained by Gerber and Polvani (2009), since the closest latitude difference for R30 resolution is over 2^o around the tropospheric jet, on the same order with the tropospheric jet shift, we cannot observe any shift of the tropospheric jet.

Our wavenumber setting experiments indicate wave number 1 and 2 forcings are more effective than wave number 3, similar to the results obtained by Gerber and Polvani (2009), except that in our simulation the stratospheric jet with wave number 1 is weaker than wave number 2 forcing. The Newton cooling experiments indicate the long relaxation scale is favorable for wave propagation and larger zonal wind variability and a weaker stratospheric jet. They also suggest that the values of the Newton relaxation parameter in the lower stratosphere and troposphere are more important than those in the upper stratosphere for determining the strength of the jet. The resolution is found to have a large impact on the model: at a lower resolution (R15), the zonal wind structure fails to capture the main dynamics of wave-mean flow interaction in the stratosphere. The zonal wind structure and variability in R30 is much better and similar to the Southern and Northern Hemisphere observations for different topography. At a higher resolution (R60) the model has an even stronger wave mean flow interaction and weaker stratospheric jet, but the main features are similar to those obtained at R30 resolution.

In summary, from a series of experiments for the perpetual winter run, we find that given sufficient resolution (R30), proper parameters and external forcings, a winter state resembling the Southern Hemisphere and Northern Hemisphere observations can be obtained in the dynamical core model. Due to its simplicity, the results do not perfectly match the observations. Nevertheless, the consistency of the model results with the most important features of the observed circulation suggest that the dynamical core model can capture the key internal dynamics of the stratosphere-troposphere system and, therefore, is appropriate model for our mechanistic studies of the final warming.

Chapter 3

Stratospheric final warming simulation

The stratospheric polar vortex breaks up in the spring, re-forms in the fall due to the annual cycle of solar radiation. The stratospheric final warming and final cooling differ: the final warming is much more abrupt than final cooling because of the planetary waves (Black et al., 2006). Analyses of daily observations Black et al. (2006); Black and McDaniel (2007b) revealed that the stratospheric final warming makes a significant contribution to the spring transition in the lower troposphere, especially in the Northern Hemisphere. Monthly analyses of final warmings by Ayarzaguena and Serrano (2009) also suggested that the Northern Hemisphere final warming has a substantial impact on the tropospheric storm track over the North Atlantic and the numbers of storms that cross Northern Europe in April. In this chapter, the dynamical core model is used to simulate final warming events by imposing a transition in radiative equilibrium temperature from winter to summer only in the stratosphere. We then follow Black et al. (2006) to construct composites for the evolution of the final warming in the zonal wind and in planetary waves, and we test our first hypothesis that much of the observed tropospheric signal in the final warming is initiated from the stratosphere. Section 3.1 describes the method for simulating the final warming. Results for the modeled seasonal transition follow in section 3.2. The final warming results are described in section 3.3, and the dynamics of the final warming in section 3.4. The final section includes discussion and conclusion. Part of the content of this chapter appears in Sun and Robinson (2009).

3.1 Simulation method

The stratospheric final warming is the final collapse of the polar vortex due to increased solar heating as spring progresses. Therefore, a seasonal transition is needed to produce and analyze final warmings. In the dynamical core model, radiative diabatic heating / cooling is parameterized by the Newton cooling, and the model state is driven by the radiative equilibrium temperature, $\mathrm{T_{eq}}$. The seasonal cycle can be induced by a radiative relaxation to a seasonally varying, zonally symmetric $\mathrm{T_{eq}}$ field, which is a sinusoidal transition between winter and summer equilibrium temperature fields (Scott and Haynes, 2002).

The winter and summer $\mathrm{T_{eq}}$ were given in Chapter 2. Here we first run the model with $\mathrm{T_{eq}}$ fixed for 2000 days, in order to obtain statistically stable winter and summer states in the Northern and Southern Hemispheres. Then the model is run for another 800 days. Output is taken from every tenth day, from day 10 to day 800 to be used as initial conditions for the seasonal runs. For each initial condition, a 365-day run is carried out with the $\mathrm{T_{eq}}$ evolving according to:

$$\mathrm{T_{eq}}(\phi, \sigma, t) = \gamma(t) \times \mathrm{T_{eqWINTER}}(\phi, \sigma) + (1 - \gamma(t)) \times \mathrm{T_{eqSUMMER}}(\phi, \sigma) \tag{3.1}$$

where $\gamma(t) = 0.5 \times (1 + \cos(2\pi \times t \text{ days}/365 \text{ days}))$, $\mathrm{T_{eqWINTER}}(\phi, \sigma)$ and $\mathrm{T_{eqSUMMER}}(\phi, \sigma)$ are the winter and summer $\mathrm{T_{eq}}$ shown in Fig. 2.1.

This yields an 80-member ensemble of seasonal transitions. Because the winter and summer $\mathrm{T_{eq}}$ are the same in the troposphere, the seasonal transition is driven radiatively only in the stratosphere. This experimental design allows us to look at how the stratospheric final warming affects the tropospheric circulation and to test our hypothesis.

Similar to the perpetual runs, seven different topographic amplitudes from 0 m to 3000 m are applied for the seasonal runs. For the 2000-m topographic amplitude, we also test two different stratospheric vortex strengths, by setting u_1 to 240 m s^{-1} and 320 m s^{-1}. In addition, runs are carried out with wave number 2 topographic forcing and at higher resolution (R60), to examine the robustness of the results. Each experiment comprises an

80-member ensemble.

3.2 Seasonal transition results

The climatological seasonal transition is obtained by averaging the 80 ensemble members, each following the same T_{eq} transition. The evolution of the zonal mean zonal wind at 10-hPa and 70°N is shown in Fig. 3.1. In the middle stratosphere, the seasonal transition between westerly winds in the winter and easterly winds in the summer is evident. As the amplitude of the topography is increased, the high-latitude zonal winds in mid-winter first increase due to the shift of the jet, then decrease because of the weakening of the jet, consistent with the perpetual runs. The final warming onset date, the date at which the zonal winds shift from positive to negative, becomes earlier with the increased strength of the topography. It is also of interest to look at the standard deviation across the seasonal ensembles. Variability in the zonal wind variations is always weak during the summer, independently of the topographic amplitude. Zonal wind variability in winter, however, increases with the topographic amplitudes. The interannual variability of the seasonal transition comes, in part, from the initial conditions, which can be seen from the increase of the standard deviation at the beginning of the transition period. On the other hand, waves are also important for the interannual variability. In the absence of waves (summer state), the variations are much weaker. Plumb (2009) pointed out that the asymmetry between the Northern and Southern Hemisphere in the strengths of their planetary waves affects their mean states. There is large interannual variability of the temperature over the North Pole during winter, contrasted with the weaker variability over the South Pole, with the latter becoming marked only during the springtime (Labitzke, 1977).

The evolutions of the zonal mean zonal wind at 100 hPa and 70°N is shown in Fig. 3.2. Unlike the 10-hPa results, here the seasonality of the zonal winds disappears when the topography is weak. This implies that the lower stratosphere is less affected by the seasonal transition when planetary waves are weak. The standard deviations at 100 hPa are

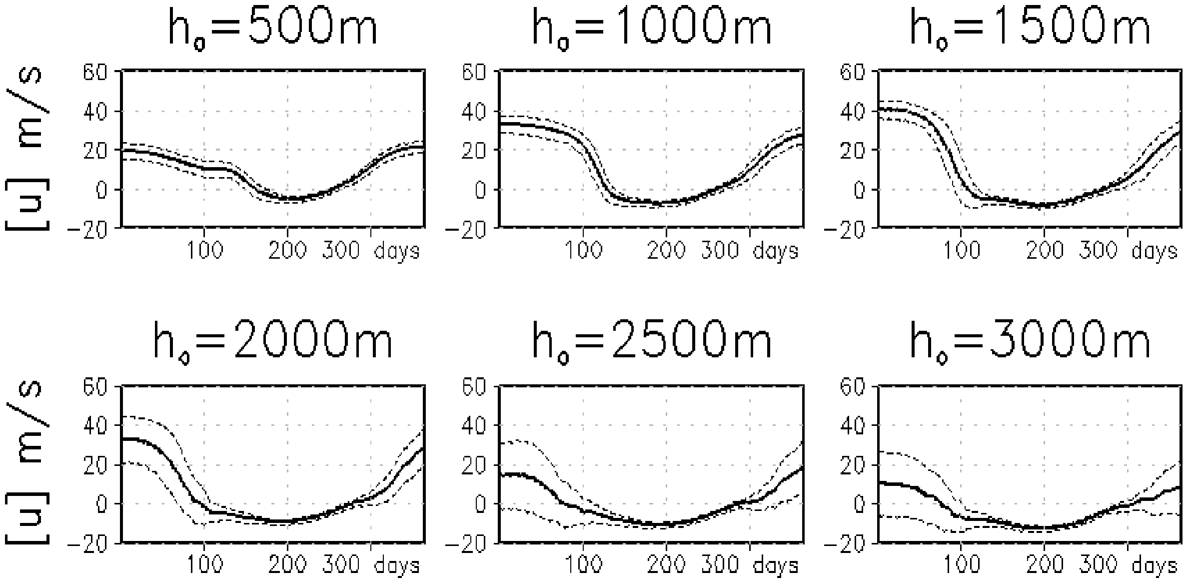

Figure 3.1: Climatological zonal mean zonal wind seasonal transitions at 10 hPa and 70°N for different topographic amplitudes. Solid line is the ensemble mean, dash lines are ensemble mean plus/minus standard deviation.

larger than at 10 hPa for every topographic amplitude, and the summertime has the same magnitude of variability as the wintertime. Since waves are present at 100 hPa during the summertime, this once again indicates the important role of waves in driving interannual variability.

Examining the zonal wind evolution in the troposphere, at 500 hPa shown in Fig. 3.3, no clear seasonal cycle is found. Given that the equilibrium temperature transition is only imposed in the stratosphere, this is not surprising. It suggests that climatologically the stratospheric influence on the tropospheric zonal wind is limited, when the topography is weak.

The seasonal cycle of the zonal wind is closely connected to that in the planetary waves. Fig. 3.4 shows the seasonal cycle of high-latitude Eliassen-Palm flux divergence at 10 hPa. For small-amplitude topography, even during mid-winter, the Eliassen-Palm flux divergence is near zero, indicating the absence of wave activity. Large Eliassen-Palm flux convergence occurs only in late and early winter. The late-winter peak is larger than the early-winter peak. Its timing is consistent with the dates of the 10-hPa final warming shown in Table 3.1.

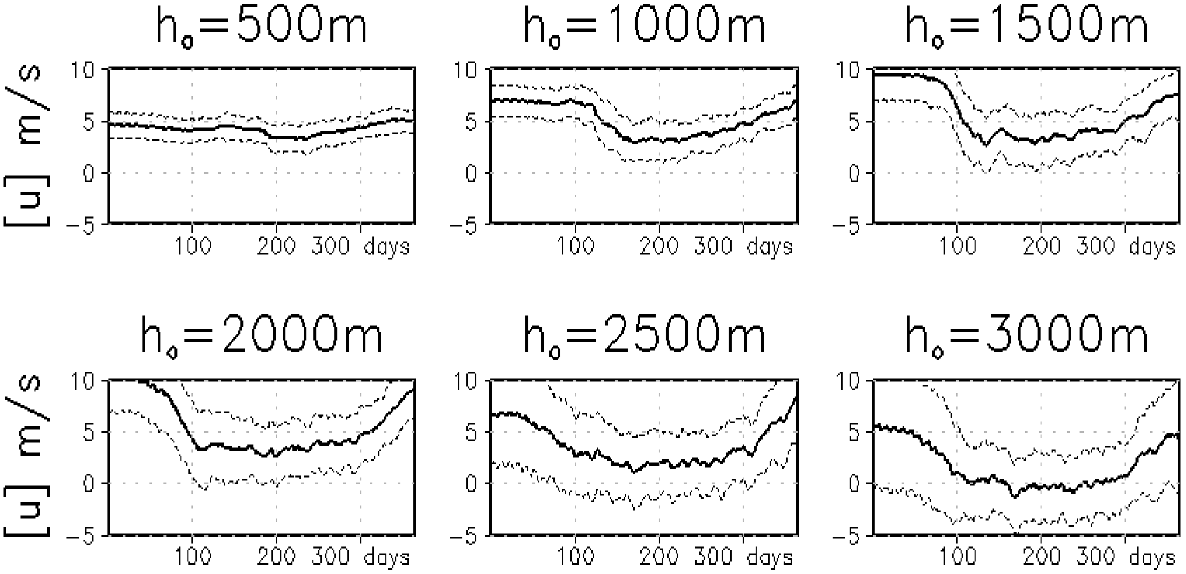

Figure 3.2: Climatological zonal mean zonal wind seasonal transitions at 100 hPa and 70°N for different topographic amplitudes. Solid line is the ensemble mean, dash lines are ensemble mean plus/minus standard deviation.

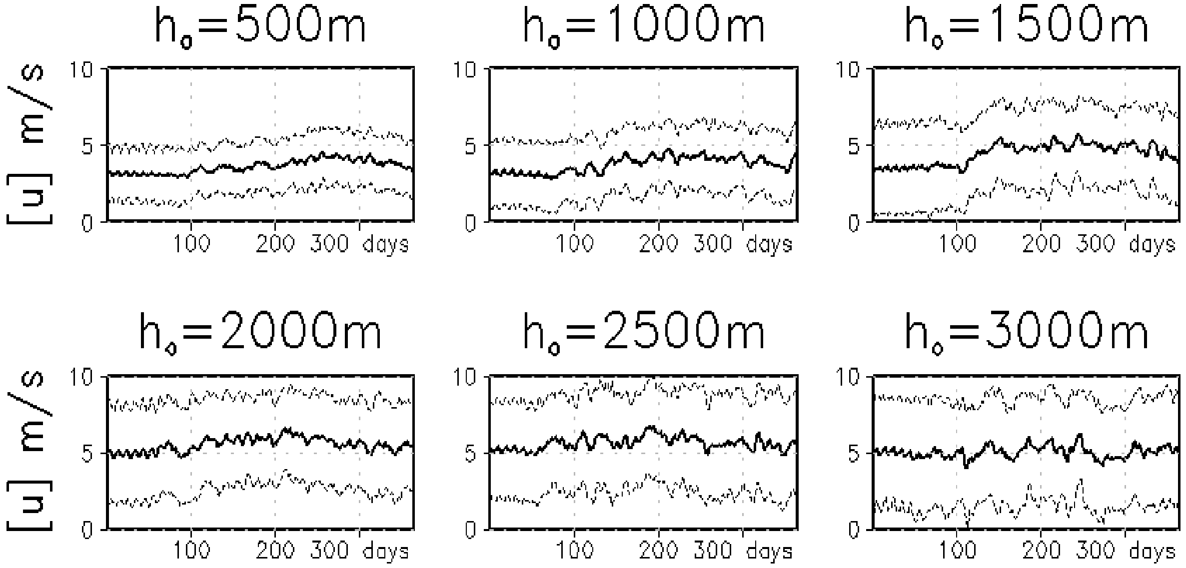

Figure 3.3: Climatological zonal mean zonal wind seasonal transitions at 500 hPa and 70°N for different topographic amplitudes. Solid line is the ensemble mean, dash lines are ensemble mean plus/minus standard deviation.

The wintertime Eliassen-Palm flux convergence strengthens with increasing topographic amplitude, while the convergence in summer is always zero, due to the absence of wave activity. The two maxima in the wave activity are present until the amplitude of the topography is 2000 m. At higher amplitudes, the convergence peaks in mid-winter and is weaker in the early and late winter.

The evolution of 100-hPa upward Eliassen-Palm flux is shown in Fig. 3.5. This quantity is consistent with the 10-hPa Eliassen-Palm flux convergence. The maximum of the upward flux in the late winter is very clear for weak topography. The wintertime upward Eliassen-Palm flux increases with the topographic amplitudes. For topography stronger than 2000 m, the upward flux weakens from mid to late winter, similar to the Eliassen-Palm flux convergence.

Differences in the evolution of wave activity between the low and high topographic amplitudes are also seen in observations. The observed planetary wave climatologies are quite different between Northern and Southern Hemispheres. From eight years (1979 - 1986) of daily geopotential data, Randel (1988) showed that in the Southern Hemisphere stratosphere, there is one maximum geopotential height variance in the late-winter / spring, with a distinct secondary, smaller maximum in late fall or early winter. These maxima in the variance result are primarily associated with wave number one fluctuation. In the Northern Hemisphere, however, the quasi-stationary planetary waves are active throughout the winter, until the final warming in the spring (Plumb, 2009). The seasonal evolution of the Eliassen-Palm flux divergence in our model, for low topographic amplitudes, is similar to Southern Hemisphere observations, while more like the Northern Hemisphere for high topographic amplitudes.

The asymmetric between Northern and Southern Hemisphere wave structures in the stratosphere appears to be a consequence of the positive feedback between waves and the mean flow (Plumb, 2009). According to the Charney-Drazin criteria, only those waves within the propagation window ($0 < u < U_c$) can penetrate the stratosphere. When the topographic forcing is too weak, there are strong zonal winds in the stratosphere, which prevent the propagation of waves. When the topographic forcing becomes stronger, more waves can enter the

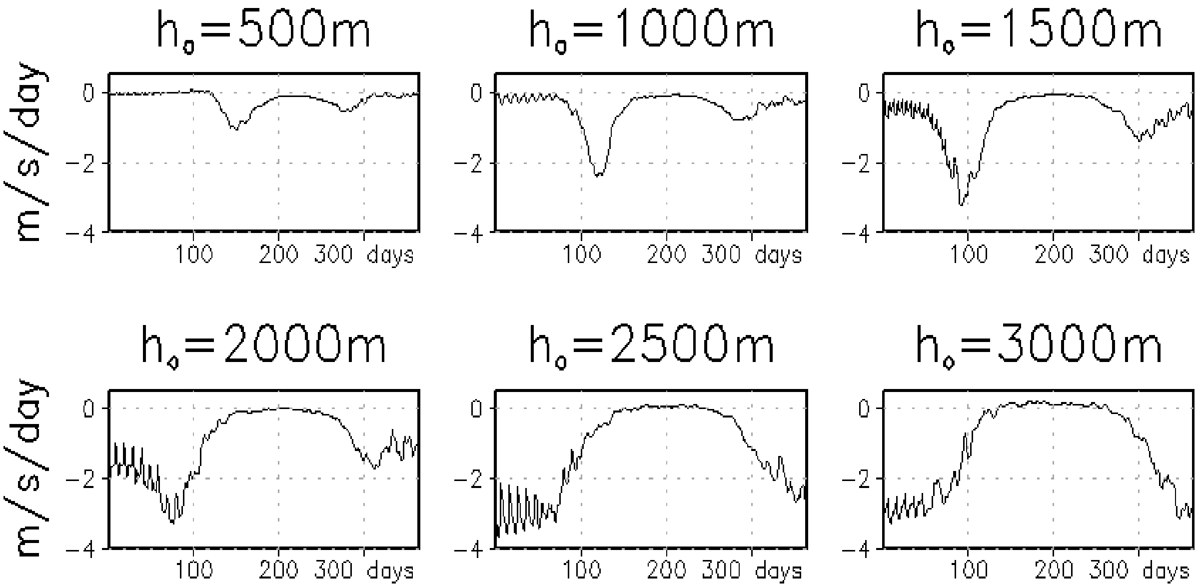

Figure 3.4: Climatological 60°N - 90°N averaged Eliassen-Palm divergence evolutions at 10 hPa. The unit of the Eliassen-Palm divergence is m s^{-1} day^{-1}.

stratosphere and weaken the zonal flow. The weaker zonal winds allow more waves enter the stratosphere and further weaken the zonal flow. Therefore, for the weak-forcing regime, only in the early and late winter when the zonal wind is weak, can large wave-one amplitudes occur. For the strong-forcing regime, however, wave-one amplitudes can be high throughout the winter because the weaker zonal winds do not prevent their vertical propagation.

3.3 Final warming analyses

3.3.1 Final warming onset dates comparison

Black et al. (2006), Black and McDaniel (2007b) performed observational analyses for the Northern and Southern Hemisphere final warmings using the NCEP/NCAR reanalysis and ERA-40 dataset. Here we adopt similar approaches to calculate the onset dates and construct final warming composites. Black et al. (2006) define the onset date of the final warming as the final time that the zonal-mean zonal wind at 50 hPa and 70°N drops below zero without returning above a 5 m s^{-1} threshold. The latitude 70°N is chosen, because it is the latitude of the Northern Hemisphere stratospheric jet. Similarly 60°S is used to define the final warming

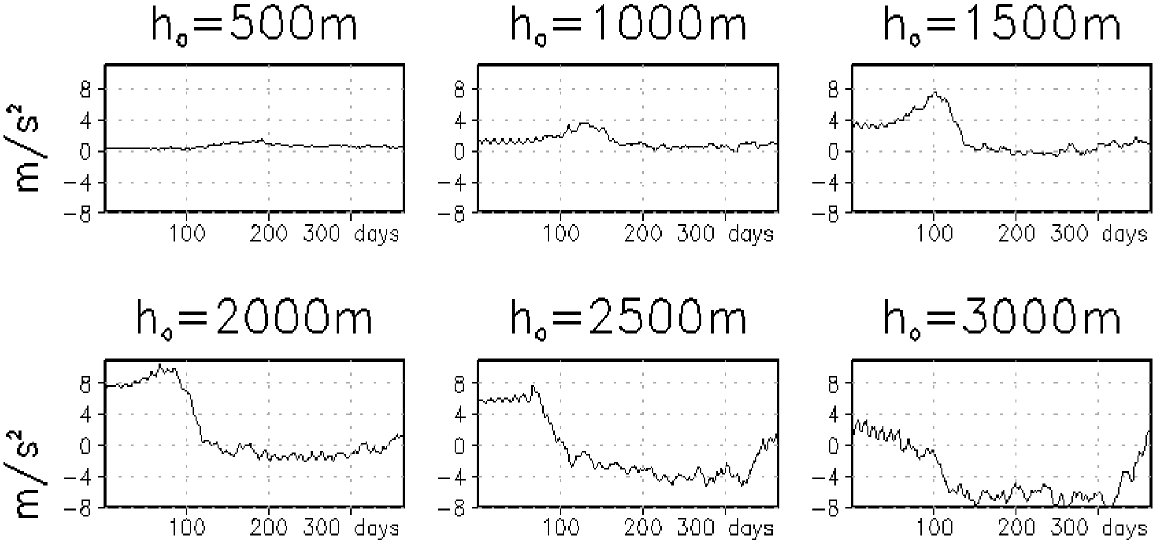

Figure 3.5: Climatological 60°N - 90°N averaged upward Eliassen-Palm flux evolutions at 100 hPa. The unit of upward Eliassen-Palm flux is 10^{-7}m s^{-1}.

in the Southern Hemisphere (Black and McDaniel, 2007b). For our seasonal transitions, the final warming onset dates are based on the latitudes of the mid-winter stratospheric jet, increasing from 50°N to 70°N with the amplitude of topographic forcing. In addition, when the topographic forcing is strong, the zonal wind variability during the seasonal transition is large, so that the 50-hPa zonal wind often exceeds 5 m s^{-1} even in the summertime. Thus we adopt a larger threshold, 10 m s^{-1}, in this study, to avoid cataloging such events into a very late final warmings.

Table 3.1 shows the ensemble mean final warming onset dates for different topographic forcings at different vertical levels. Here the final warming onset dates are the days after the transition in the equilibrium temperature begins (t in equation 3.1). At 10 hPa, the onset dates become earlier as topographic amplitudes increase. When the topographic forcing is weak, the zonal wind transition to negative does not occur in the lower stratosphere, so there is no final warming according to this definition. Only when h_0 is larger than 1500 m, does the zero wind line descend below the 50-hPa level. The final warmings at lower levels also occur earlier with the increase in topographic amplitudes. In addition, the time for the zero wind line to descend from 10 hPa to 50 hPa decreases with the increase of topographic amplitude, from around 30 days at 1500 m amplitude to around 7 days at 3000 m.

The final warming onset dates for different vortex strengths are tested by running 80-member ensembles for $u_1 = 240$ m s^{-1} (weak vortex) and $u_1 = 320$ m s^{-1} (strong vortex) with a topographic amplitude of 2000 m. Comparing with the $u_1 = 280$ m s^{-1} control run, the mean final warming for the weak vortex events occurs around 6 days earlier, while the mean onset date for the strong vortex is 10 days later. Since these three final warming events have the same topographic forcing, the difference between the final warming onset results from the different mid-winter initial conditions. It normally takes much more time to decelerate the strong vortex zonal winds than weak vortex winds, so that the final warming date for the strong vortex is later.

We also follow Black et al. (2006) and Black and McDaniel (2007b) and analyze the final warmings in observations for the Northern and Southern Hemispheres. The Northern Hemisphere final warming mean onset date at 50 hPa is between the 1500-m and 2000-m topographic amplitude results from our model. The zero wind line in the Northern Hemisphere descends from 10 hPa to 50 hPa in only 7 days in observations, which is comparable with model results for 3000-m topography. The observed mean onset date of the final warming in the Southern Hemisphere is much later, due to the weakness of planetary waves. According to the zero wind line definition, final warmings do not always occur in the Southern Hemisphere. We then follow Black and McDaniel (2007b) to adjust the definition of the final warming using threshold zonal wind speeds of 5 m s^{-1} and 10 m s^{-1}. The larger value will result in an earlier onset date for the final warming. The delay from 10 hPa to 50 hPa is around 20 days, between 1500 m and 2000 m.

Histograms of the dates of occurrence for the 50-hPa final warming events with different topographic amplitudes are shown in Fig. 3.6, together with the observational results for the Northern and Southern Hemispheres in Fig. 3.7. Note that the 5 m s^{-1} threshold is used to define the Southern Hemisphere and 1500-m amplitude final warmings. The onset date in the model appears to be approximately normally distributed, as is the case for the observed Northern Hemisphere final warmings. The distribution of final warming dates

h_0 (m)	**m**	**u_1**	**Resolution**	**Definition**	**10-hPa**	**20-hPa**	**30-hPa**	**50-hPa**
0	1	280	R30	50°N	+162	*	*	*
500	1	280	R30	55°N	+159	*	*	*
1000	1	280	R30	60°N	+126	+140	*	*
1500	1	280	R30	65°N	+102	+111	+120	+139
2000	1	280	R30	70°N	+84	+89	+95	+101
2500	1	280	R30	70°N	+68	+73	+75	+82
3000	1	280	R30	70°N	+70	+70	+71	+75
2000	1	240	R30	70°N	+77	+83	+88	+97
2000	1	320	R30	70°N	+95	+100	+103	+110
2000	2	280	R30	70°N	+76	+78	+81	+91
2000	1	280	R60	70°N	+71	+72	+76	+80

Table 3.1: Stratospheric final warming 80-ensemble mean onset dates for different topographic forcing (h_0, m) , vortex strength (u_1) and horizontal resolution settings. The onset date is the date after the transition of equilibrium temperature begins. When the topographic forcing is weak, the final warming is defined at the latitudes of the mid-winter vortex and * means some final warmings do not occur according to the zero wind line definition.

	Definition	**10-hPa**	**20-hPa**	**30-hPa**	**50-hPa**
Northern Hemisphere	70°N (0m s^{-1})	+109	+108	+110	+116
Southern Hemisphere	60°S (0m s^{-1})	+156	+164	+170	*
Southern Hemisphere	60°S (5m s^{-1})	+150	+158	+163	+173
Southern Hemisphere	60°S (10m s^{-1})	+146	+153	+157	+165

Table 3.2: Northern and Southern Hemispheres mean final warming onset dates based on the same definition as Table 3.1. The final warming date is the date after the winter solstice, which is set to June 21 in the Southern Hemisphere, December 21 in the Northern Hemisphere. The zonal winds used to define the final warming come from NCEP/NCAR 1948 - 2008 reanalysis dataset.

in the Southern Hemisphere is more complicated. The observed dates may include trends resulting from anthropogenic ozone depletion.

3.3.2 Evolutions of the zonal wind during the final warming

We select an individual final warming case for each topographic amplitude, and display the time evolutions of the high-latitude zonal wind with respect to the onset time, in Fig. 3.8. When the topographic forcing is weak, the slow transition from westerlies to easterlies occurs only in the upper stratosphere. With the increase of topographic forcing, the transition becomes abrupt, and the zero wind line can descend to lower stratosphere. The tropospheric zonal winds are quiet for the weak topographic final warmings, but have a larger variability

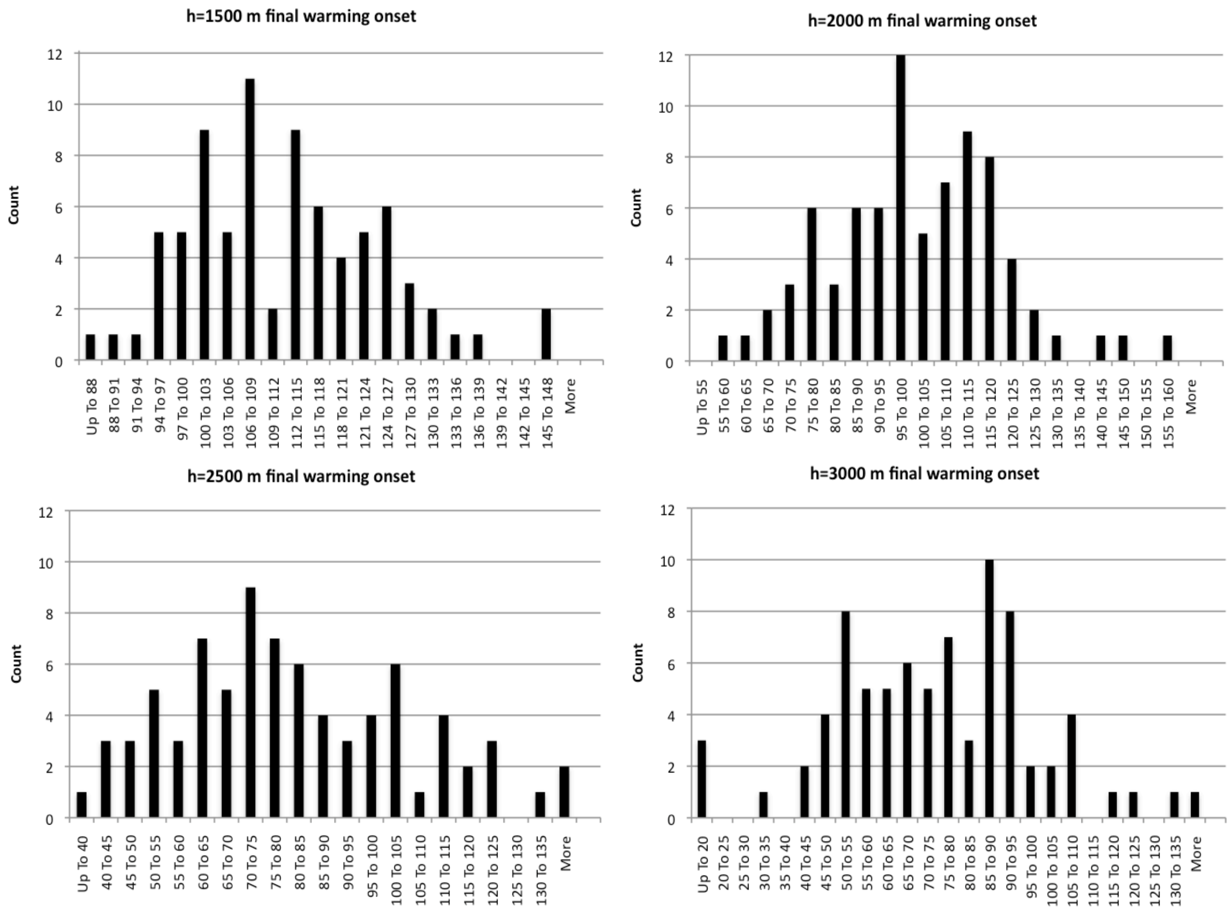
h=1500 m final warming onset

h=2000 m final warming onset

h=2500 m final warming onset

h=3000 m final warming onset

Figure 3.6: Histograms of the 80-member ensembles onset dates for the 50-hPa final warming events with different topographic amplitudes. Final warmings with 1500-m amplitude are defined at 5 m s^{-1} criterion, final warmings with other amplitudes are based on 0 m s^{-1} criterion.

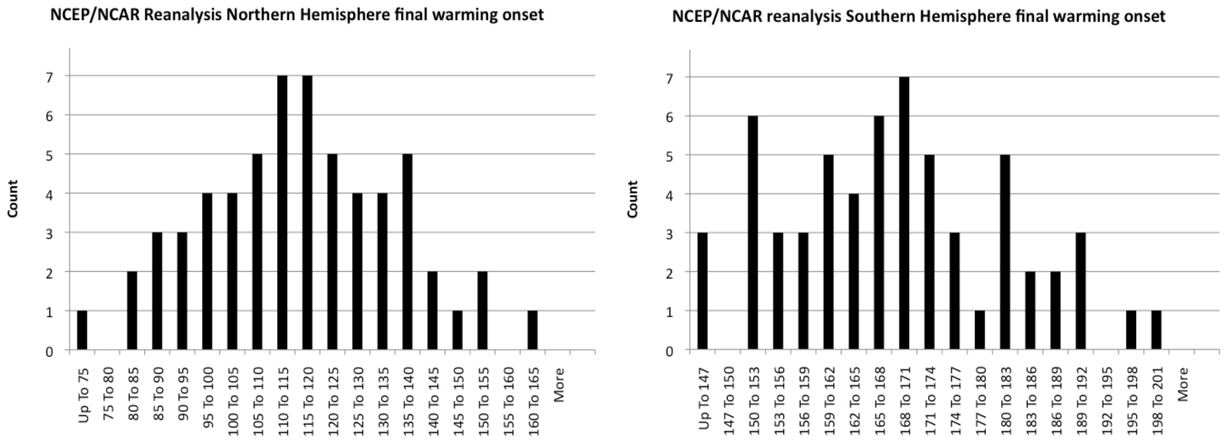
NCEP/NCAR Reanalysis Northern Hemisphere final warming onset

NCEP/NCAR reanalysis Southern Hemisphere final warming onset

Figure 3.7: NCEP/NCAR reanalysis data 1948 - 2008 final warming ensembles onset date histograms for the Northern and Southern Hemispheres. Northern Hemisphere final warmings are defined at 0 m s^{-1} criterion; Southern Hemisphere final warmings are based on 5 m s^{-1} criterion.

as the topographic forcing increases, and the tropospheric deceleration can be observed in response to the stratospheric transition.

After the final warming onset dates are determined, composites are constructed by performing ensemble averages with the time of each member shifted to align the onset times. This is different from the previously described climatological analysis, in which the time is based on the evolution of the equilibrium temperature T_{eq}. Composite anomaly fields are calculated by subtracting the ensemble climatology from the ensemble composites. In order to estimate the statistical significance of the anomalies, the student's t-test is used to calculate the 90% and 95% confidence levels. We also try a non-parametric test, Wilcoxon signed-rank test, which does not need the samples to be normally distributed, in order to avoid any possible mistakes. The calculations using these two statistical methods give almost the same results (see Fig. 3.17). This indicates that student's t-test is valid in the study.

Fig. 3.9 shows the evolution of the zonal wind climatologies and composites at 50 hPa and 70°N across the final warmings for different topographic amplitudes. The 50-hPa level is used to define the final warming. Thus from day -20 to day +20, the transition is characterized by the transition from westerlies prior to the final warming to easterlies afterwards. When the topographic amplitude is weak (500-m amplitude), no clear signal of transition appears in the composite or climatological zonal winds. For final warming with 1000-m topography, the zonal wind deceleration is clear, but the composite and climatological evolutions overlap. For stronger topography, the abrupt transition in the composite and the slower transition in the climatology are evident.

Similar features are also evident in the troposphere. Fig. 3.10 shows the results at 200 hPa and 70°N. Similar to the results at 50 hPa, the differences between the climatology and the composite are small when the topographic forcing is weak. For topography stronger than 1000 m, the composite zonal wind deceleration appears before the final warming, while the climatological transition is much smaller.

Fig. 3.9 and Fig. 3.10 characterize the high-latitude zonal wind transitions across the final warmings. Prior to the final warming, zonal winds decelerate not only in the stratosphere,

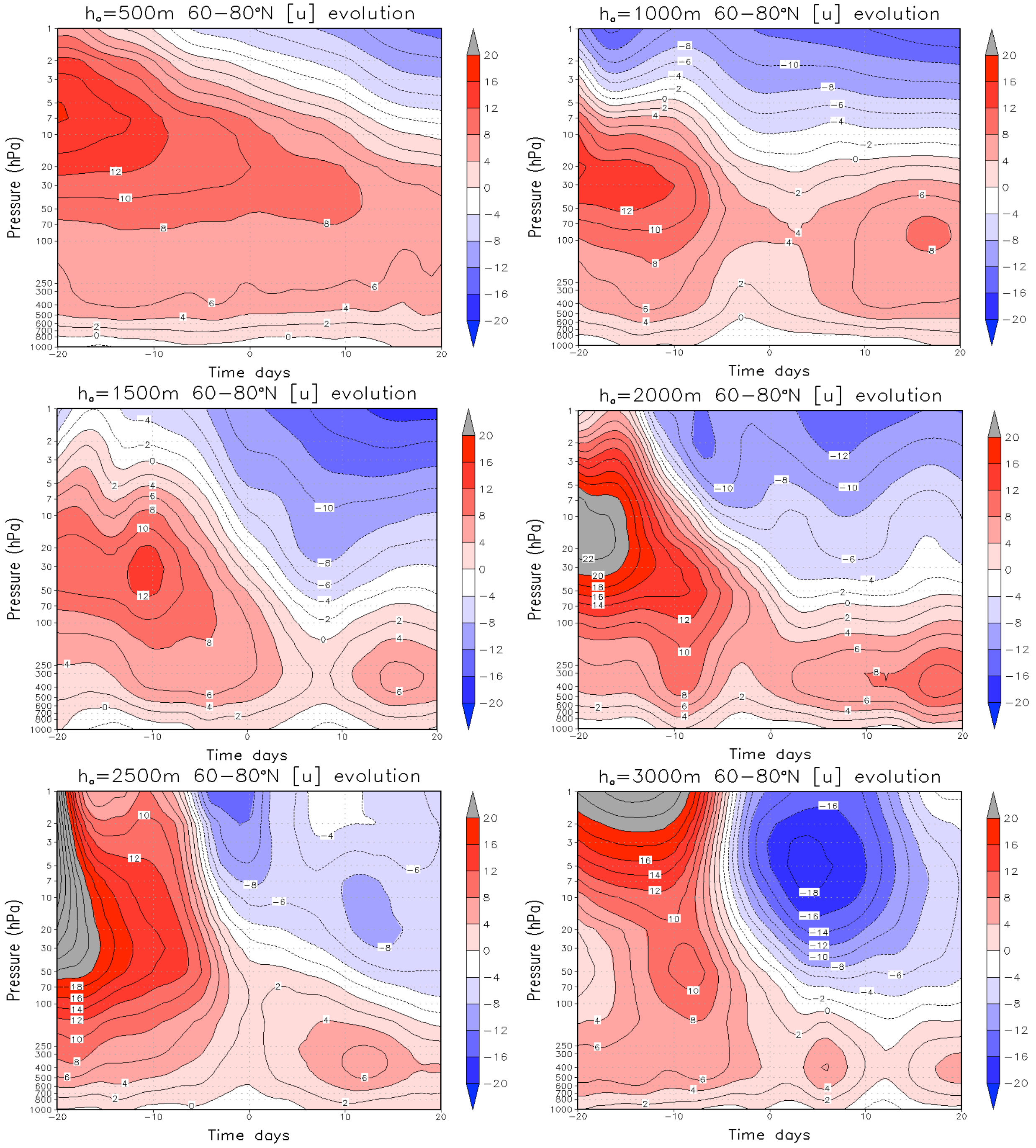

Figure 3.8: Time evolutions of zonal wind averaged over 60°-80°N for individual final warming events with different topographic amplitudes with respect to the onset time. The h_0=500, 1000, 1500-m final warmings are defined at 20, 10, 5 m s^{-1} criteria of 50 hPa zonal wind. The h_0=2000, 2500, 3000-m final warmings are defined at 0 m s^{-1} criteria of 50 hPa zonal wind. The onset dates for 500, 1000, 1500, 2000, 2500, 3000-m final warming cases are day +148, +132, +113, +101, +82, +74 after the T_{eq} transition, respectively. The contour interval is 2 m s^{-1}.

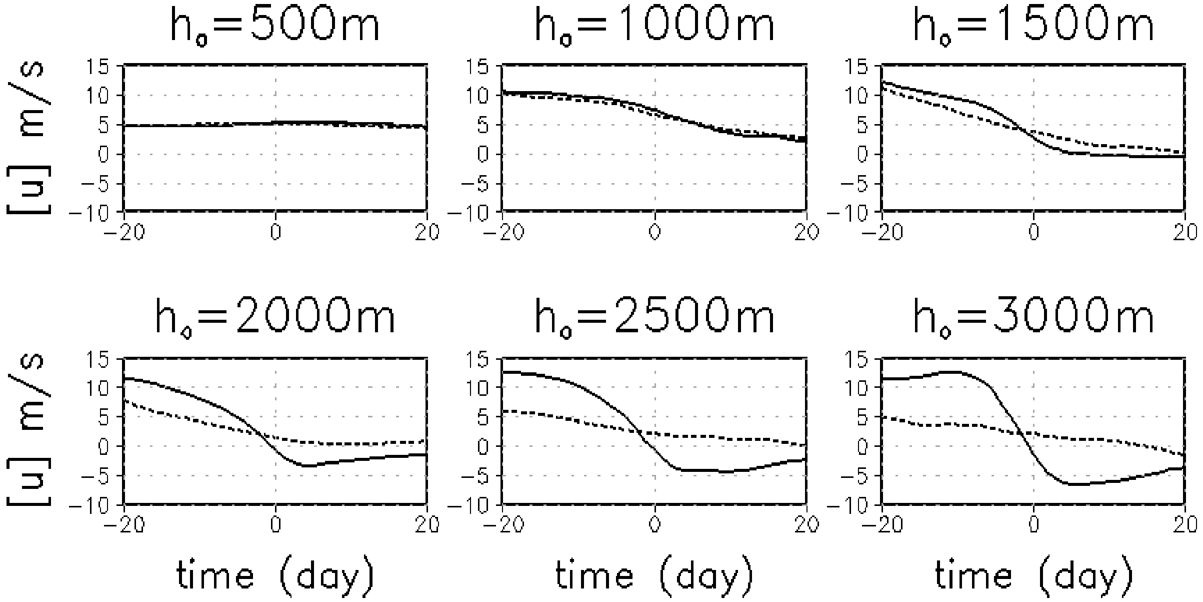

Figure 3.9: Climatological and composite zonal wind evolutions at 50 hPa and 70°N across the final warmings in the dynamical core. Xaxis is the date with respect to the final warming onset. Solid line is composite, dash line is climatology.

but also in the troposphere. Such decelerations, however, are much slower in the stratospheric climatology and are not evident at all in the tropospheric climatology, from which they are filtered by averaging. The tropospheric zonal wind transitions in the composite are tied to the date of the stratospheric final warming. Since the final warming occurs in the stratosphere, such tropospheric signals can arise only from the influence of stratospheric changes.

The evolutions of the zonal wind with different vortex strength are shown in Fig. 3.11. Although the onset times are different, the zonal wind transitions are similar in the stratosphere and the troposphere. Given that these three types of final warmings have the same topographic forcing and similar equilibrium temperatures near the final warming onset, the zonal wind transitions in the stratosphere and troposphere should be similar.

3.3.3 Robustness with the topographic forcings and resolution

Ensembles of final warmings with wave number 2 topographic forcing and with higher resolution, rhomboidal 60, are used to test the robustness of our results. The final warming mean onset dates for the wave number 2 topographic forcing are approximately 10 days earlier

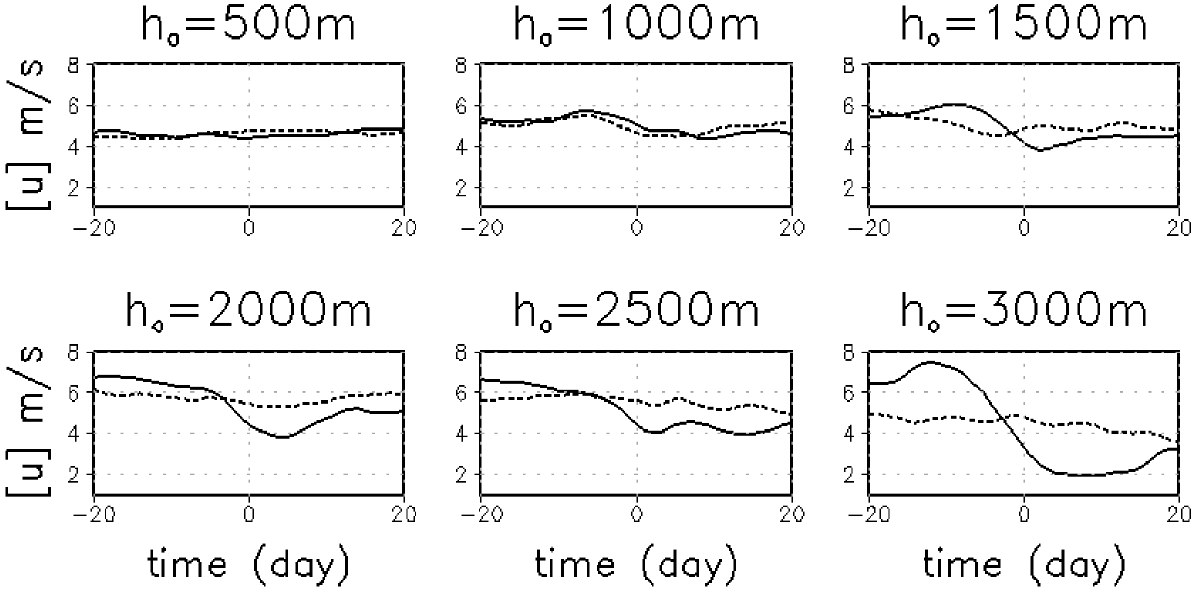

Figure 3.10: Climatology and composite zonal wind evolutions at 200 hPa and 70°N across the final warmings in the dynamical core. Xaxis is the date with respect to the final warming onset. Solid line is composite, dash line is climatology.

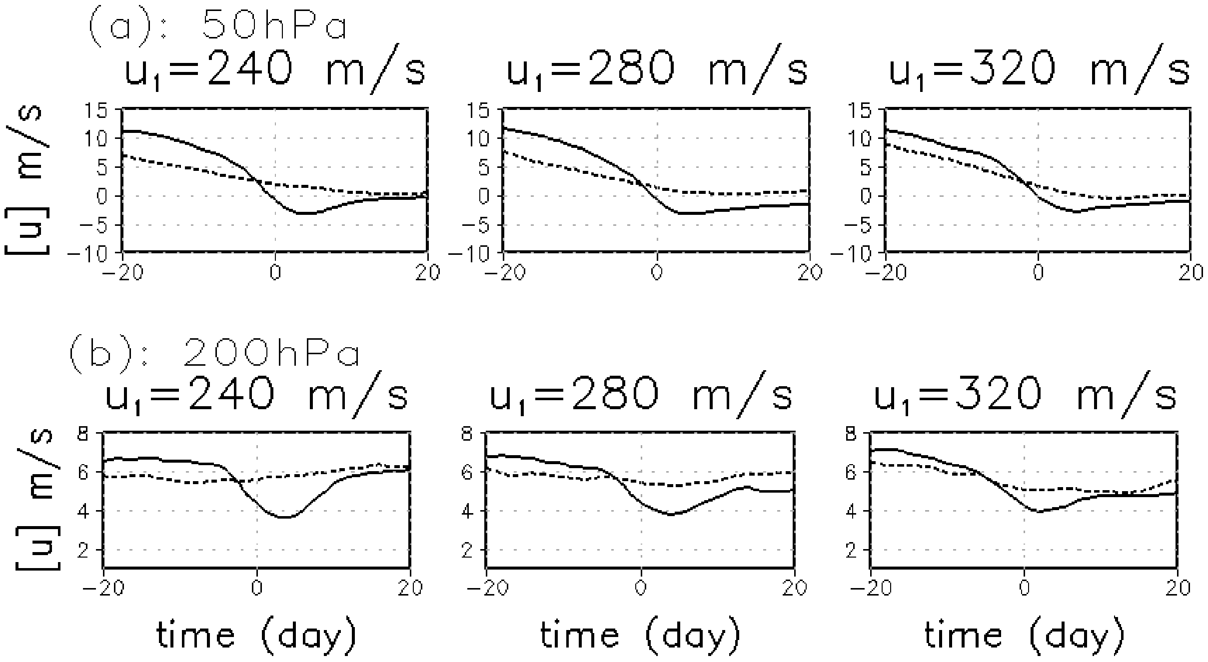

Figure 3.11: Climatology and composite zonal wind evolutions at (a) 50 hPa, (b) 200 hPa and 70°N across the final warmings for different vortex strength u_1 in the dynamical core. Xaxis is the date with respect to the final warming onset. Solid line is composite, dash line is climatology.

than for wave number 1 forcing (Table 3.1). Since the mid-winter polar vortex is similar in the perpetual runs using wave-2 and wave-1 topography, the early onset time of the wave number 2 final warmings implies that wave number 2 is more effective than wave number 1 in driving the zonal wind transition.

Similar to the perpetual run, we run the final warming with higher resolution to test the robustness of the results. With higher resolution, more waves are resolved and wave-mean flow interaction is stronger. This results in larger variability in the perpetual run and an earlier date for the final warming onset. From table 3.1, the mean onset date for R60 with 2000-m topography is comparable to the results for 3000-m topography at R30 resolution. The zero wind line descends from 10 to 50 hPa in 9 days, shorter than the 17 days for the R30 simulations.

The 50-hPa and 200-hPa zonal wind evolutions across the final warmings are shown in Fig. 3.12. Although there are differences for different wave number forcing and different resolution, the zonal wind deceleration in the composite is similar. This suggests that the zonal wind transition in the stratospheric final warming and its impact on the troposphere are robust.

3.4 Dynamics of the final warmings

In the previous section, we have displayed and discussed the composite and climatological zonal wind evolutions at 50 hPa and 200 hPa for different topographic amplitudes. When the topographic forcing is weak, both the composite and climatological zonal winds are characterized by a slow transition, mostly due to the radiative forcing, and there is little or no signal of the transition in the troposphere. This is similar to the Southern Hemisphere observations. In the observational analysis of final warmings by Black and McDaniel (2007b), the tropospheric zonal winds also undergo the tropospherically driven seasonal transition. Here, however, since the seasonal transition only occurs in the stratosphere, this tropospherically driven signal is absent. When the topographic forcing increases, the composite zonal wind

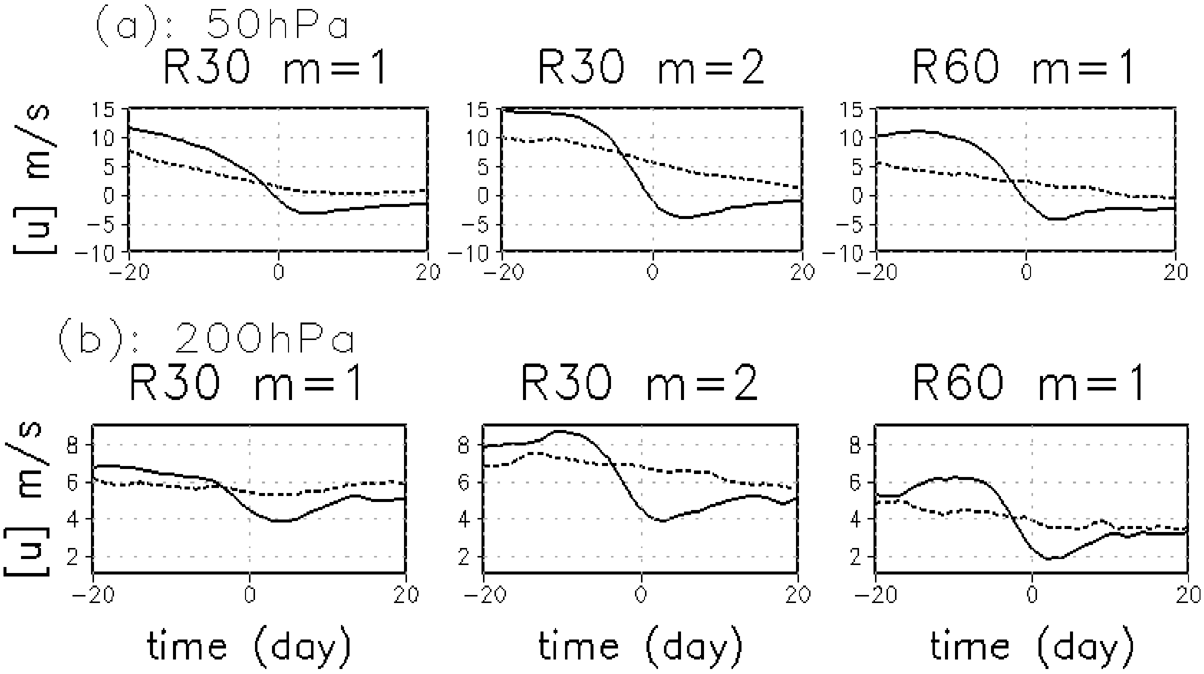

Figure 3.12: Climatology and composite zonal wind evolutions at (a) 50 hPa, (b) 200 hPa and 70°N across the final warmings for different wave number topographic forcing and resolutions in the dynamical core. Xaxis is the date with respect to the final warming onset. Solid line is composite, dash line is climatology.

evolution across the final warming becomes more abrupt while the climatological evolution is still slow. In the troposphere, this zonal wind deceleration is evident in the composite evolution. This indicates that the final warming can have a substantial impact on the tropospheric circulation, when the topographic forcing is sufficiently strong. This influence is robust, as it appears with different wave numbers for the topographic forcing and at different resolutions. The evolutions of the zonal winds in final warmings with strong topographic forcing are more similar to the Northern Hemisphere observations (Black et al., 2006). In this section, we choose 2000-m amplitude final warming as a strong topographic forcing event to study the dynamics of the final warmings.

We begin with an overview of the composite zonal wind evolutions surrounding the time of the final warming onset. The composite zonal mean zonal wind is shown in Fig. 3.13. Twenty days prior to the final warming onset, the extratropical stratosphere is dominated by a westerly polar vortex. Over the next twenty days, the mid to high latitude westerlies dramatically weaken and easterlies appear; and the zero wind line descends from the upper stratosphere to the lower stratosphere. After the onset, the polar vortex breaks up and the easterlies prevail in the stratosphere. The stratosphere and troposphere reach quasi-steady state with some relaxation back to the winter state in the upper stratosphere.

The evolution of zonal wind anomaly shown in Fig. 3.14 reveals the changes with respect to the climatology. At day -20, there is a clear dipole pattern with positive anomalies in the extratropics and negative anomalies in the subtropics. Thereafter, the positive anomalies weaken quickly and become negative anomalies, first appearing in the upper stratosphere, then extending downward until they reach surface at day 0. After the final warming onset, the negative anomalies persist for several days, gradually weakening and finally disappearing after day +20.

The evolutions of the zonal winds shown in Fig. 3.13 and Fig. 3.14 are similar to the Northern Hemisphere observations from Black and McDaniel (2007a). The coherent extension of the zonal wind anomalies from the stratosphere to the surface suggests that as a stratospheric event, the final warming also has a substantial impact on the troposphere. More specifically, the transition between the positive anomaly at day -20 to negative anomaly at day 0 in both the stratosphere and troposphere indicates that when the final warming occurs, the troposphere experiences a notable zonal wind deceleration. Since in our final warming simulations, the tropospheric T_{eq} remains unchanged, this tropospheric zonal wind change can be attributed to the downward influence from the stratosphere.

The zonal wind changes seen in the final warming results have two possible sources: either diabatic heating from solar radiation, or waves. It is well known that the midwinter sudden warming is linked to anomalous planetary waves emanating from the troposphere (Limpasuvan et al., 2004). The final warming here, is also closely connected to the planetary wave activity. Without eddies, the zonal wind seasonal transition can be simulated in the zonally symmetric model. It is found that the transition due to diabatic heating alone is characterized by a slow transition, limited to the stratosphere. Thus the coherent extension of the zonal wind anomaly seen in Fig. 3.14, must come from the contributions from waves.

Fig. 3.15 shows the evolution of anomalies in the long-wave (wavenumber 1 - 3) Eliassen-

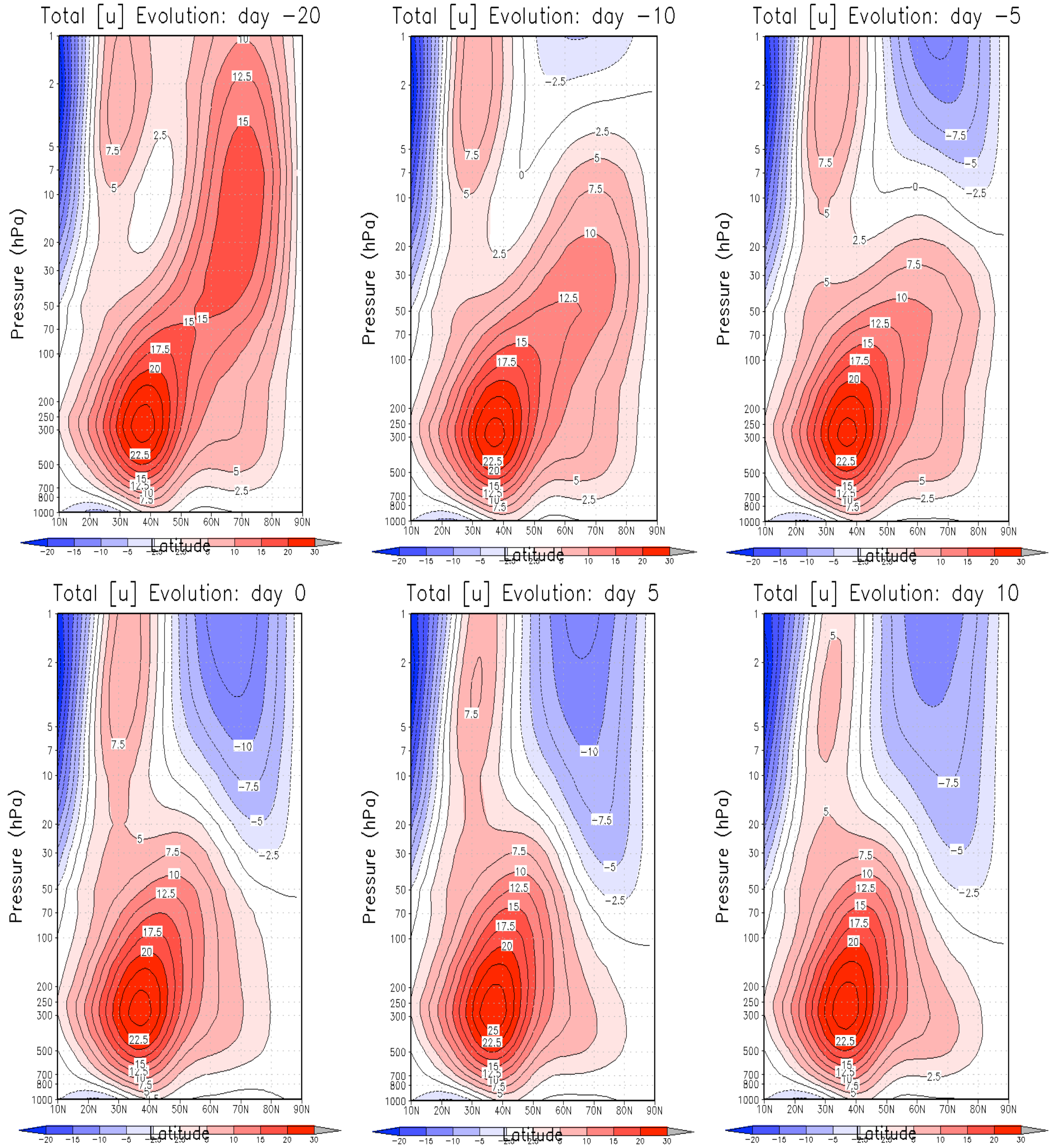

Figure 3.13: Time evolutions of zonal mean zonal wind for h_0=2000-m final warming events with respect to the onset time. The contour interval is 2.5 m s^{-1}.

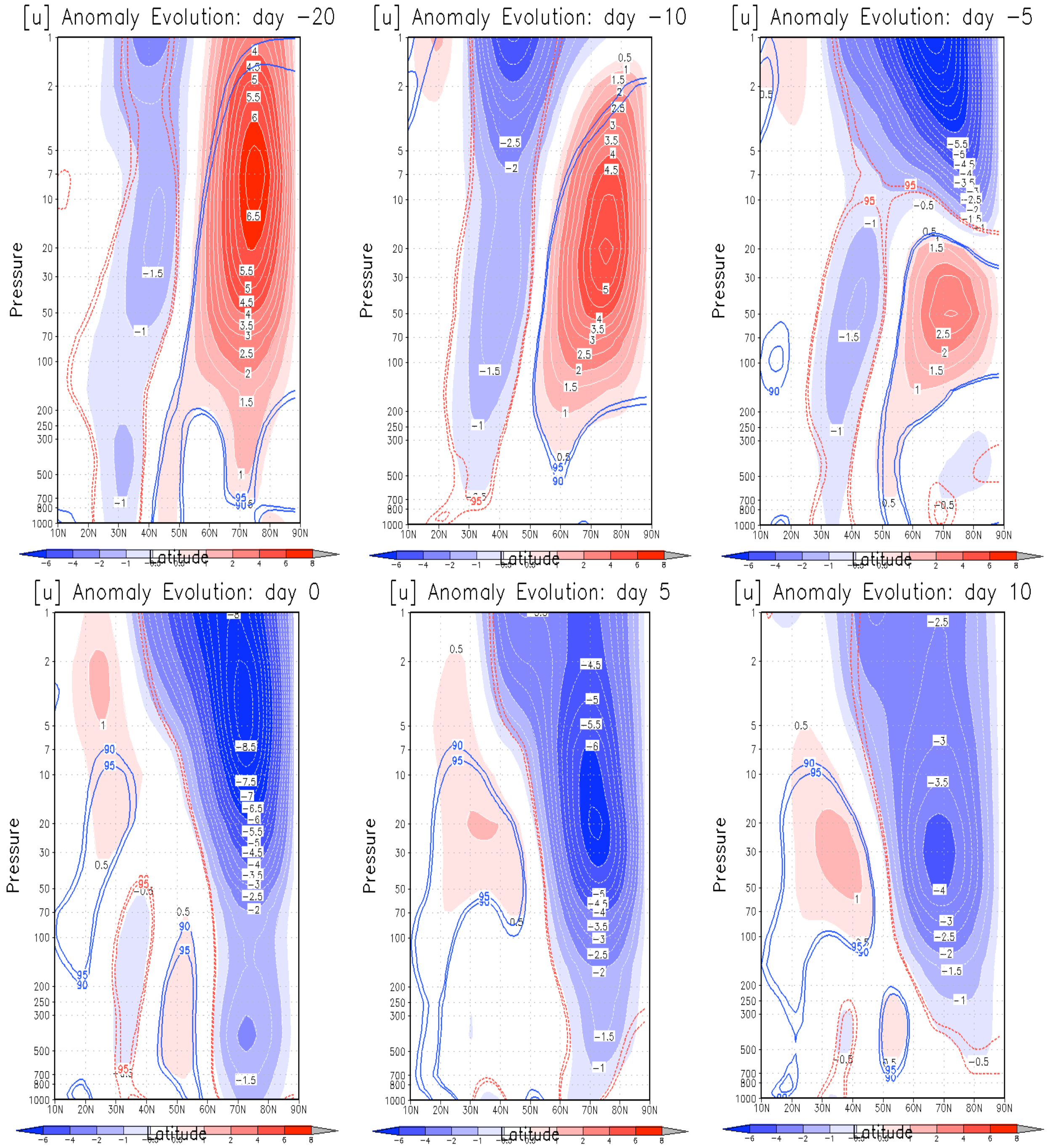

Figure 3.14: Time evolutions of anomalous zonal wind for h_0=2000-m final warming events with respect to the onset time. The contour interval is 0.5 m s^{-1}. Colored contours indicate the 90% and 95% confidence levels from a two-sided Student's t-test.

Palm flux vector and divergence across the onset of the final warming. The Eliassen-Palm flux convergence first appears in the mid-latitude upper stratosphere (day -20). This signal amplifies and shifts poleward and downward. While the Eliassen-Palm flux convergence amplifies, an enhanced upward Eliassen-Palm flux appears in the stratosphere and upper troposphere. The convergence anomaly peaks around the time of the final warming onset and then weakens. By day +10, the Eliassen-Palm flux is anomalously divergent in the stratosphere, and the anomalous flux vectors are downward after day +10.

Kuroda and Kodera (1999) discussed a slow clockwise rotation of zonal wind anomalies and wave driving in the Northern Hemisphere in the latitude-height plane. A similar feature is observed in our final warming simulations, where the zonal wind deceleration due to planetary waves first appears in the mid-latitude upper stratosphere, then shifts poleward and downward.

Since most of the zonal wind and wave anomalies are in high-latitude, we can summarize the evolution of the final warming by plotting the high-latitude behavior. The results, averaged over 65^o - 75^oN, for the climatological and composite zonal winds, are shown in Fig. 3.16. The climatology is characterized by a slow transition from a winter state with westerlies to a quasi-steady summer state with easterlies in the stratosphere and a weak jet in the upper troposphere. There is very little change in the lower troposphere. In contrast, the composite zonal wind transition is much more abrupt, in both the stratosphere and the troposphere. After the onset of the final warming, the composite zonal wind recovers slightly back in the stratosphere due to the absence of planetary waves. The composite better reflects the typical evolution of the zonal wind, because it avoids the averaging over events at different times that occurs in forming the climatology.

The zonal wind anomalies, Fig. 3.17, shows statistically significant positive anomalies prior to the final warming and negative anomalies afterwards, implying a larger zonal wind deceleration process in the composite than the climatology. The negative anomalies extend coherently downward to the surface. The zonal wind changes are closely connected to the wave activity, as shown from the long wave Eliassen-Palm flux vector and divergence. The

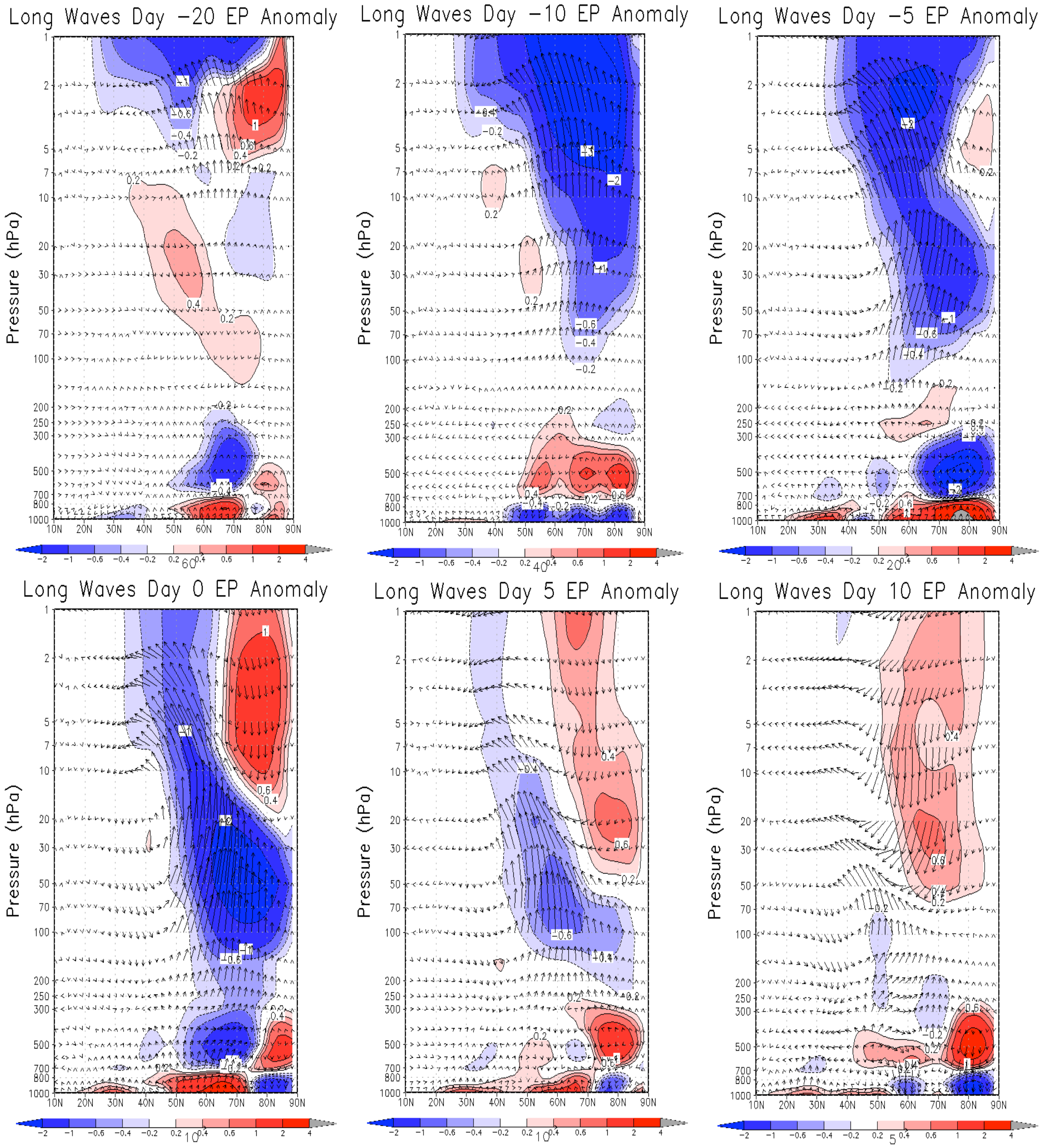

Figure 3.15: Time evolutions of anomalous Eliassen-Palm vector and divergence for h_0=2000-m final warming events with respect to the onset time. The contour interval is not uniform in order to better show the stratospheric changes. The unit of Eliassen-Palm divergence is m s^{-1} day^{-1}.

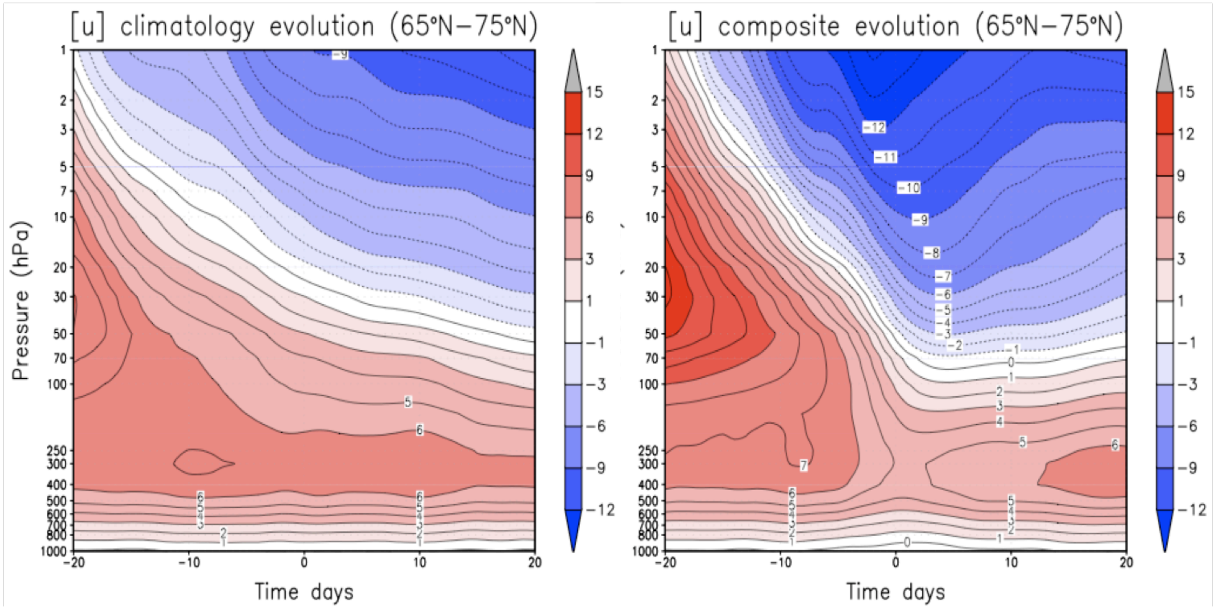

Figure 3.16: Climatological and its parallel composite zonal wind evolutions averaged over 65^{o}N-75^{o}N for h_0=2000-m final warming events. The contour interval is 1 m s^{-1}.

transition of the zonal wind anomalies from positive to negative is accompanied by upward anomalous Eliassen-Palm flux vectors and a large anomaly in the Eliassen-Palm flux convergence occurs prior to the final warming events. The zonal wind and wave evolutions in our simulation are similar to the Northern Hemisphere observations by Black et al. (2006).

3.5 Discussion and conclusion

In this chapter, 80-member ensembles of seasonal transition are obtained by imposing a seasonal transition in the stratospheric radiative equilibrium temperatures. These results permit us to analyze the resulting final warming events. The strength of the topographic forcing is found to have a large impact on the seasonal cycle and on the final warming. For the seasonal cycle, the winter state with weak (strong) topographic forcing is characterized by small (large) interannual variability in the stratosphere. This is consistent with the observations (Labitzke, 1977) and with other simulations (Taguchi et al., 2002). The winter state with weak topography has two Eliassen-Palm flux convergence: a weak one in the early winter and a strong one in the late winter. The latter time coincides with the climatological

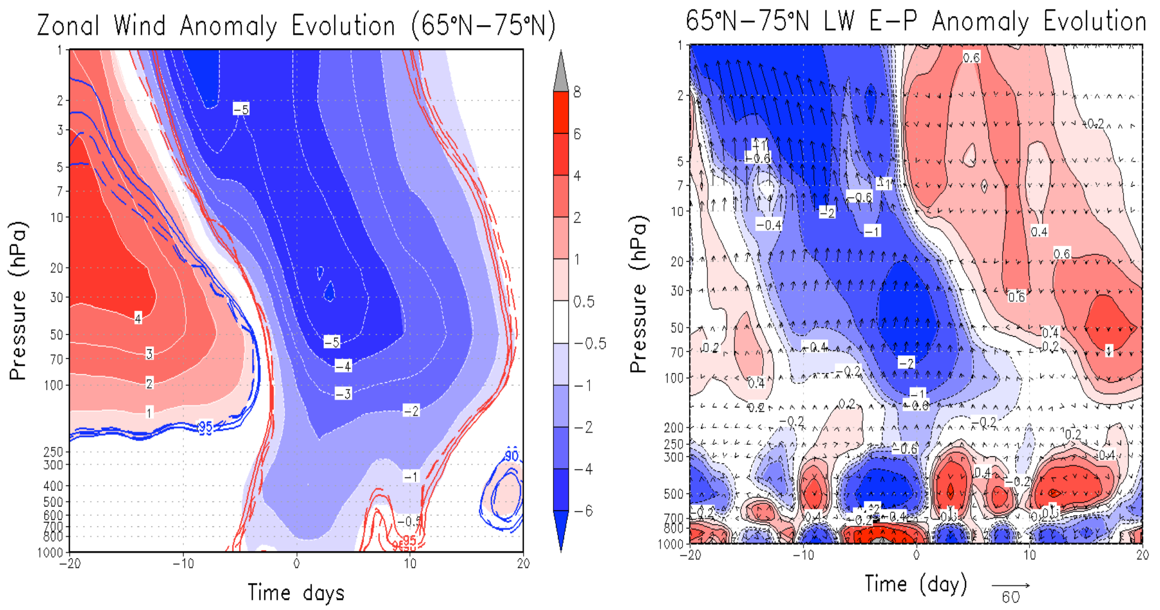

Figure 3.17: Composite (left) anomalous zonal wind and (right) long-wave (number 1- 3) Eliassen-Palm flux evolutions averaged over 65°N-75°N for h_0=2000-m final warming events. The colored solid contours indicate the 90% and 95% confidence levels from a two-sided Student's t-test.; the colored dash contours in the left figure indicate the 90% and 95% confidence levels from a Wilcoxon signed-rank test. The unit of Eliassen-Palm divergence is m s^{-1} day^{-1}.

final warming. For strong topographic forcing, the quasi-stationary planetary waves are active throughout the winter. The wave patterns for different topographic forcings are similar to the observed asymmetry in planetary waves between two hemispheres (Randel, 1988). This consistency suggests that our seasonal results are reasonable and encourages us in pursuing our analyses of the modeled final warming.

In our final warming results, the timing of the final warming depends on both the initial vortex strength and wave activity. In our vortex strength experiment, since three final warming cases have the same topographic forcings, the differences in onset time should come from the different strengths of the initial mid-winter vortex. A stronger (weaker) mid-winter vortex normally results in a later (earlier) final warming. The waves, of course, are also important in determining the timing of the final warming. With weak topographic forcing, the final warming does not occur in the lower stratosphere. In our model, the time required for the zero wind line to descend from 10 hPa to 50 hPa is longer than in observations, but it is consistent with the fact that Northern Hemisphere final warming is much earlier than the Southern Hemisphere (Table 3.2). The timing of the final warmings will be discussed more in Chapter 5, when we explore the predictability of the final warming.

The evolution of the climatological and composite zonal winds and planetary waves with different topographic forcings are obtained. The zonal wind evolution with weak forcing is characterized by a slow transition, mostly following the evolution of the radiative equilibrium temperature. The composite zonal wind evolution with strong topographic forcing, however, is much more abrupt than the climatology. For the anomalous zonal winds, the statistical significant positive (negative) anomalies prior to (after) the final warming onset are observed. These anomalies extend downward to the surface. The anomaly structures are robust to the changes in the wave forcing and the resolution. The composite zonal wind deceleration across the final warming is closely connected to a burst in planetary wave activity.

In summary, large ensembles of final warming events are obtained by by imposing a seasonal transition in the stratospheric equilibrium temperature in a dynamical core model. The composite zonal wind evolutions clearly show that when the stratosphere experiences the transition from wintertime to summertime, the high-latitude tropospheric zonal winds also decelerate. With the increase of topographic forcing, the stratospheric transition becomes more abrupt, and the tropospheric changes also become larger. The transitions with weak and strong topographic forcings resemble the observations of final warmings in the Southern and Northern Hemispheres (Black et al., 2006; Black and McDaniel, 2007b). In the dynamical core, since the radiative seasonal transition occurs only in the stratosphere, these tropospheric signals unquestionably come from the downward influence of the stratosphere. This suggests that much of the observed tropospheric signal during final warmings is initiated from the stratosphere.

Chapter 4

Explore the mechanisms of the downward influence

4.1 Introduction

In Chapter 3, analyses of ensembles of final warming simulations revealed that prior to the final warmings there is zonal wind deceleration not only in the stratosphere but also in the troposphere. Since the stratosphere undergoes a seasonal transition driven by increased insolation, extratropical zonal winds are expected to decrease in the stratosphere. The tropospheric equilibrium temperature is kept unchanged in our seasonal transition, so the zonal wind changes can be attributed to the downward influence from the stratosphere. Using different diagnostic methods, we investigate the connection between the troposphere signals and the planetary waves, and we test our second hypothesis that the planetary waves are crucial in the observed downward influence of the final warmings.

It is well recognized that the tropospheric planetary waves propagate upward into the stratosphere and slow the zonal wind through wave-mean flow interaction. The mechanisms by which the stratosphere can affect the troposphere, however, are more complex and still not understood. One way to understand the downward influence is to consider the equations for angular momentum, mass conservation and conservation of energy. Here we follow Plumb (2009) and state these equations as:

$$\frac{\partial M}{\partial t} + \bar{v}_* \cdot \nabla M = \frac{a \cos\phi}{\rho} \nabla \cdot \mathrm{F}$$

$$\frac{\partial \rho}{\partial t} + \nabla \cdot \rho \bar{v}_* = 0$$

$$\frac{\partial\bar{\theta}}{\partial t} + \bar{v}_* \cdot \nabla\bar{\theta} = \frac{1}{\rho c_p}(\frac{p_0}{p})^\kappa J$$

where $M = \Omega a^2 \cos^2\phi + \bar{u}a\cos\phi$ is the specific mean absolute angular momentum, $\bar{v}_* = (\bar{v}_*, \bar{w}_*)$ the meridional residual circulation, ρ is the density, θ is the potential temperature, p is the pressure, $p_0 = 1000$ hPa, c_p is the specific heat of air at constant pressure, $\kappa = 2/7$, and J is the diabatic heating rate.

Considering a steady state, if there is no eddy forcing, so that $\nabla \cdot \mathrm{F} = 0$, then the angular momentum equation implies that there can be no flow across angular momentum surfaces. Since the angular momentum surfaces are nearly vertical in extratropical latitudes (Haynes et al., 1991), it follows that there is no meridional circulation. Then from the thermodynamic equation there is no diabatic heating, and the temperatures are in radiative equilibrium.

When the planetary waves are present, $\nabla \cdot \mathrm{F} < 0$ where there is dissipation, so that these waves act as a drag on the westerly mean flow. Angular momentum decreases poleward in the extratropical stratosphere, so that, in steady state zonal drag induces a mean poleward meridional flow across the angular momentum contours. Mass conservation requires corresponding vertical motion, so that there is upward (downward) motion equatorward (poleward) of the wave drag. The flow returns near the surface by virtue either of frictional or topographic form drag at the surface, or in a region of Eliassen-Palm flux divergence if the waves are forced internally (Plumb, 2009). Thus, the meridional residual circulation can be deduced, without consideration of the thermodynamic equation, and it can be used to explain the downward influence of the stratospheric wave drag on the tropospheric circulation.

This mechanism is often called "downward control" of the extratropical meridional circulation by planetary waves. The details can be found in Haynes et al. (1991), and in the review by Holton et al. (1995) (cf. Haynes (2005), Plumb (2009)). In unsteady situations, there is a little difference. Fig. 4.1 shows the meridional circulation deduced by different frequencies of westward wave drag. Since the density decrease with altitude, the mass circulation is dominated by the lower branch. Thus the meridional circulation and its consequences are not qualitatively different from the steady case, despite a broader in horizontal extend (Haynes et al., 1991).

The downward control theory has been used to explain phenomenon related to the stratosphere-troposphere exchange, for example the Brewer-Dobson circulation (Plumb and Eluszkiewicz, 1999; Randel et al., 2008). The tropospheric signals calculated from such theory are, however, much weaker than observed. For example, Song and Robinson (2004) assumed a typical anomaly in stratospheric wave driving on the order of 1 m s^{-1} day^{-1} and distributed over a stratospheric layer 50-hPa deep, if the boundary layer has a thickness of 100 hPa and the time scale for the drag in the boundary layer is 1 day, then the equilibrated surface wind in response to the stratospheric wave driving is around 0.5 m s^{-1}, much weaker than is implied by observations.

Kushner and Polvani (2004) suggested that the tropospheric synoptic-eddy feedback, as mentioned by Robinson (1991, 1994, 2000), can amplify the stratospheric signals transmitted from the stratosphere by downward control. Further studies by Song and Robinson (2004) revealed that considering both the downward control and tropospheric eddy feedback is still insufficient to explain the tropospheric response to stratospheric forcing they obtained in their model. They suggested that the planetary waves themselves also play a role in transmitting stratospheric signals downward, even when the planetary waves are weak.

Another possible mechanism associated with the planetary wave reflection was proposed by Perlwitz and Harnik (2003, 2004). They used a time-lagged singular value decomposition analysis to isolate signals of downward propagating wave number one. When the wave-one pattern in the stratosphere lead that in the troposphere, statistical significant lag-correlations for time lags were obtained. In the Northern Hemisphere, they found evidence for wave-one coupling between the stratosphere and troposphere during the strong-vortex months of the winter (January, February and March). The wave is reflected in the stratosphere, above 10 hPa. Their further studies suggested that whether or not wave refection dominates depends on the basic state of the winter. The stratosphere can affect the troposphere either by reflecting wave number one, in reflective years, or by connecting the zonal mean fields in

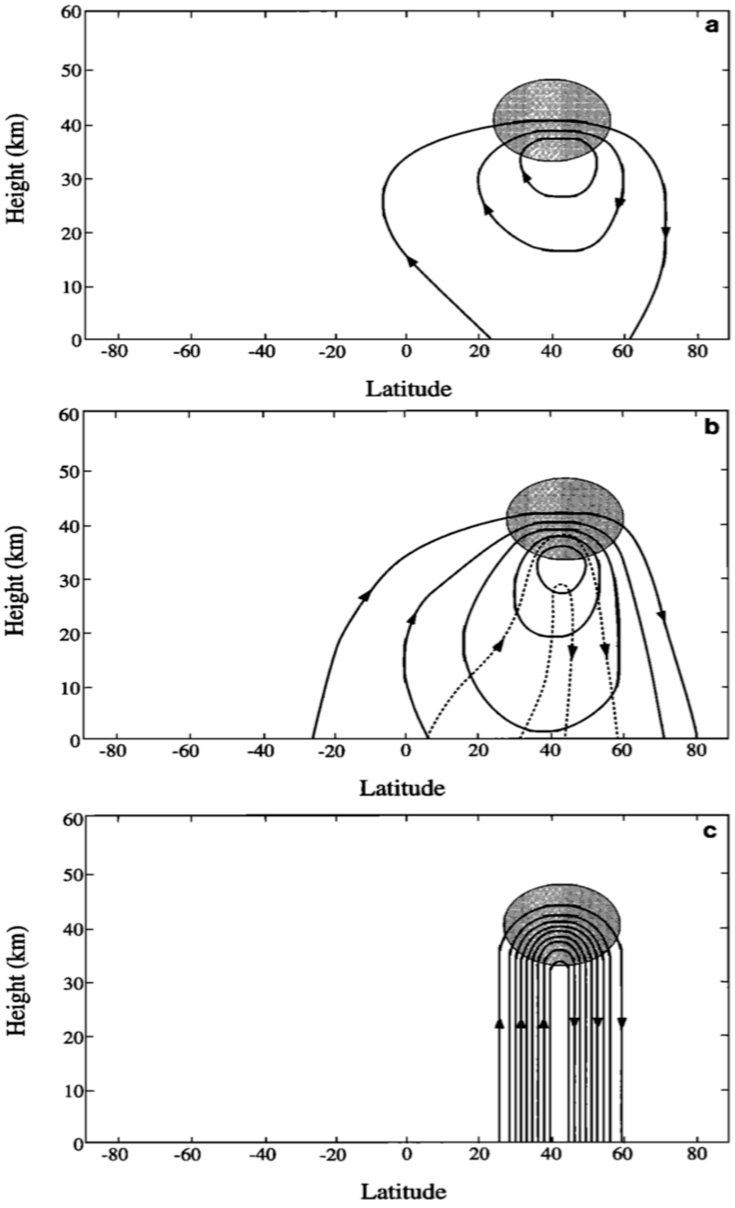

Figure 4.1: Idealized numerical experiments on the response of the mean stratospheric zonally symmetric circulation in the latitude-height plane to a westward force applied in the shade region. Contours are streamlines, with the same contour interval used in each panel. (a) Adiabatic response for $\sigma/\alpha \gg 1$. (b) Response for $\sigma/\alpha = 0.34$, corresponding to annual frequency and 20-day radiative damping time-scale; the solid and dashed contours show the response that is in phase and 90^o out of phase with the forcing, respectively. (c) Steady state response ($\sigma/\alpha \ll 1$). The model is unbounded below, so the ordinate has arbitrary origin but can be regarded, for instance, as showing approximate vertical distance above the lower boundary of the overworld. The figure comes from Holton et al. (1995). (Copyright 1995 American Geophysical Union. Reproduced by permission of American Geophysical Union.)

other ways (e.g. downward control), in non-reflective years. Shaw et al. (2010) compared the relative roles of downward wave and zonal-mean coupling and found that in the Southern Hemisphere, downward wave-one coupling dominates, while in the Northern Hemisphere, downward wave-one coupling and zonal-mean coupling are equally important from winter to early spring. In addition to wave reflection, Chen and Robinson (1992) indicated that the propagation of planetary waves is sensitive to the wind shear across the extratropical tropopause. Black and McDaniel (2007a) suggested that the stratosphere could influence the troposphere by trapping tropospheric planetary waves during final warmings.

In this chapter, we investigate the downward influence of the final warming on the troposphere circulation in different ways. In section 4.2, by comparing the effects of long waves with that of short waves, we resolve whether tropospheric eddy feedback is important in the final warmings. Section 4.3 describes an analysis of the momentum budget, performed to understand the source of the tropospheric deceleration prior to the onset of the final warming. Since the zonally symmetric model computes its own secondary circulation, in section 4.4 we use this model to study how stratospheric wave driving affects the troposphere by inducing a residual circulation, as in the downward control theory. The final section includes discussions and conclusions.

4.2 The roles of planetary waves in the final warmings

Tropospheric synoptic eddies are important in amplifying the signals transmitted from the stratosphere (e.g. Kushner and Polvani (2004), Song and Robinson (2004)). Without topography, Song and Robinson (2004) found that short waves are primarily responsible for the tropospheric response to the stratospheric wave driving, though the influence of planetary waves is not negligible (Fig. 10 of their paper). Most of the planetary wave driving, in their model, is associated with wave number 3. In this study, wave number 1 topographic forcing is added to the model and the situation is different.

We estimate the roles of planetary waves by separating the long wave (number 1 - 3) from

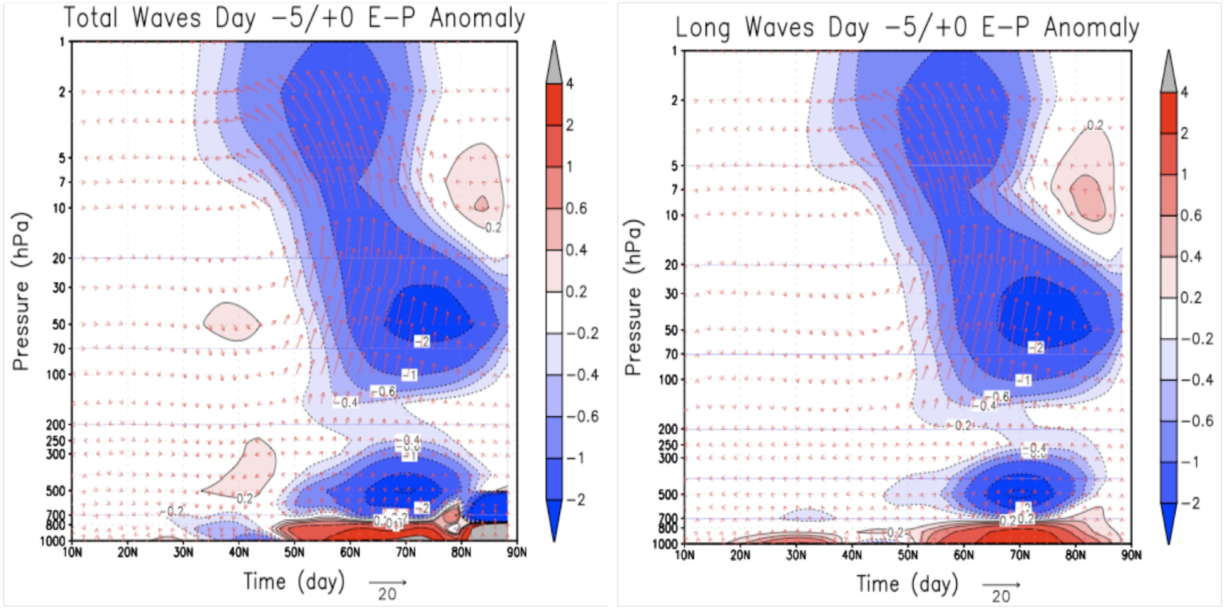

(a)

(b)

Figure 4.2: Anomalous Eliassen-Palm flux vector and Eliassen-Palm divergence averaged over day -5/0 with respect to the final warming onset for the (a) total waves and (b) long waves. The unit of the Eliassen-Palm divergence is m s^{-1} day^{-1}.

short wave Eliassen-Palm flux divergence. Fig. 4.2 shows the comparison of the anomalous Eliassen-Palm flux divergence averaged over day -5/0 for the total waves and long waves only. During this stage, the zonal wind decelerations occur in the stratosphere and troposphere. The upward Eliassen-Palm flux and Eliassen-Palm flux convergence in the extratropical stratosphere are responsible for the stratospheric deceleration. In the troposphere, there is a vertically oriented dipole in wave driving centered around 70^oN with convergence above 700 hPa and divergence below. This is similar to the wave number 3 structure shown in Fig. 11 of Song and Robinson (2004). The similarity between the total waves and long waves reveals that the wave activity that causes the zonal wind decelerations is mostly due to the long waves, not only in the stratosphere, but in the troposphere. It suggests that the downward influence of the final warming is process that involves interactions between long waves and the zonal mean flow, in the high-latitudes where the tropospheric synoptic-eddy feedback is not important.

4.3 Momentum budget analysis

In Chapter 3, we found that the zonal wind decelerations prior to the final warming are closely connected to the wave activity. Section 4.2 indicates that most of the responsible activity comes from the contribution of long waves. This is not enough, however, for us to understand why there is zonal wind deceleration in the troposphere. An analysis of the momentum budget can help to determine the roles of different terms in driving the zonal wind deceleration prior to the final warming, and so to understand better the mechanisms for the downward influence of final warmings.

From the Transformed Eulerian Mean momentum equation (.10), without considering the tendency of $\overline{(P_s' u')}_t$ term but including the near-surface drag,

$$\underbrace{\overline{P}_s \frac{\partial \bar{u}}{\partial t}}_{\text{tendency}} + \underbrace{\alpha\,\bar{v}^* + \beta\,\bar{\omega}^*}_{\text{circulation}} = \underbrace{-\frac{1}{\cos\phi}\{\overbrace{\frac{1}{a\cos\phi}\frac{\partial[\mathrm{F}^{(\phi)}]}{\partial\phi}}^{\text{Horizontal}} + \overbrace{\frac{\partial[\mathrm{F}^{(\sigma)}]}{\partial\sigma}}^{\text{Vertical}} + \overbrace{\frac{1}{a}\overline{P_s'\frac{\partial\Psi'}{\partial\lambda}}}^{\text{Form drag}}\}}_{\text{Eliassen-Palm divergence}} \underbrace{-k\bar{u}}_{\text{Friction}}$$

where $\overline{P}_s$ is the zonal mean surface pressure, the residual circulation $v = (\bar{v}^*, \bar{\omega}^*)$, $\alpha = \frac{1}{a\cos\phi}\frac{\partial(\bar{u}\cos\phi)}{\partial\phi} - 2\Omega\cos\phi$, $\beta = \bar{u}_\sigma$, $\mathrm{F}^{(\phi)}$ and $\mathrm{F}^{(\sigma)}$ are the horizontal and vertical Eliassen-Palm flux. In the σ coordinates, there is an extra form drag term on the right-hand side of the equation, which cannot be explained as the divergence of a flux. For the residual circulation, the $\overline{\omega}^*$ term is found to be much smaller than $\overline{v}^*$ term. From this equation, the stratosphere can affect the tropospheric circulation in two possible ways:

1. By changing the tropospehric residual circulation: This part of the change is attributed to the tropospheric geostrophic and hydrostatic adjustment to the stratospheric change, such as in the downward control theory (Haynes et al., 1991) in the steady state. When the stratosphere experiences the seasonal transition, it can also result in changes in the tropospheric residual circulation, which then affect the zonal winds (Thompson et al., 2006).

2. By changing the tropospheric waves: The stratosphere can affect the tropospheric plan-

etary wave propagation, either by wave reflection (Perlwitz and Harnik, 2003, 2004), wave trapping(Chen and Robinson, 1992; Black and McDaniel, 2007a) or resonance (Plumb, 2009).

Next, we carry out the Transformed Eulerian Mean momentum-budget analysis for the perpetual winter and final warming. In the long-term mean perpetual winter state, there is a rough balance among the residual circulation, waves and friction, and the zonal-wind tendency term is negligible. The zonal-wind tendency cannot be neglected in the final warming. By calculating each term in the momentum equation, the roles of residual circulation, waves and friction in determining the stratospheric and tropospheric zonal wind deceleration can be estimated and compared.

4.3.1 Winter state

We begin with the Transformed Eulerian Mean momentum-budget analysis for the perpetual winter state. The 2000 - 4000 day averaged momentum budgets at 10 hPa, 100 hPa, 500 hPa and 850 hPa are shown in Fig. 4.3. In the long-term mean of the perpetual winter state, the zonal wind tendency $\frac{\partial \bar{u}}{\partial t}$ can be neglected. This is confirmed in Fig. 4.3 which shows that the combination of the three Eliassen-Palm flux divergence terms and friction balance the residual circulation term.

At different pressure levels, the magnitudes of terms in the momentum equation are different. The friction is negligible except near the surface, where it reaches 3 m s^{-1} day^{-1}, but is still much smaller than the residual circulation and vertical Eliassen-Palm flux divergence.

In the mid-stratosphere, the magnitude of the vertical Eliassen-Palm flux divergence is largest, it is opposed by both the horizontal Eliassen-Palm flux divergence and by the form drag. The magnitude of the residual circulation is smaller than the vertical Eliassen-Palm flux divergence and is balanced by the total Eliassen-Palm flux divergence. In contrast to the perpetual winter in the Northern Hemisphere, all four terms in the Southern Hemisphere are negligible due to the absence of planetary waves in the summer.

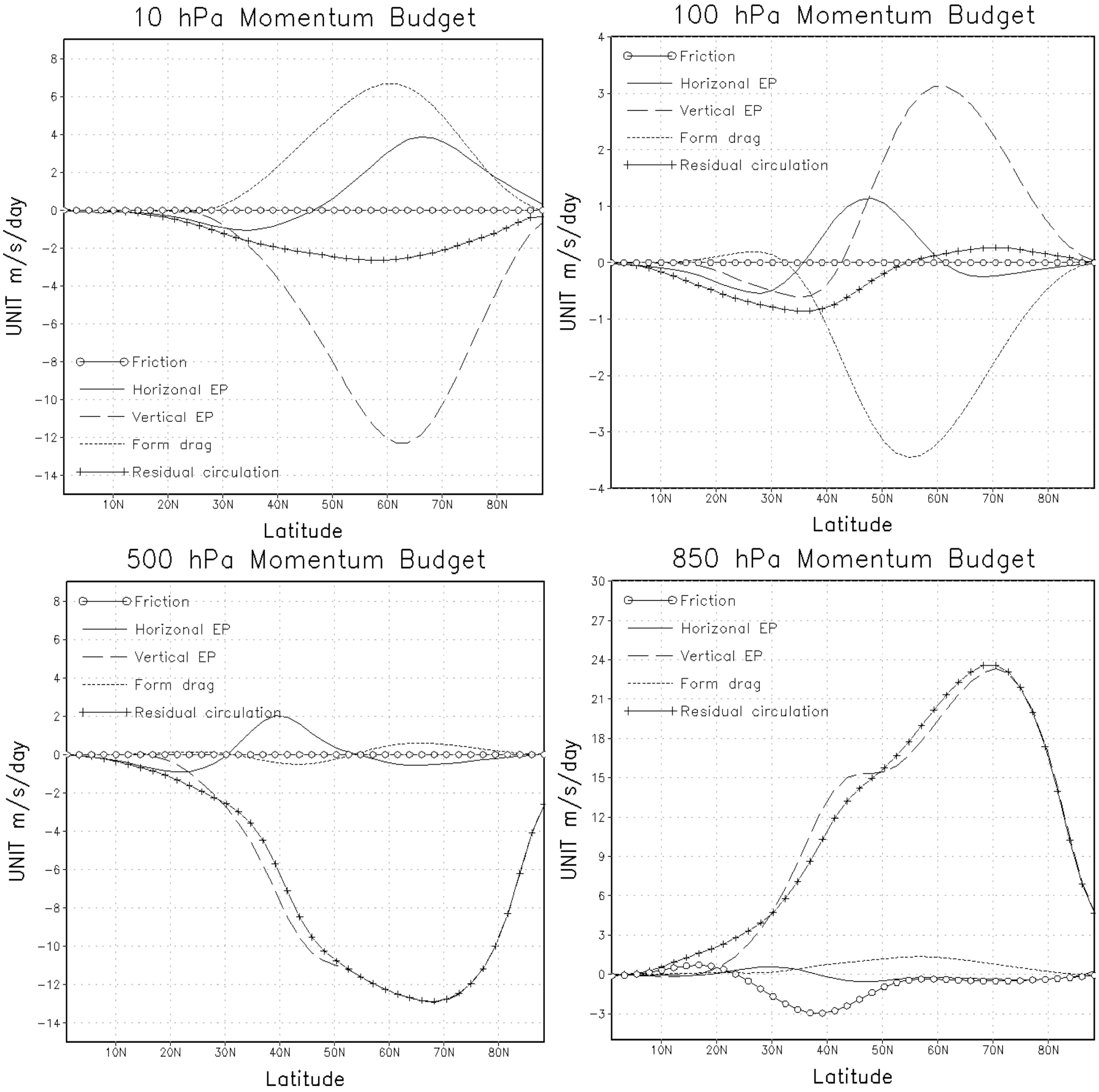

Figure 4.3: Perpetual winter long-term mean momentum budget at 10 hPa, 100 hPa, 500 hPa and 850 hPa. The unit is m s^{-1} day^{-1}. Note that in the long-term mean perpetual run, Horizontal Eliassen-Palm divergence + Vertical Eliassen-Palm divergence + Form drag + Friction ≈ Residual circulation.

In the lower stratosphere, the residual circulation and horizontal Eliassen-Palm flux divergence become relatively small. The positive vertical Eliassen-Palm flux divergence and negative form drag cancel each other. In the troposphere, the horizontal Eliassen-Palm flux divergence and form drag become negligible. Almost all of the residual circulation is balanced by the vertical Eliassen-Palm flux divergence except near the surface where some negative friction is visible in the mid-latitudes.

The winter momentum budget in Fig. 4.3 characterizes the balance among the residual circulation, waves, and friction, in which the zonal wind tendency can be neglected. In the seasonal transition, however, this term has to be considered and will be discussed next.

4.3.2 Final warming

In a similar way to the perpetual winter, we diagnose the residual circulation, Eliassen-Palm flux divergence and friction for the final warming. Unlike the perpetual winter, however, the zonal wind tendency cannot be neglected in the final warming. There are two ways to calculate it, either directly from the daily zonal wind output, or indirectly from other terms in the momentum equation. Here we use both methods to compute the climatological and composite zonal wind tendency for 80-member final warming ensembles.

Fig. 4.4 shows the anomalous zonal wind tendency averaged over days -5/0 calculated separately from the daily zonal wind output and from the momentum equation. The high-latitude deceleration is very clear in both of them, except in the upper stratosphere. Overall, there is a good agreement between them in the lower stratosphere and troposphere. There are more small-scale structures in the zonal wind tendency obtained from momentum budget than from daily output. This is reasonable since the tendency from the daily output is a small residual from the sum of several large terms.

Next we focus on the momentum budget and investigate which terms are responsible for the deceleration. Similar to Fig. 4.3, the composite residual circulation, Eliassen-Palm flux divergence and friction anomalies averaged over days -5/0 are shown in Fig. 4.5. The friction is found to be negligible, even near the surface. In the high-latitudes of the stratosphere,

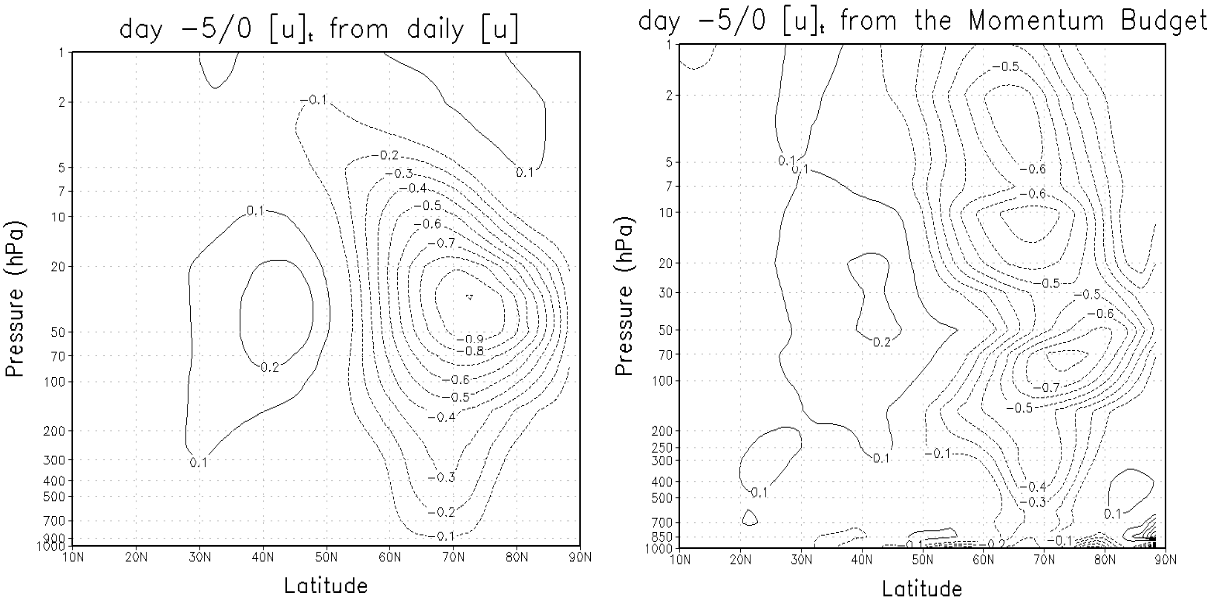

(a) (b)

Figure 4.4: Zonal wind tendency averaged over -5/0 with respect to the final warming onset calculated from (a) daily zonal wind output; (b) momentum budget. The contour interval is 0.1 m s^{-1} day^{-1}.

most of the deceleration is caused by the Eliassen-Palm flux convergence, partly cancelled by the residual circulation. In the upper troposphere, the Eliassen-Palm flux convergence has nearly the same magnitude as the residual circulation. The difference around 70°N is the source of the tropospheric deceleration. The Eliassen-Palm flux divergence and residual circulation are similar in the upper troposphere, but both are positive. Their difference also causes the deceleration in the high-latitudes of the lower troposphere.

The momentum budget for the final warming gives a good estimate of the roles of residual circulation, waves and friction. In the stratosphere, the deceleration is mainly due to the Eliassen-Palm flux convergence, partly cancelled by the residual circulation. In the troposphere, the waves are still important and have almost the same magnitude as the residual circulation. Since there are both wave and circulation anomalies in the troposphere, it is hard to distinguish which mechanism dominates the downward influence. In fact, the waves themselves can induce the residual circulation. Thus from the budget analysis, it is impossible to clearly see whether waves or the changes in the residual circulation occur in response to the stratospheric transition. Nevertheless, the wave activity in the troposphere suggests

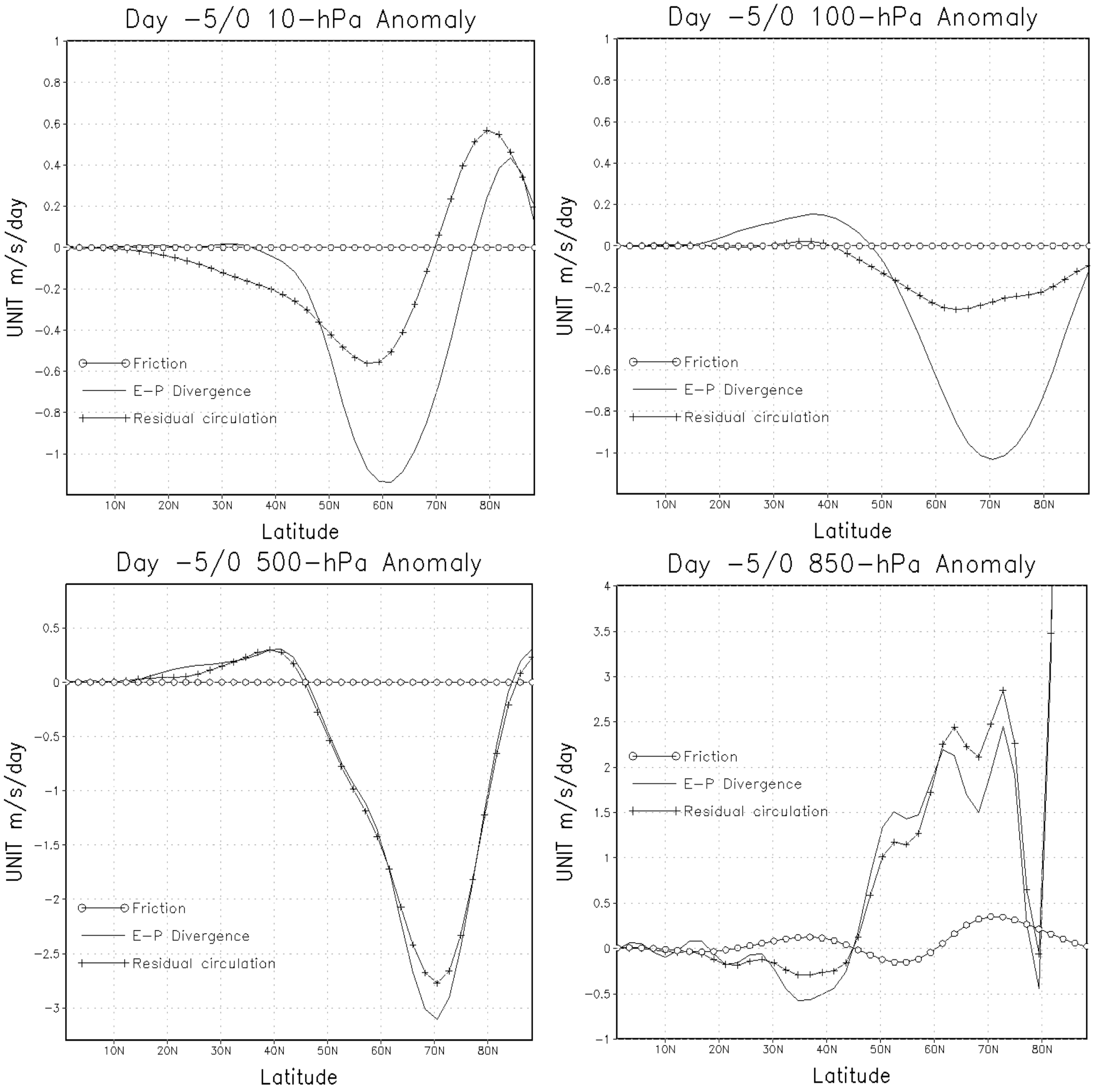

Figure 4.5: Anomalous residual circulation, Eliassen-Palm divergence and friction averaged over day -5/0 with respect to the final warming onset at 10 hPa, 100 hPa, 500 hPa and 850 hPa pressure levels. The unit is m s^{-1} day^{-1}.

that planetary waves are important in the downward influence of the final warmings.

4.4 Zonally symmetric model

In section 4.3, prior to the final warming both anomalous wave activity and anomalous residual circulation are found in the troposphere. They partly cancel each other and result in the tropospheric zonal wind deceleration. It is still not clear what is the source of the tropospehric residual circulation. Is it induced by the stratospheric or by tropospheric wave driving? The former implies the downward control mechanism, while the latter is about the stratospheric influence on the tropospehric planetary waves.

We can use the zonally symmetric model to answer this question. The zonally symmetric model computes its own residual circulation, in response to the wave driving. Thus, it can be used to evaluate the influence of the stratospheric wave driving on the circulation (e.g. Plumb and Eluszkiewicz (1999); Thompson et al. (2006)). In this section, we first describe the zonally symmetric model and perpetual run results, then separate the wave forcing by wave numbers and altitudes (troposphere and stratosphere), in order to understand their different influence on the tropospheric circulation. From these experiments, the mechanism of the downward influence of the final warming will become clear.

4.4.1 Model description

The zonally symmetric model uses the same radiative forcing and dissipations as the full model, but only the zonal mean part (wave number 0) is integrated forward in time. In the zonally symmetric model, the eddy forcings are not internally generated. They must be imposed, and are normally calculated from the results of the full model. There is no topography in the zonally symmetric model. The momentum, thermodynamic and surface pressure equations are:

$$\overline{P_s}\frac{\partial\overline{u}}{\partial t} + (\overline{P_s}\overline{v} - f)(\frac{1}{a\cos\phi}\frac{\partial(\overline{u}\cos\phi)}{\partial\phi}) + (\overline{P_s}\,\overline{\dot{\sigma}}_{new})(\frac{\partial\overline{u}}{\partial\sigma}) = \overline{P_s}F_u$$

$$\overline{P_s}\frac{\partial\overline{T}}{\partial t} + \frac{\overline{P_s}\,\overline{v}}{a}\,\frac{\partial\overline{T}}{\partial\phi} + \overline{P_s}\,\bar{\dot{\sigma}}_{new}\,\frac{\partial\overline{T}}{\partial\sigma} - \kappa\,\overline{P_s}\,\overline{T}\,(\frac{\bar{\dot{\sigma}}_{new}}{\sigma} + \bar{\tilde{v}}\,\frac{\partial\overline{\ln(P_s)}}{\partial y} - \overline{\tilde{D}}) = \overline{P_s}\,F_T$$

$$\frac{\partial\overline{\ln(P_s)}}{\partial t} + \frac{\bar{\tilde{v}}}{a}\,\frac{\partial\overline{\ln(P_s)}}{\partial\phi} + \overline{\tilde{D}} = F_{\ln P_s}$$

where F_u, F_T and $F_{\ln P_S}$ are eddy forcings diagnosed from the full model. Since the eddy forcing F_v has much less effect on the zonal winds, in convenience, it is neglected. A detailed deduction of the eddy forcings is given in the appendix B.

4.4.2 Perpetual run

We first run zonally symmetric model using the same fixed T_{eq} as Fig. 2.1 for the h_0=2000-m topography. Fig. 4.6 and Fig. 4.7 show the 2000-day averaged F_u, F_T and $F_{\ln Ps}$ eddy forcings for the perpetual run. F_u and F_T are the eddy momentum and heat flux divergence. In the mid-summer, since most of the waves are trapped in the troposphere, these terms should be negligible in the stratosphere. This is confirmed in Fig. 4.6; Both F_u and F_T are near zero in the Southern Hemisphere stratosphere. In the Northern Hemisphere stratosphere, the magnitudes of F_u and F_T are both much larger than in the troposphere. In the troposphere most of the eddy maxima are around the jet in mid-latitude. $F_{\ln Ps}$ indicates the difference between full model and zonally symmetric model in the advection of $\ln Ps$.

Fig. 4.6 and Fig. 4.7 show the asymmetry in eddy forcing between the two hemispheres, not only in the stratosphere due to the different seasons, but also in the high-latitudes troposphere, even though T_{eq} is symmetric across the equator. This reflects the different propagation of waves in the two hemispheres. In the Northern Hemisphere, the topography induces strong planetary wave number 1 and causes the eddy forcing in the high-latitudes to be different. In addition, the planetary waves propagate upward into the stratosphere in the Northern Hemisphere, while in the Southern Hemisphere they are trapped in the troposphere. This also causes difference in the tropospheric eddy forcing.

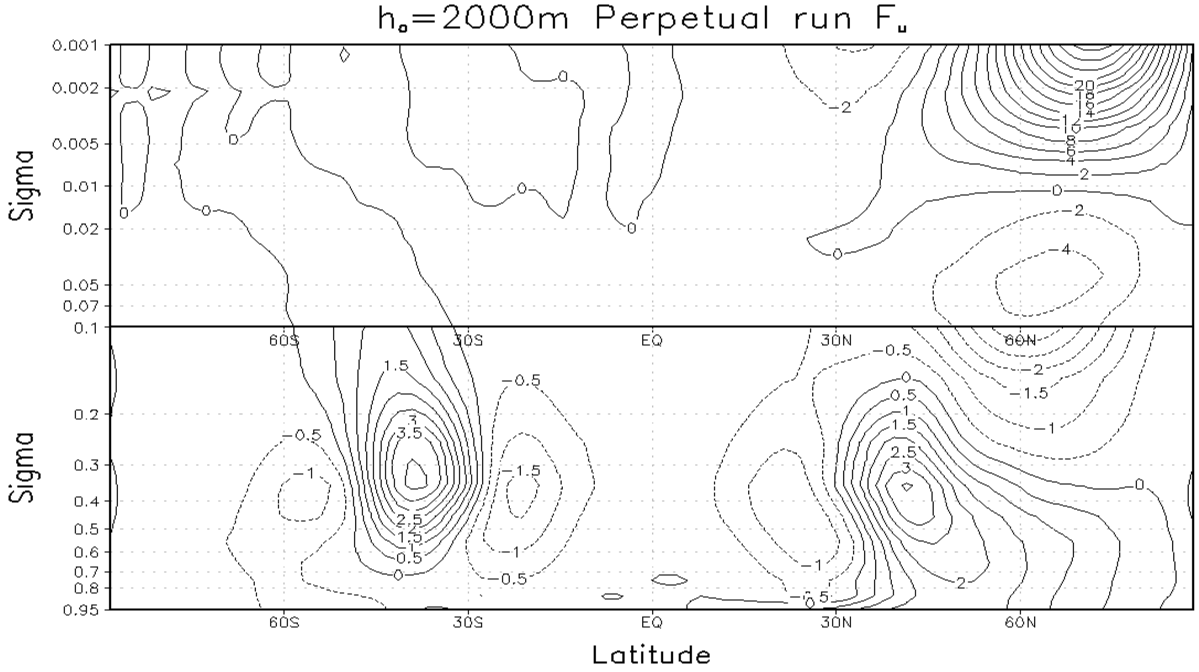

(a)

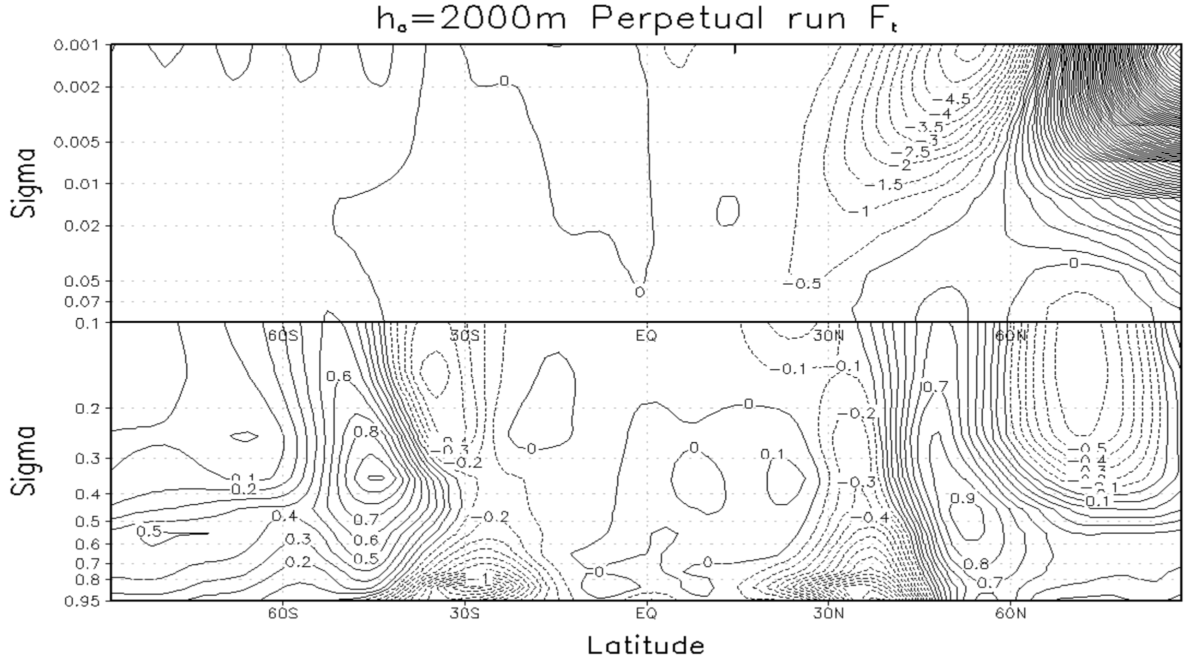

(b)

Figure 4.6: Perpetual run 2000-day averaged eddy forcing F_u and F_T. The unit of F_u is m s^{-1} day^{-1}, the unit of F_T is K day^{-1}. The contour interval in (a) is 2 m s^{-1} day^{-1} above 0.1 σ level, 0.5 m s^{-1} day^{-1} below it. The contour interval in (b) is 0.5 K day^{-1} above 0.1 σ level, 0.1 K day^{-1} below it.

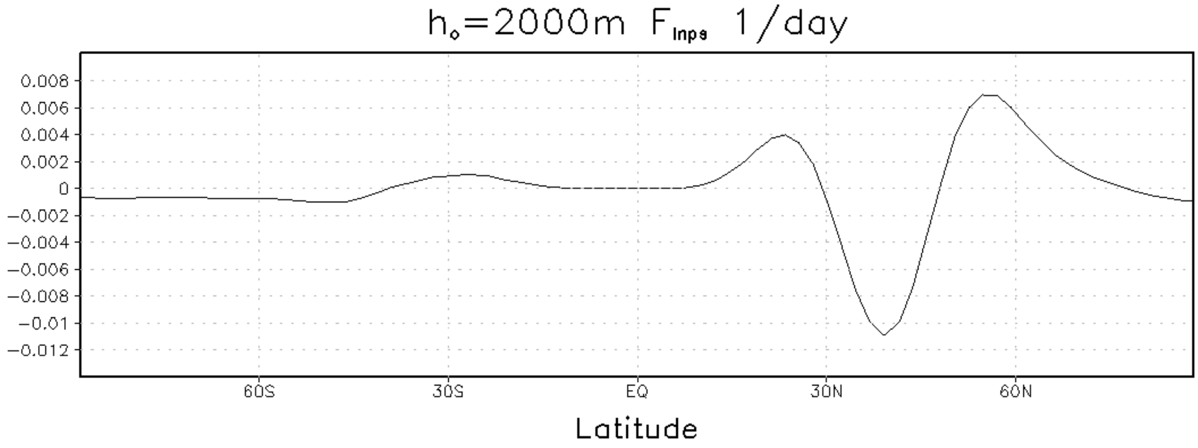

Figure 4.7: Perpetual run 2000-day averaged eddy forcing $F_{\ln Ps}$. The unit is day^{-1}.

In the perpetual run, the zonal winds are stable after a few hundred days. The zonal winds with total eddy forcings in Fig. 4.6 and Fig. 4.7 are shown in Fig. 4.8 (b). In contrast, zonal winds without any eddy forcing are also given in Fig. 4.8 (a). Without eddies, the tropospheric jet is unrealistic. In the stratosphere, the zonal wind vertical derivative $(\frac{\partial u}{\partial z})$ follows the thermal wind relation and is similar to the radiative equilibrium. Due to the effect of the tropospheric boundary condition, the stratospheric zonal wind in the Northern Hemisphere is similar to the radiative zonal wind in Fig. 2.1 while it is not in the Southern Hemisphere. With all the eddies, the zonal wind in the zonally symmetric model closely resembles the long-term zonal wind in Fig. 2.3 (d). In the Southern Hemisphere, the zero wind line altitude is significantly lower. The perpetual run of the zonally symmetric model provides a benchmark for the seasonal and final warming runs. These results show that by adding the eddy forcings to the zonally symmetric model the full response of the zonal wind can be obtained.

4.4.3 Final warming run

A seasonal run is carried out in the zonally symmetric model, using the 365-day climatological seasonal eddy forcings from the 80-member ensembles of the full model. The evolutions also resemble the climatology of the full model. The final warming run is then considered, but for only one composite and for climatological cases are, instead of the full 80-member

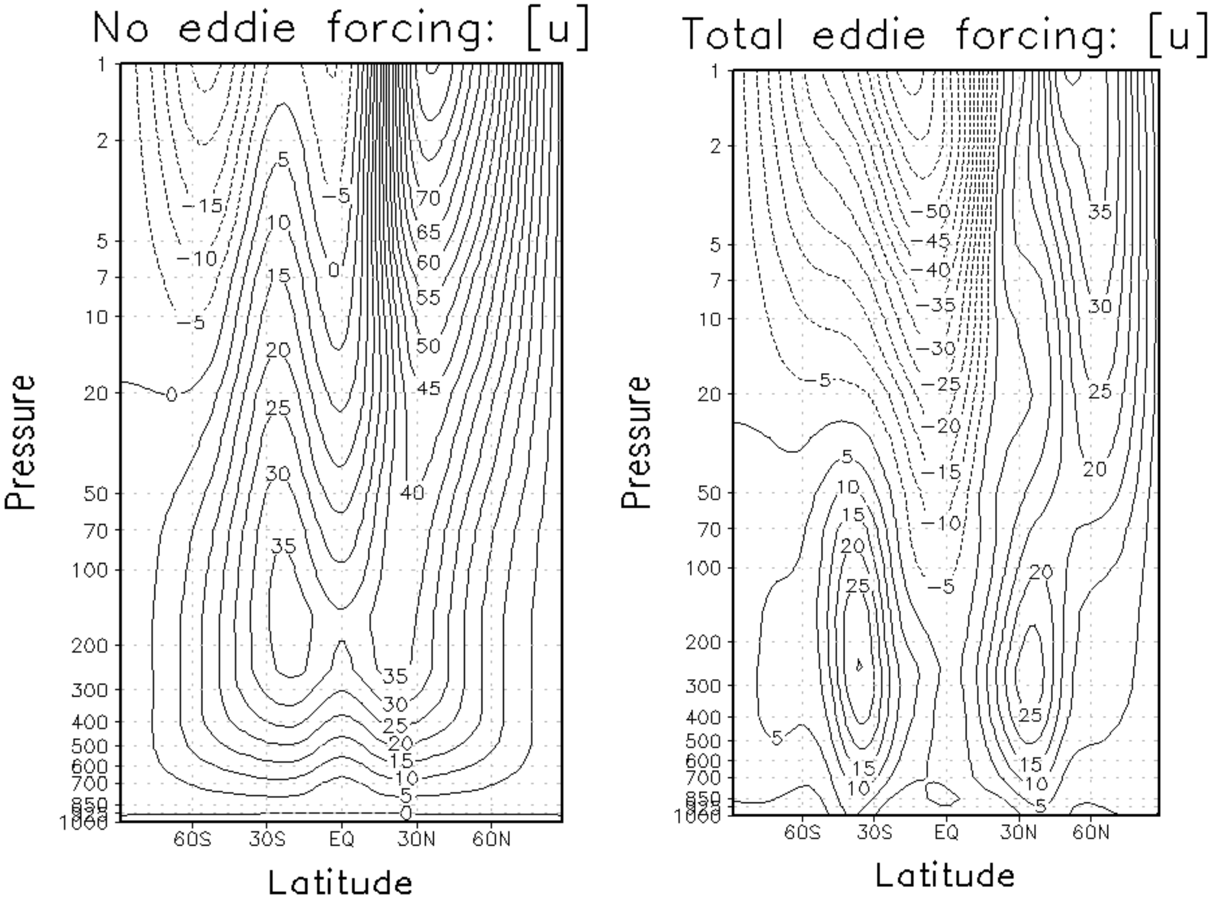

(a)

(b)

Figure 4.8: Zonal wind structures in the zonally symmetric model with (a) no eddy forcing, (b) total eddy forcings calculated from the h_0=2000-m perpetual run in Fig. 4.6 and 4.7. The contour interval is 5 m s^{-1}.

ensembles. The initial conditions and eddy forcings come from the ensemble-mean composite and climatology. Each run starts at day -40 with respect to the final warming onset and ends at day +40.

Fig. 4.9 (a) shows the composite zonal-wind anomaly, obtained by subtracting the climatology from the composite. With the full eddy forcings, the evolution is very similar to the full model results in Fig. 3.17. Next the eddy forcings are divided into long waves (number 1-3) and short waves. We rerun the composite and climatology with the same initial conditions as for the full eddy run. The results for the long and short wave forcings are shown in Fig. 4.9 (b) (c). The evolution with only long waves is almost the same as with all the eddies, and the full tropospheric response is obtained. The evolution with only short waves, however, is characterized by a weakening of the anomalous zonal wind in the stratosphere, which comes from the initial difference between the composite and climatology at day -40 with respect to the onset of the final warming. No tropospheric signal is found in the short-wave final warming run. This confirms the result, from section 4.2, that downward influence of the final warming in our model is only associated with the long waves only, and synoptic-eddy feedback is not important.

We then separate the stratospheric forcing from the tropospheric forcing at approximately 100 hPa. The results for the anomalous zonal wind are shown in Fig. 4.10. In the stratosphere, the evolution with stratospheric forcing is similar to the results with the full forcing, shown in Fig. 4.9 (a). Anomalous zonal winds appear in the upper troposphere, but not in the lower troposphere. This indicates that the stratospheric wave forcing can impact the tropospheric circulation by inducing the residual circulation, as in the theory of downward control. The fact that most of the influence is confined to the upper troposphere, however, suggests this mechanism is not sufficient to explain the full tropospheric response.

Looking at the evolution of the anomalous zonal wind with tropospheric forcing, Fig. 4.10 (b), we see negative anomalies near the onset of the final warming. This implies that the tropospehric residual circulation anomalies discussed in section 4.3 are mostly induced by tropospheric planetary waves. It is the tropospheric planetary waves that respond to the

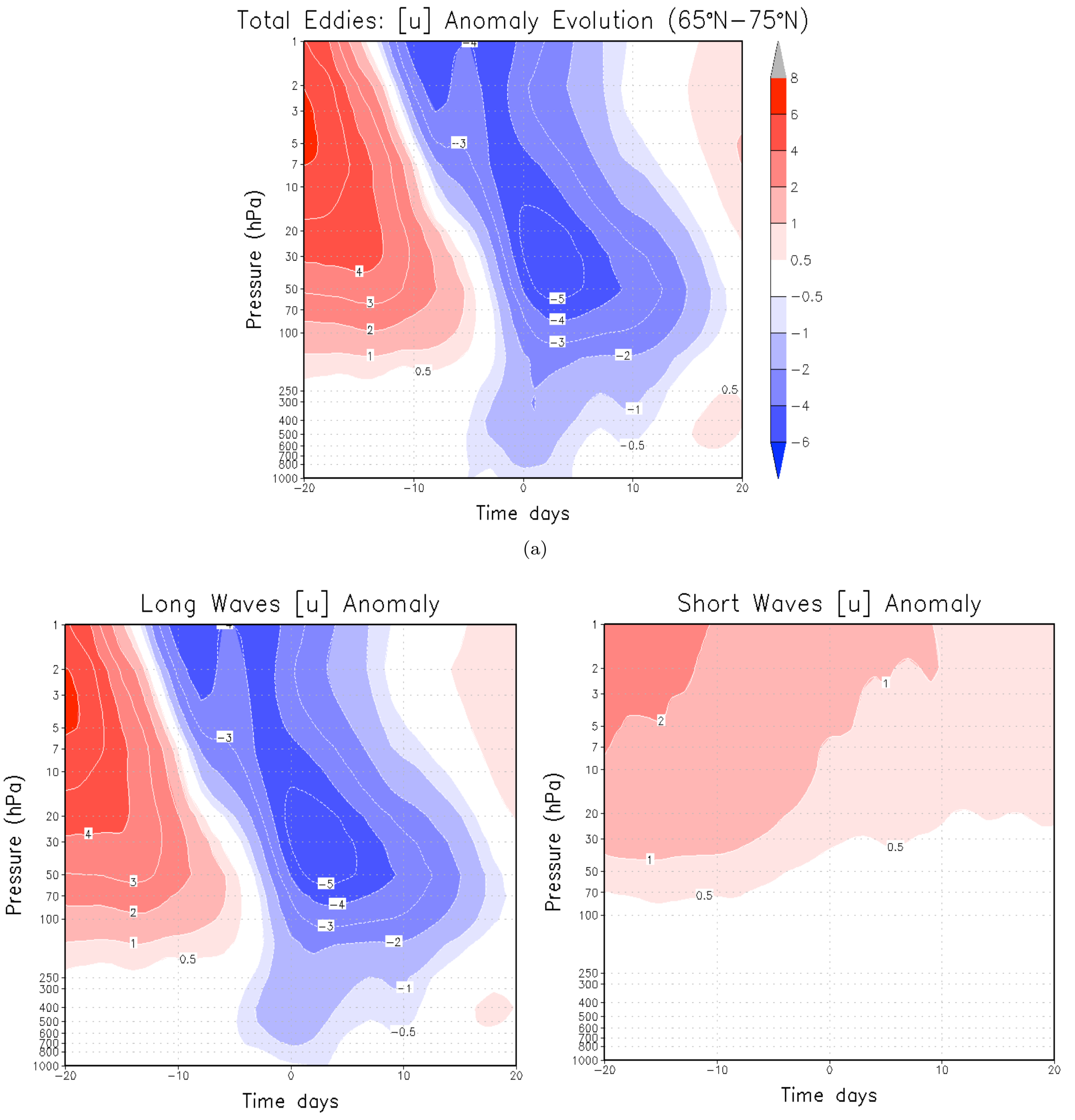

(a)

(b)

(c)

Figure 4.9: Time evolution of anomalous zonal wind across the final warming in the zonally symmetric model with the forcings of (a) total eddies, (b) long waves, (c) short waves. All of the eddy forcings are calculated from the 80-member ensembles h_0=2000-m seasonal run.

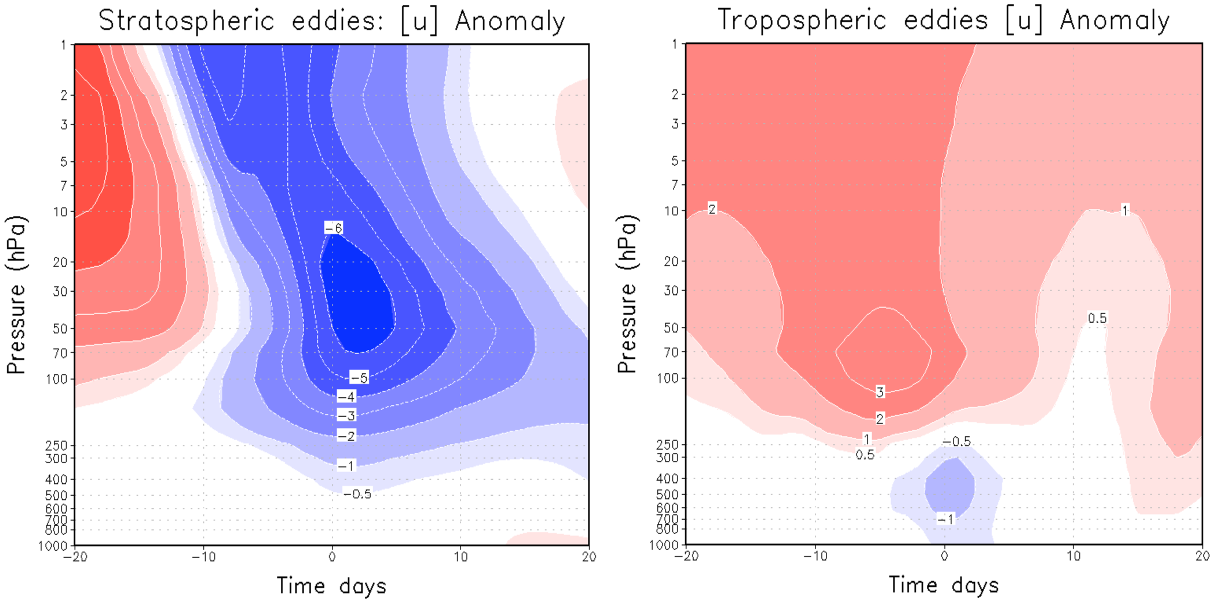

(a)

(b)

Figure 4.10: Time evolution of anomalous zonal wind across the final warming in the zonally symmetric model with the forcings of (a) stratospheric eddies, (b) tropospheric eddies. All of the eddy forcings are calculated from the 80-member ensembles of h_0=2000-m seasonal run. The colorbar is the same as Fig. 4.9.

stratospheric influence and cause the tropospheric zonal wind deceleration prior to the final warming.

4.5 Final warming wave evolution

From section 4.4, tropospheric response to the stratospheric influence is connected to the tropospheric planetary waves. Here we investigate two questions: Which wave number is most important? How do tropospheric waves respond when final warming happens? We carry out the final warming run in the zonally symmetric model using only wave-1 forcing. The evolution of the anomalous zonal wind is shown in Fig. 4.11 (a). The similarity to the full model suggests that wave 1 is most important, and the downward influence in our model is related to the propagation of wave number 1.

We then go back to the full model and construct the composite for the wave-1 amplitude. The evolution of the final warming is shown in Fig. 4.11 (b). In the troposphere, a burst of wave-1 amplitude appears, while the stratospheric wave weakens. This wave eruption does

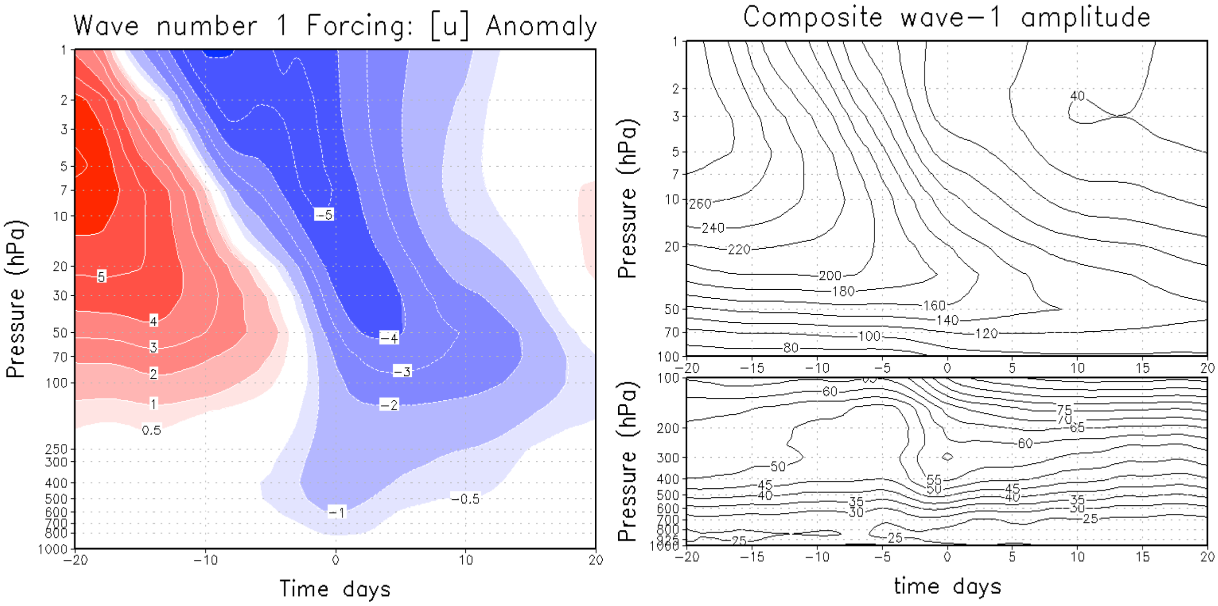

(a) (b)

Figure 4.11: (a) Time evolution of anomalous zonal wind of the final warming in the zonally symmetric model with wave-1 forcing. The forcing is calculated from the 80-member ensembles of h_0=2000-m seasonal run. The colorbar is the same as Fig. 4.9. (b) Time evolution of composite wave-1 amplitude of the final warming in the full model. The contour interval is 5 m below 100 hPa, 20 m above 100 hPa .

not occur in the climatological evolution, suggesting that the amplification of wave number 1 prior to the final warming is the main reason for the tropospheric deceleration.

4.6 Discussion and conclusion

In this chapter, we explore the mechanisms of the downward influence of the final warming on the tropospheric circulation. The comparison between anomalous long waves and full eddy Eliassen-Palm flux divergence in section 4.2 suggests that planetary waves play an important role in causing the stratospheric and tropospheric deceleration prior to the final warming. The zonally symmetric model run with long-wave forcing also confirms that the downward influence of the final warming involves interactions between long waves and the zonal-mean flow in high-latitudes.

Without topography, previous studies indicated that tropospheric synoptic-eddy feedback is primarily responsible for the tropospheric response to the stratospheric wave driving

(Kushner and Polvani, 2004; Song and Robinson, 2004). The planetary waves are also important for communicating the stratospheric influence down into the troposphere, but their response, mostly due to wave number 3 in the model, is much weaker than the synoptic eddies (Song and Robinson, 2004). This differs from our topographic final warming results, in which the planetary waves are much more important so that the synoptic eddy feedback is invisible. This relates to the decorrelation time of the annular model with and without topography. Gerber et al. (2008) suggested the intrinsic time scale of the annular mode is shorter in the presence of topography or some other stationary wave forcing. This implies a weak transient-eddy feedback when the jet is not zonally symmetric. In addition, the responses of Song and Robinson (2004) and Kushner and Polvani (2004) are in steady state simulations, while the final warming is a transient event. As a transient event, the final warming might not allow enough time for the synoptic eddies to respond systematically, so that the mechanism of the tropospheric eddy feedback is much weaker in the presence of topography.

In the stratosphere, the zonal wind deceleration prior to the final warming is mostly determined by the anomalous wave activity, partly cancelled by the residual circulation. In the troposphere, the planetary waves have almost the same magnitude as that due to the residual circulation. Their difference determines the tropospheric zonal wind deceleration. Zonally symmetric model runs reveals that, by inducing the residual circulation, the stratospheric wave driving can affect the tropospheric circulation, but the tropospheric signal is weak and mostly confined to the upper troposphere. Thus, it is the tropospheric planetary waves that induce the tropospheric residual circulation and cause the zonal wind deceleration in the troposphere.

Our investigation indicates that there are two mechanisms for the downward influence for the stratospheric final warming on the tropospheric circulation. The stratospheric anomalous wave driving induces the residual circulation and has an impact on the tropospehric circulation, similar to Haynes et al. (1991) and Thompson et al. (2006). The tropospheric signal due to this mechanism, however, is very weak and mostly confined in the upper troposphere. On the other hand, the stratosphere can affect the propagation of planetary wave from the troposphere, resulting in a wave burst prior to the final warming in the troposphere. This wave eruption can also induce the residual circulation and finally cause the tropospheric zonal wind deceleration. This is similar to the results of Kushner and Polvani (2004) and Song and Robinson (2004), but planetary waves, instead of synoptic eddies are primarily in responsible to the stratospheric changes.

The mechanism of the tropospheric wave-1 amplification associated with the final warming is still not very clear. One possibility is the waves are trapped by the stratosphere when final warming occurs, as suggested by Black and McDaniel (2007a). Wave reflection (Perlwitz and Harnik, 2003) and resonance (Plumb, 2009) are also possible. Further studies are needed in order to understand this phenomenon. A wave-one model with topography might be a good tool to study the propagation during the final warming. Since the planetary waves are not only induced by the topography, but also by wave-wave interaction among higher wave numbers, the latter part of the forcing has to be calculated as a residual in the wave one equation, averaged over time, from the full model and included as forcing in the wave one model. This might give a better simulation of wave number 1 behavior during the final warming.

In summary, the pattern of downward influence in our 2000-m final warming resembles the Northern Hemisphere observations by Black et al. (2006). The diagnose analyses of the downward influence reveals that the tropospheric zonal wind deceleration is mostly attributed to the tropospheric wave-1 amplification prior to the final warming. The residual circulation induced by the stratospheric wave driving, although it can reach the troposphere, is too weak and confined to the upper troposphere. This suggests that the planetary waves are crucial in the observed downward influence of the final warming.

Chapter 5

Predictability of the stratospheric warmings

5.1 Introduction

The stratosphere has received more attention since it is realized that the stratosphere does not respond passively to the troposphere. The annular mode analyses of Baldwin and Dunkerton (2001) suggested that stratosphere could be used to predict tropospheric weather regime. Charlton et al. (2003) showed that using the amplitude of the stratospheric Arctic Oscillation as a predictor in a simple statistical model results in greater skills than using troposphere-only model. The case studies of Kuroda (2008) also suggested that including the role of stratospheric variability is crucial for improving the predictability of medium-range weather forecast in winter. Better predictions of sudden warming, one of the most important events in the stratosphere, will, therefore, lead to better predictions in the troposphere.

The timing of the stratospheric final warming varies from year to year in both hemispheres. The Northern Hemisphere has a larger interannual variability (Waugh and Rong, 2002; Black et al., 2006). Climatologically, the final collapse of the polar vortex occurs at the same time as the annual transition from winter to spring (spring onset) in the lower atmosphere (Black et al., 2006). This interannual variability in the date of the final warming is closely connected to the ozone depletion. Since the break-up of the polar vortex mixes the surrounding air over the pole, a late final warming is associated with reduced ozone concentrations in the polar regions. The timing of the final warming depends strongly on the planetary waves (Waugh et al., 1999). Better understanding of the interannual variability and prediction of the timing of the final warming can lead to improved predictions of ozone recovery in the Southern Hemisphere.

Both the sudden warming and the final warming are associated with anomalous upward Eliassen-Palm flux from the troposphere, in observations (Polvani and Waugh, 2003; Black et al., 2006; Black and McDaniel, 2007b), and in models (Scott and Polvani, 2004; Sun and Robinson, 2009). How the stratosphere is affected by the troposphere and subsequently affect the troposphere is, however, complex. Reichler et al. (2005) studied the response of stratosphere-troposphere system to externally imposed pulses of lower-tropospheric planetary wave activity and found large variability in these responses. The perturbation experiments by Gerber et al. (2009) also revealed two different tropospheric responses following the sudden warming. The variability, in this case, was attributed to the interaction between the tropospheric pulse and tropospheric circulation before the pulse reached the stratosphere, and the sensitivity of the stratospheric wave breaking to the detailed structure of the polar vortex (Reichler et al., 2005). Understanding this process is important for improving predictions of stratospheric warmings and their influence on the tropospheric circulation.

Two different aspects of stratospheric sudden warmings warrant consideration. Conventionally the sudden warming is connected to the anomalous wave propagation from the troposphere, so the predictability of the sudden warming can be traced back to the troposphere. For example, Martius et al. (2009) reported that 25 of their 27 sudden warming events are preceded by blocking events. They suggest that tropospheric blocking is a necessary but not sufficient condition for the occurrence of a sudden warmings. On the other hand, the potential importance of stratospheric internal dynamics is raised by Holton and Mass (1976), and in further explorations of stratospheric vacillation by Yoden (1987); Christiansen (1999, 2000). Using a single-layer quasi-geostrophic model, Mattewman (2009) suggested that the sudden warming can occur even without the tropospheric anomalous planetary wave source. These two views of the sudden warming lead to different deductions regarding the relative roles of troposphere and stratosphere in determining its predictability.

Unlike the sudden warming, the final warming is mainly due to the increase in solar heating as spring progresses. Waves from the troposphere are still important in decelerating the zonal wind and destroying the polar vortex. Black et al. (2006) found that the abrupt zonal wind evolution in the early final warming resembles the sudden warming, while late final warmings are characterized by a slow transition that is more determined by radiative heating. Because of the involvement of diabatic heating, it is even harder to understand the dependence of the predictability of the final warming on the troposphere and stratosphere.

Quantitatively, both the troposphere and stratosphere should play some role in determining the predictability of the stratospheric warmings. In this chapter, using a series of perturbation experiments, we test the relative roles of the troposphere and stratosphere in determining the timing of the stratospheric sudden and final warmings. A common way to accomplish this is to add some perturbations to troposphere (Reichler et al., 2005; Gerber and Polvani, 2009) or to the stratosphere (Song and Robinson, 2004; Kushner and Polvani, 2004) and follow their subsequent influences. Here we separate the stratospheric and tropospheric perturbations and add them to the control run. By comparing their influences on the predictability of the stratospheric warmings, the relative roles of the troposphere and stratosphere in determining the stratospheric warming will be clear, and our third hypothesis, that much of the predictability of stratospheric warming events comes from the troposphere, can be tested.

Following the introduction, section 5.2 describes the method we use for the perturbation experiments. Section 5.3 and 5.4 show the perturbation results for the sudden warming and the final warming. The final section includes the discussion and conclusion.

5.2 Perturbation method

We continue to use h_0=2000-m topographic sudden / final warming events with $u_1 = 280$ m s^{-1} (vortex strength) to carry out the perturbation experiments. The sudden warming onset is defined as the time when zonal mean zonal winds at 10 hPa and 70°N reverse sign. If the interval of two sudden warmings is less than 30 days, we regard the two events as one. Based on this definition, four sudden warmings are found between day 2000 and day 3000 in the perpetual-winter run. We then perform the perturbation experiments for them one by one. For the final warmings, the approach is similar, but we separately consider early, middle and late final warmings, according to their different onset times. Two final-warming cases are randomly selected for each type.

For each sudden / final warming event, there are two control runs starting at day -20 and -10 with respect to the warming onset time. We did some experiments for earlier initial condition, but found that stratospheric warming events lose their predictability when initial conditions are selected from too long before the onset. The ensemble forecast of Gerber and Polvani (2009) also showed that if the tropospheric initial perturbation is launched more than 20 days before the warming, the sudden warming begins to cease to predictable.

In the experiments, the perturbations are added to the initial conditions but other settings are kept the same as in the control run. The equilibrium temperature remains unchanged in the sudden warmings and the seasonal transition in the equilibrium temperature in the final warming is also the same as in the control run for each final warming. The perturbed initial conditions are given by:

$$X_{\mathrm{total}}(t) = (1-a)\,X_{\mathrm{Initial}}(t) + a\,X_{\mathrm{perturb}}(t')$$

where $X_{\mathrm{initial}}(t)$ is the control run initial condition at day -20 and -10, including vorticity, divergence, temperature and surface pressure spectral fields. $X_{\mathrm{perturb}}(t')$ is the perturbation field. It comes from the same warming event but at a different time from the initial condition. The perturbation fields used for day -20 initial conditions are the daily output from day -30 to day -10 while the perturbation fields for day -10 are from day -20 to day 0. Thus for each warming event, we have two control runs with day -20 and day -10 initial conditions. For each initial condition, there are 10 perturbation experiments. The coefficient, a determines the perturbation region. We have three different types of experiments as follows:

1. whole-field perturbation experiments. a=1 so that the perturbation field $X(t')$ completely replaces the original field.

2. stratospheric perturbation experiment:

$$a(\sigma) = \begin{cases} 1 & \sigma \leq 0.1 \\ 0 & \sigma > 0.1 \end{cases}$$

   In this setting, only the stratospheric field is perturbed.

3. tropospheric perturbation experiment:

$$a(\sigma) = \begin{cases} 1 & \sigma \geq 0.1 \\ 0 & \sigma < 0.1 \end{cases}$$

   Similar to 2, but only tropospheric fields are perturbed. The surface pressure perturbation is regarded as the tropospheric field.

Each perturbation run ends at day +40 with respect to the warming events. In the perturbation runs, the time step is reduced to 4.8 minutes to prevent numerical instability during the initial adjustment to the perturbed initial condition. The schematic design of the perturbation experiments is shown in Fig. 5.1.

We calculate the timing of the warming onset for each perturbation experiment. It is expected that the timing should be, at least partly, dependent on the perturbed initial conditions. Specifically, the longer the perturbation initial condition is from the warming onset, the later the warming onset will occur in the perturbation run. If the warming is independent of the initial condition, the timing of the warming event will be similar to that in the control run, no matter how the initial condition is perturbed. In this way, the effects of total perturbation, stratospheric and tropospheric perturbations on the timing of the sudden / final warmings can be observed and our third hypothesis can be tested.

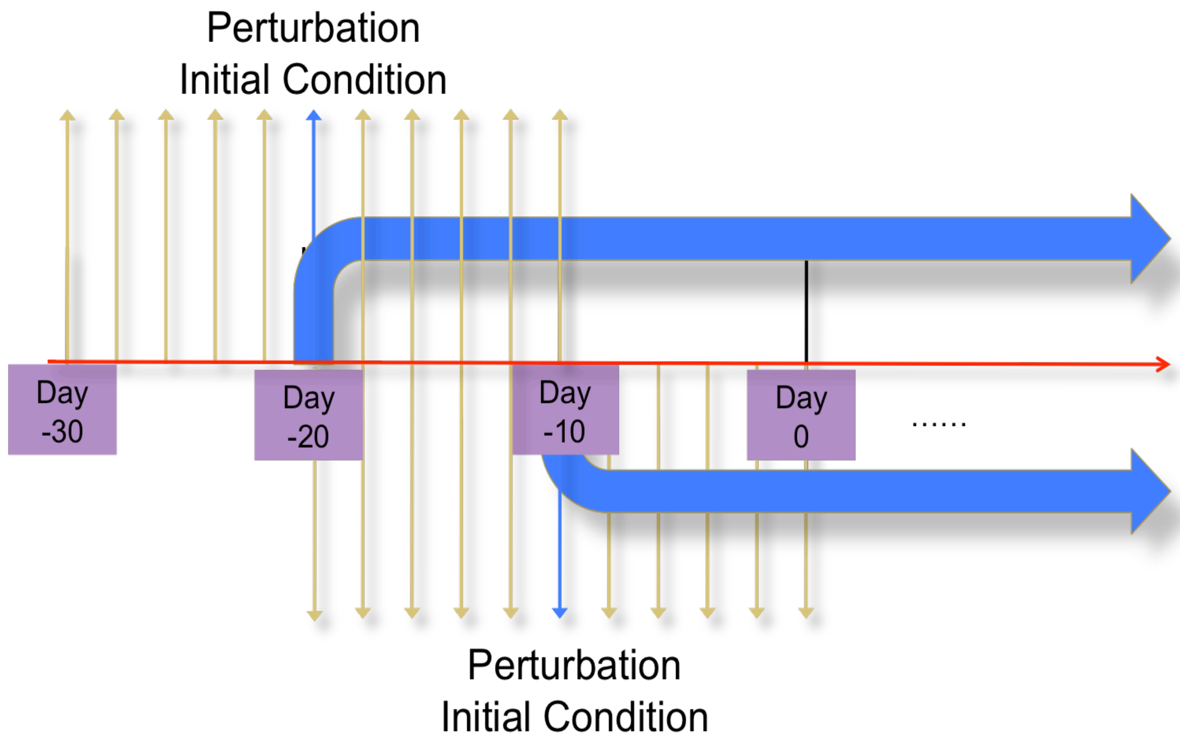

Figure 5.1: The schematic design of the perturbation experiment for the h_0=2000-m sudden / final warming events. For each warming event, there are two control runs with the different initial conditions at day -20 and -10. The perturbation fields come from other days around the control run initial condition. All perturbation runs end at day +40. See text for details.

5.3 Sudden warming perturbation experiments

We follow the method in described in section 5.2 to carry out the perturbation experiments for the sudden warmings. Fig. 5.2 shows the time evolutions of zonal winds at 70°N for the four sudden warmings. The first sudden warming is a deep one, in which the zonal winds transit to -20 m s^{-1} quickly and zero wind line descends down to around 50 hPa. If we only consider the first deceleration stage in the second sudden warming, it is the shallow one. The magnitude of the negative zonal wind is small and the zonal wind recovers quickly. The rest two sudden warmings are also shallow. Overall, few sudden warmings in our model extend down into the lower stratosphere.

The timing of the sudden warming, for the four sudden warming events, are shown in Fig. 5.3. With different types of perturbations, the onset time of the sudden warming varies greatly. The timing of the sudden warming follows the perturbation field well for both day -20 and -10 initial runs. The slopes for both initial conditions are -1. This indicates that the timing of the sudden warming is very sensitive to the initial condition, as expected, as there are no changes to the background state during the perpetual-winter runs, from which these events are taken.

We then separate the perturbations into stratospheric and tropospheric components, and carry out the experiments for each component. We find that the occurrence of the sudden warming is sensitive to the choice of perturbations. Following some stratospheric and tropospheric perturbations, no sudden warmings occurs, especially for the shallow sudden warming events. Although sudden warmings do not always occur, some features are still evident. For the stratospheric perturbation, the slope for the day -20 initial condition is around 0, suggesting that the predictability of the sudden warming is independent of the perturbation at that time. The slope of day -10 initial condition, however, is around -1 within 10 days of the onset time. This tells us that the near the onset of the sudden warming the stratosphere is more effective in determining its predictability.

Results from the tropospheric perturbations experiments are nearly opposite to those

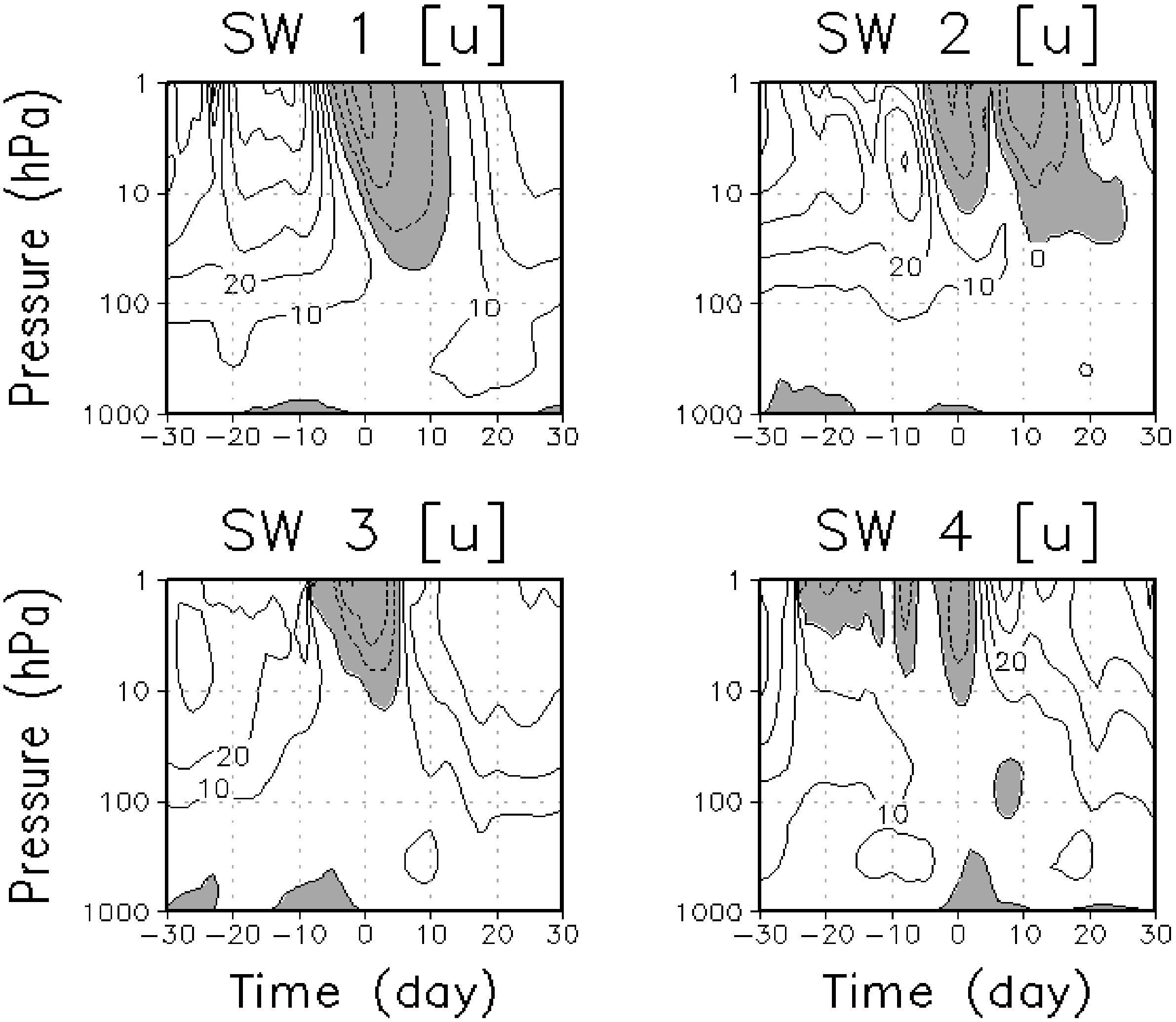

Figure 5.2: Time evolution of the zonal mean zonal wind at 70°N for the four sudden warming events with respect to the onset time. The onset dates for the four sudden warming events are day +2319, day +2449, day +2697, day +2779. The contour interval is 10 m s^{-1}. Negative zonal winds are shaded.

from the stratospheric experiments. Near the onset of the sudden warming, the slope is quite horizontal, while more resemble the total perturbation results when the perturbation time is 10 days or more from the onset time. This is clearer for the deep sudden warmings. For the shallow ones, it is hard to see any pattern due to the scarceness of the sudden warming points (sudden warming does not occur).

In order to test the robustness of our results, another four experiments are carried out, but for sudden warmings with reduced vortex strength (u_1=200 m s^{-1}). Under this setting, 20 sudden warmings can be found within the 2000-day perpetual run. The frequency of the occurrence of sudden warming is around 10 events per thousand days, much greater than for the strong vortex strength setting (4 events per thousand days). The four cases we select for the experiments are deep sudden warmings, as shown in Fig. 5.4. These events all extend downward into lower stratosphere. We then follow the same method for the perturbation experiments and show the results in Fig. 5.5.

The total perturbation experiments are still the same. Unlike the previous cases, the sudden warmings occur in most of the experiments so that it is easier to see the slopes. Overall, the pattern in Fig. 5.5 is similar to Fig. 5.3, with clearer slopes. For the day -20 initial condition, the slope of the stratospheric experiments is nearly 0, while close to -1 for the tropospheric ones. This implies that the troposphere is more effective than the stratosphere in determining the predictability of the sudden warming at this time. The slopes for the day -10 initial conditions are complex. There is a boundary day between stratospheric and tropospheric controlled predictability. Prior to this boundary day preceding the sudden warming, the troposphere primarily determines the sudden warming predictability. After this day, the stratosphere is more effective. The days for first, second and fourth sudden warmings are day -11, -6 and -16, respectively. The results for the third sudden warming are a little different from the other three. The troposphere is predominant more than 9 days before the sudden warming. At less than 9 days, however, the stratosphere is still ineffective. By looking at the zonal wind evolution, we did see that zonal wind decelerates in the stratospheric perturbation experiments, but insufficiently for the zonal wind to reverse

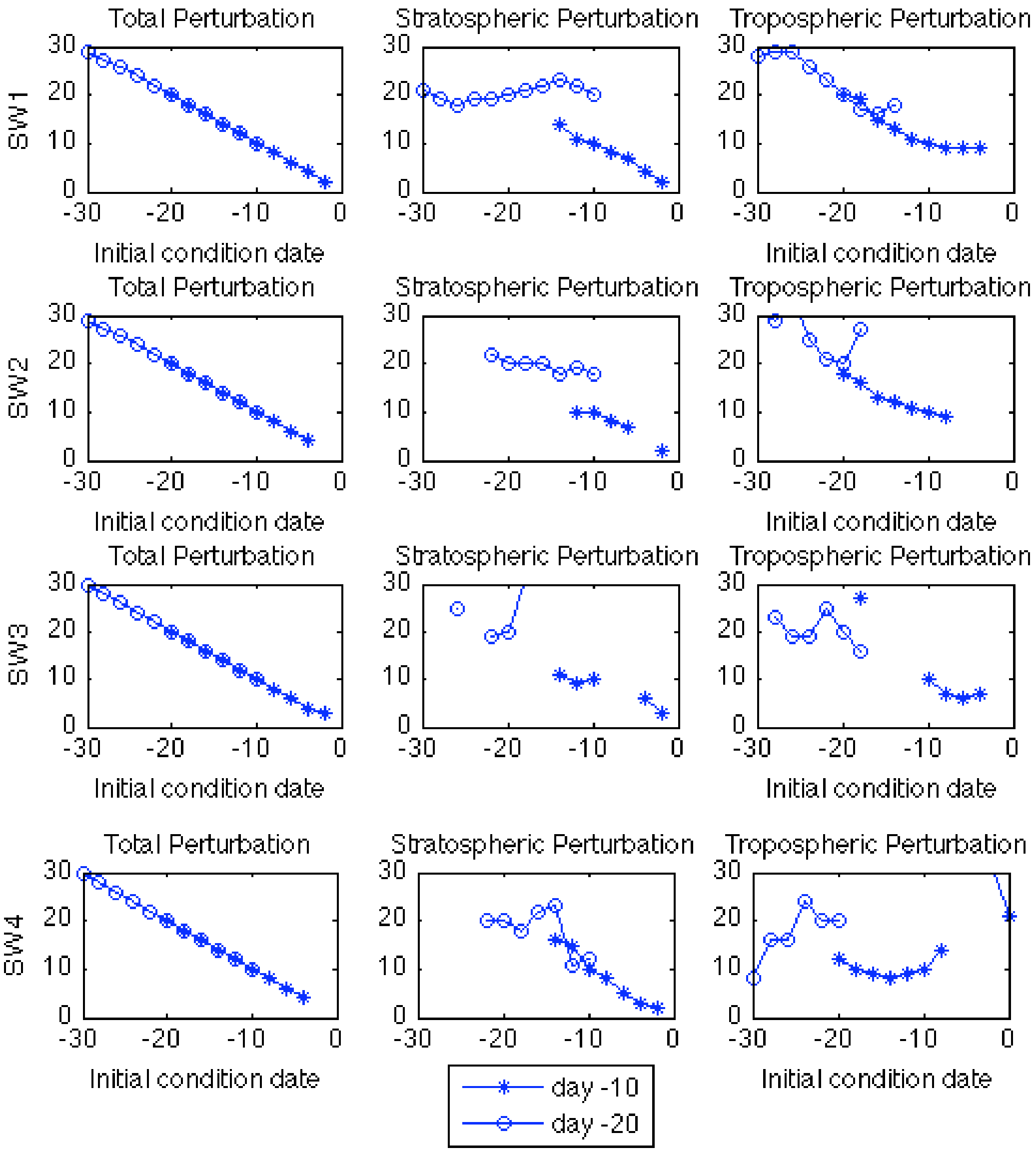

Figure 5.3: Perturbation experiments for the four sudden warming events shown in Fig. 5.2. For each sudden warming events, there are two control runs with day -20 and -10 initial conditions. The xaxis is the time of the perturbation field with respect to the onset time. The yaxis tells how many days after the initial condition sudden warming occurs.

in sign.

In short summary, the sudden warming experiments imply there is a boundary day, which separates the sudden warming predictability by the stratosphere from its predictability by the troposphere. This boundary day is around day -10 with respect to the onset of the sudden warming, but it is variable among different warming events.

5.4 Final warming perturbation experiments

5.4.1 Early and late final warming evolutions

Similar to the observations in the Northern Hemisphere, the timing of our simulated final warmings has large interannual variability (a standard deviation of 19 days). For different timing of the final warmings, the evolutions of the zonal wind and the relative roles of diabatic heating and planetary waves are also different. Following Black et al. (2006), we separate the final warmings into early and late types based on the mean onset time at day +101 of the seasonal transition. This yields 41 early and 39 late final warming events. The time evolution for each type is shown in Fig. 5.6. The main differences between early and late final warmings are in the stratosphere: the zonal wind transition in the early final warming is more abrupt with a stronger relaxation toward the initial state after the onset of the warming. Given that wave-1 amplitude peaks in the mid-winter and weakens toward the spring, it is expected that early final warmings are controlled more by planetary waves than late warmings, so their transitions are more abrupt.

5.4.2 Perturbation experiments

We then select 2 early (day +58, +74), 2 middle (day +99, +99) and 2 late (day +133, +149) final warming events for the perturbation experiments. The results for all of the three perturbations are shown in Fig. 5.7. The slope of the linear regression in the total perturbation experiments is -0.945, very close to -1. This indicates that the timing of the final warmings closely depends on the initial condition. Since the equilibrium temperature

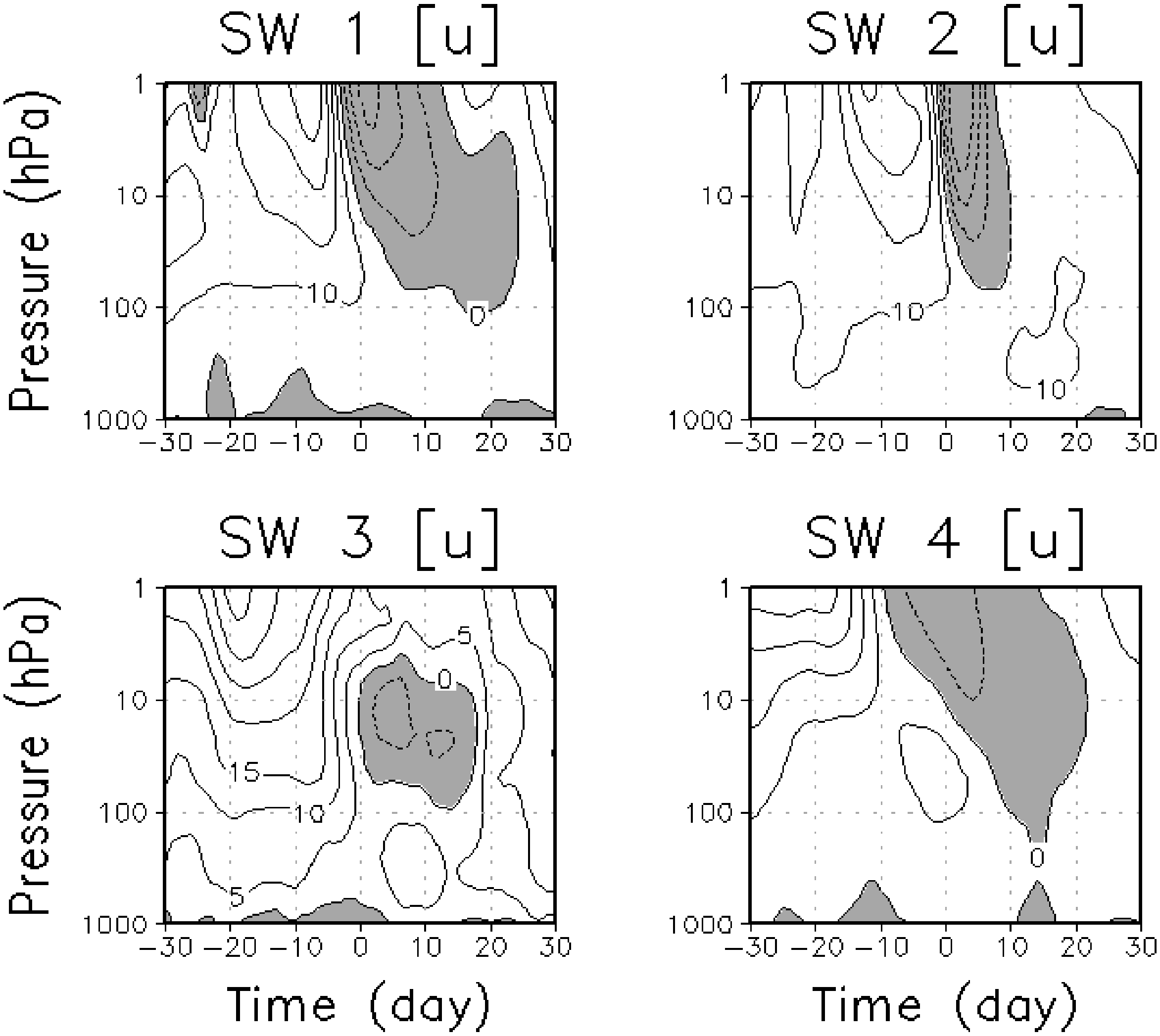

Figure 5.4: Time evolution of the zonal mean zonal wind 70°N for the four sudden warming events with reduced vortex strength (u_1=200 m s^{-1}). The onset dates for the four sudden warming events are day +2182, day +2460, day +2845, day +3710. The contour interval is 10 m s^{-1}. Negative zonal winds are shaded.

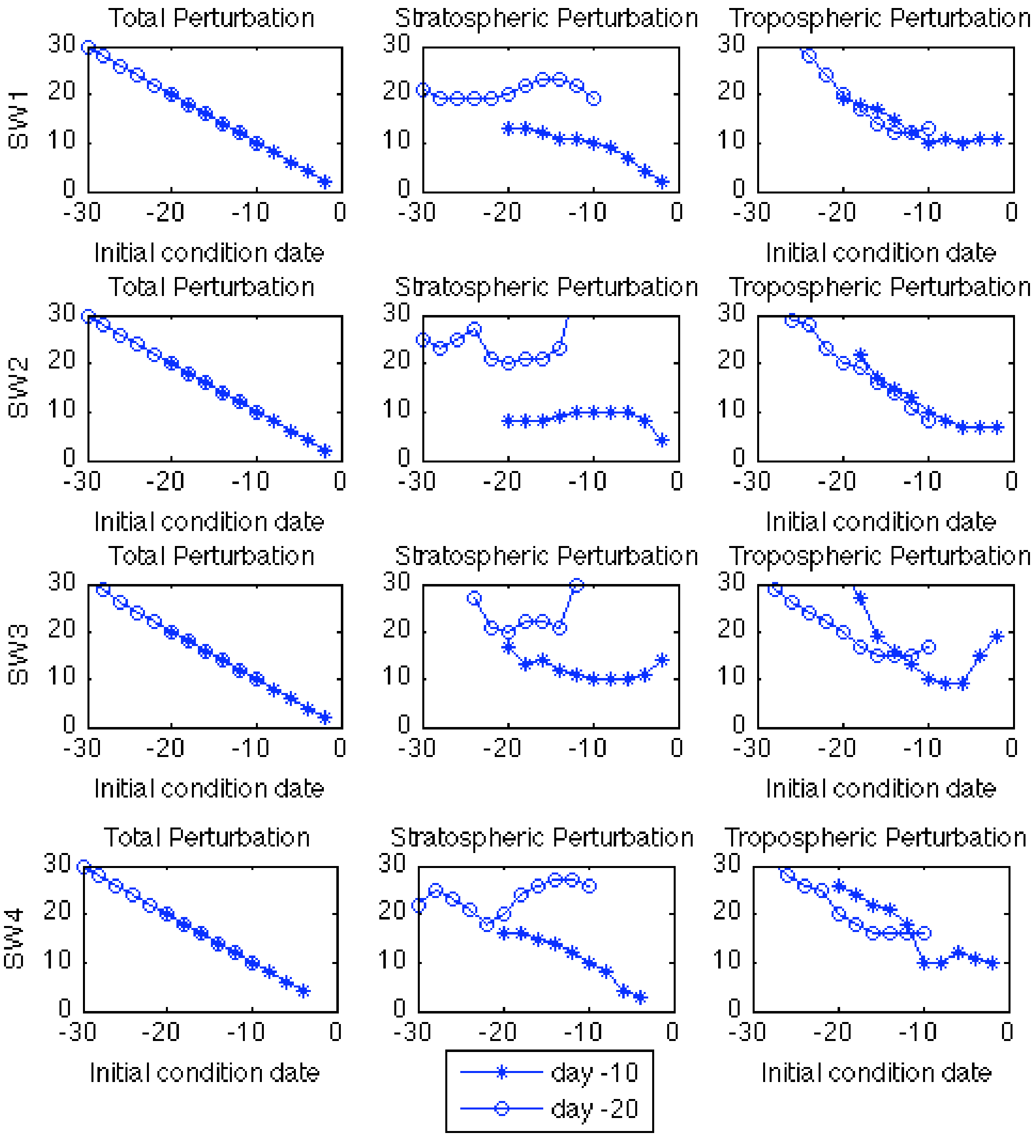

Figure 5.5: Perturbation experiments for the four weak vortex strength (u_1=200 m s^{-1}) sudden warming events shown in Fig. 5.4. For each sudden warming events, there are two control runs with day -20 and -10 initial conditions. The xaxis is the time of the perturbation field with respect to the onset time. The yaxis tells how many days after the initial condition sudden warming occurs.

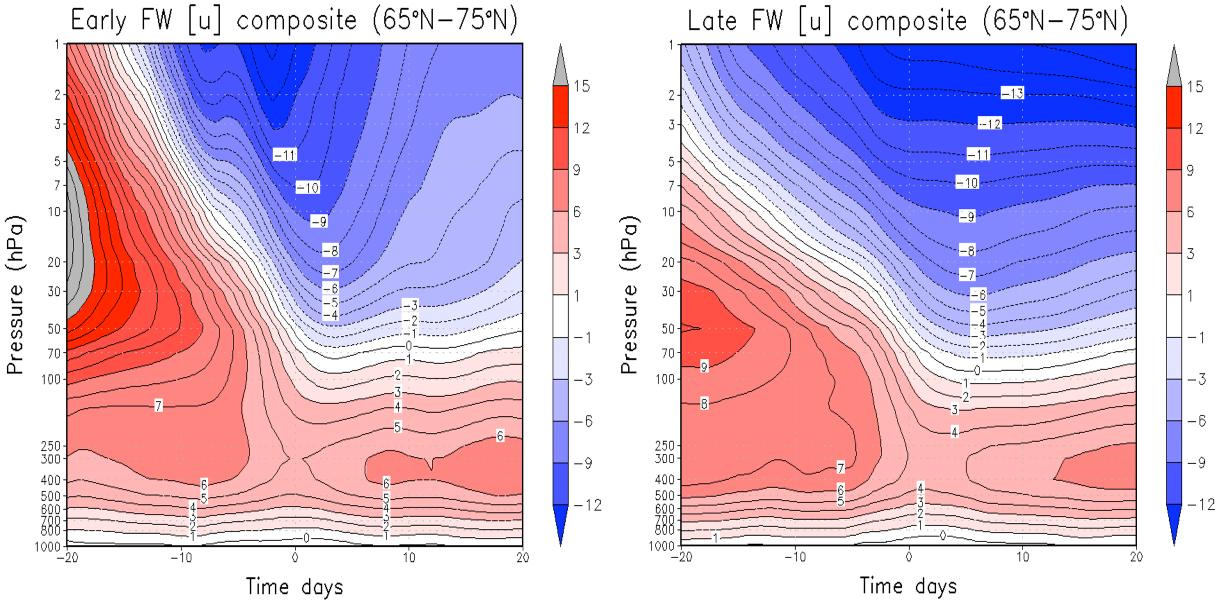

(a) (b)

Figure 5.6: Time evolution of zonal wind averaged over 65°N - 75°N for the (a) early and (b) late final warmings. The early and late final warmings are separated by the mean onset date day +101. There are 41 early and 39 late final warming events.

transition is the same in the perturbation experiments as in the control run, the fact that the onset time depends on the perturbation field implies that radiation has less impact on the timing of the final warming. The stratospheric and tropospheric perturbation experiments indicate that both the stratosphere and troposphere determine the predictability of the final warmings. The slopes of the linear regression in the stratospheric and tropospheric experiments are -0.667 and -0.674, which are indistinguishable.

Fig. 5.8 shows the perturbation experiments for the two late final warmings. The total perturbation results are consistent with Fig. 5.7 and show a slope of -1. The stratospheric and tropospheric perturbation experiments, however, indicate that the stratospheric initial conditions barely determine the timing of the final warmings. Instead, most of predictability comes from the troposphere.

Fig. 5.9 shows the perturbation experiments for two middle final warming events. The total perturbation results are still the same as for the late final warmings. The stratospheric and tropospheric perturbation results, however, are different from the late ones and similar

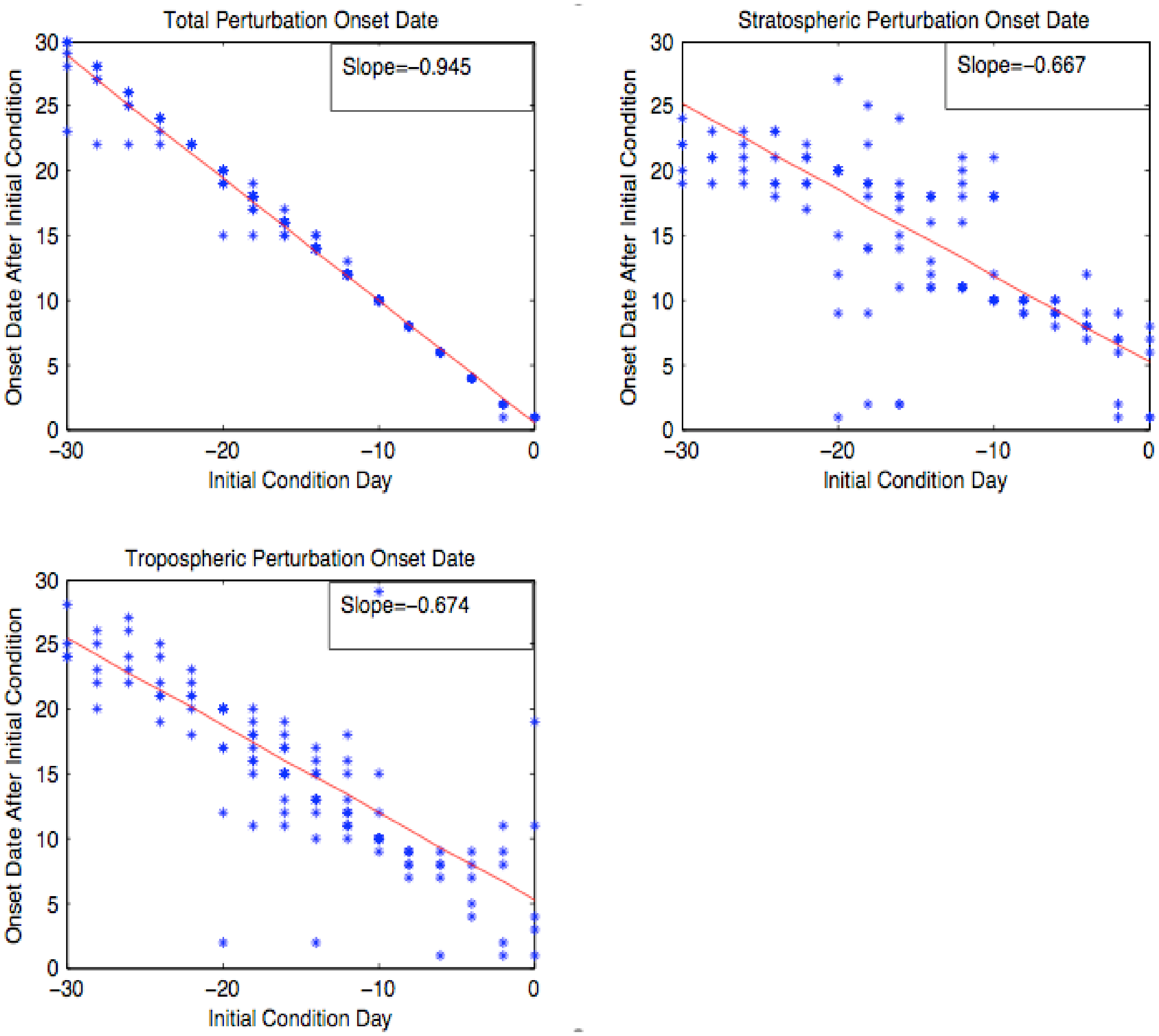

Figure 5.7: Perturbation experiments for the six final warming events. The xaxis is the time of the perturbation field (from day -30 to day -10 for day -20 initial condition; day -20 to day 0 for day -10 initial condition). The yaxis is the time of the onset date for the perturbation run, defined as the days after the initial condition. The red line is the linear regression of the points.

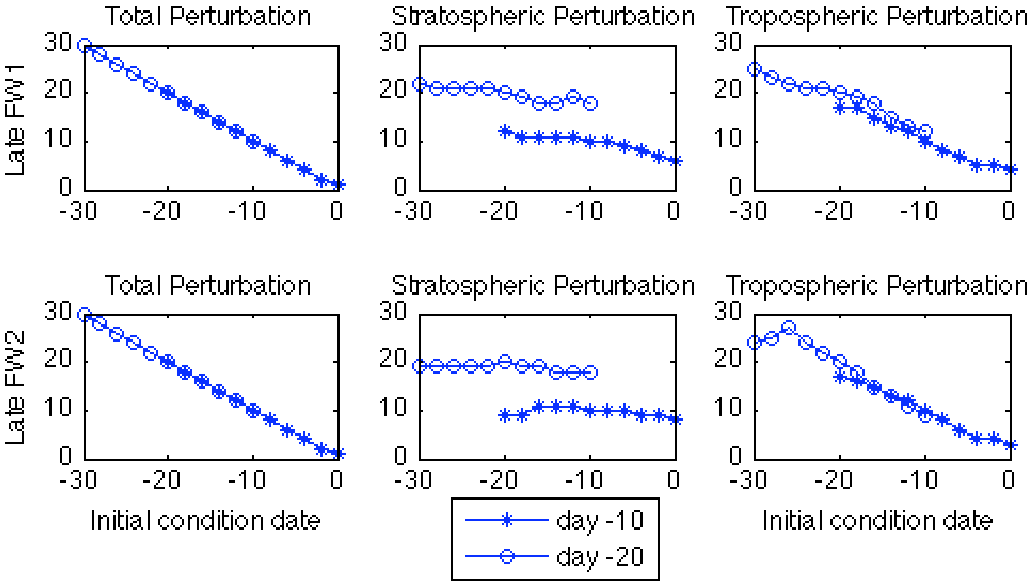

Figure 5.8: Perturbation experiments for the late final warming events.

to the sudden warming results. More than 4 days before the onset, the troposphere begins to contribute to the predictability of the final warming. The stratosphere seems to have a larger effect in determining the predictability than in the sudden warming. Even for the day -20 initial condition, the first final warming results also show some slopes less than 0. And for the day -10 initial condition, stratosphere can determine the predictability up to 15 days before the onset in the second final warming event.

The perturbation experiment results for the early final warmings are shown in Fig. 5.10. The slope of the total perturbation experiments is still near -1, but it is noticed that many final warmings do not occur. This reflects that occurrence of an early final warming is very sensitive to the initial conditions. This is similar to the shallow sudden warming cases. From these few points in the stratospheric and tropospheric experiments, it is hard to see any clear trend, but the near-0 slope suggest that their effect on the predictability of the early final warmings are limited.

Zonal-mean, long-wave and short-wave perturbation experiments are also performed for one early, one middle and one late final warming event. They do not give a good linear trend except that near the final warming onset the zonal and long waves play some roles for

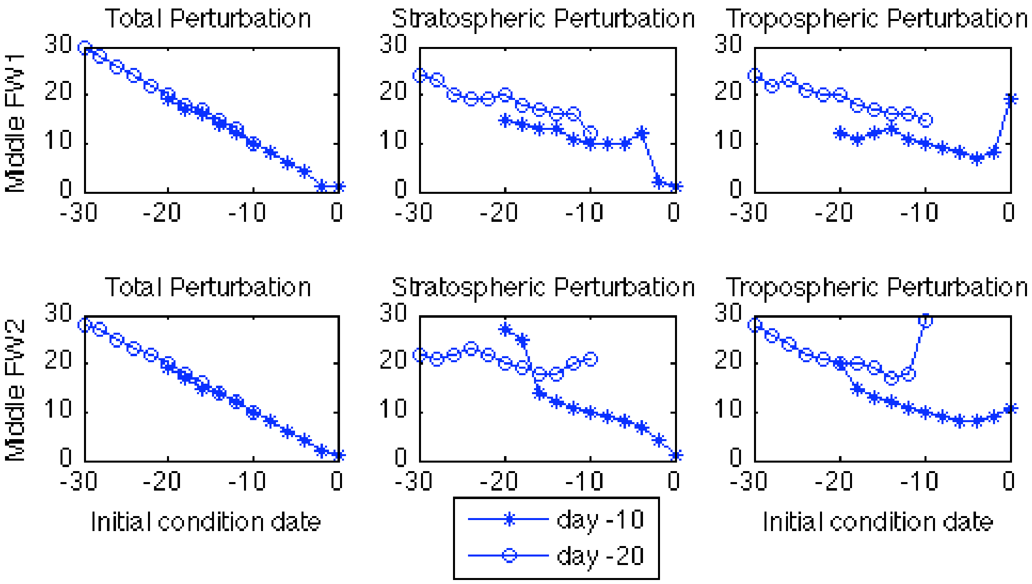

Figure 5.9: Perturbation experiments for two middle final warming events.

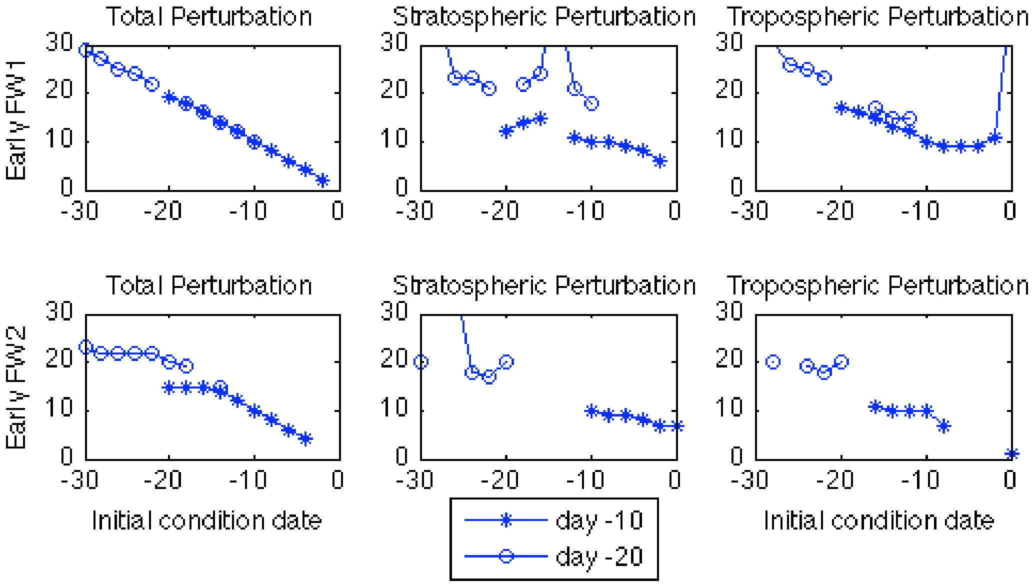

Figure 5.10: Perturbation experiments for two early final warming events.

the late and middle final warmings. Most of the early final warmings do not occur in the perturbation experiments.

5.5 Discussion and conclusion

The perturbation experiments for the sudden and final warmings reveal how the stratosphere and troposphere determine the predictability of the stratospheric warming events. For both deep and shallow sudden warmings, the timing of the sudden warming is approximately independent of the stratospheric initial condition more than 20 days before the onset time, but depends more on the stratospheric initial condition when the onset time is closer. This implies that the predictability of the sudden warming does not come from the stratosphere, except near the onset time. On the other hand, the tropospheric experiments suggest that predictability comes from the troposphere most of the time except very close to the onset time. Since the sudden warming is caused by the tropospheric planetary waves, it is not surprising that tropospheric initial conditions can determine the timing of the sudden warmings. Near the onset of the sudden warming, however, the stratospheric may already reach some "preconditioned" state, in which and stratosphere has more influence on the subsequent evolution.

The experiments for the final warmings are more complex than the sudden warmings, because temporal changes in the diabatic heating are involved. Since we use the 50 hPa instead of 10 hPa, to define the final warming, the tropospheric perturbations more readily affect the timing of the final warming. The experiments for late final warmings give the striking result that almost all of the predictability comes from the troposphere. The results for the middle final warmings resemble the deep sudden warmings, while the results for early final warming are similar to these for shallow sudden warmings.

Both the sudden and final warming experiments suggest the important role of troposphere in determining the predictability of stratospheric warmings. For the late final warmings, although the planetary waves are already absent in the middle and upper stratosphere, tropospheric planetary waves can still penetrate the lower stratosphere, decelerate the zonal winds and trigger the final warming. The sudden warming and middle final warming results are similar, in that the stratosphere has a larger impact on the predictability at times close to the onset of the warmings. At longer time before the onset, however, the troposphere is still more effective than the stratosphere in determining the predictability.

The early final warmings are very sensitive to both the stratospheric and tropospheric initial conditions, similar to the results for shallow sudden warmings. This can be understood in this way: the occurrence of an early final warming is similar to the sudden warming, but with a more restrictive condition than the sudden warming, that the zonal wind at 50 hPa reverses sign. The classic wave-mean flow interaction theory tells us that the zonal wind in the upper stratosphere first reverses sign, then the zero wind lines descend into the lower stratosphere. Thus, only those signals with very strong waves can extend the zero wind line to 50 hPa and trigger a final warmings. This explains why many warmings do not occur in early final warming perturbation experiments. It is expected that if the perturbation experiments are carried out at 10 hPa (also adopting a 10-hPa final warming definition), the early final warming perturbation results will better resemble the deep sudden warmings.

In order to test our expectation, the same perturbation experiments are performed for two early final warming events, but using a definition for the final warmings in terms of 10-hPa wind. Then the final warming necessarily becomes deeper. The results are shown in Fig. 5.11. It becomes more likely for the final warming to occur than when the 50-hPa definition is used. Two similar structures to the sudden warmings are seen: 1) Close to the onset time, the stratosphere determines the predictability of the final warmings. 2) At longer before the warming events, the troposphere is more important in triggering the warmings.

Based on the previous discussion, we find that due to the different roles of the planetary waves and diabatic heating in the stratosphere, the dominant factors determining the predictability of the final warmings are also different. The occurring of the late final warming comes primarily from the contribution of the troposphere. The early and middle final warming is more like the sudden warming, for which stratosphere is important determining

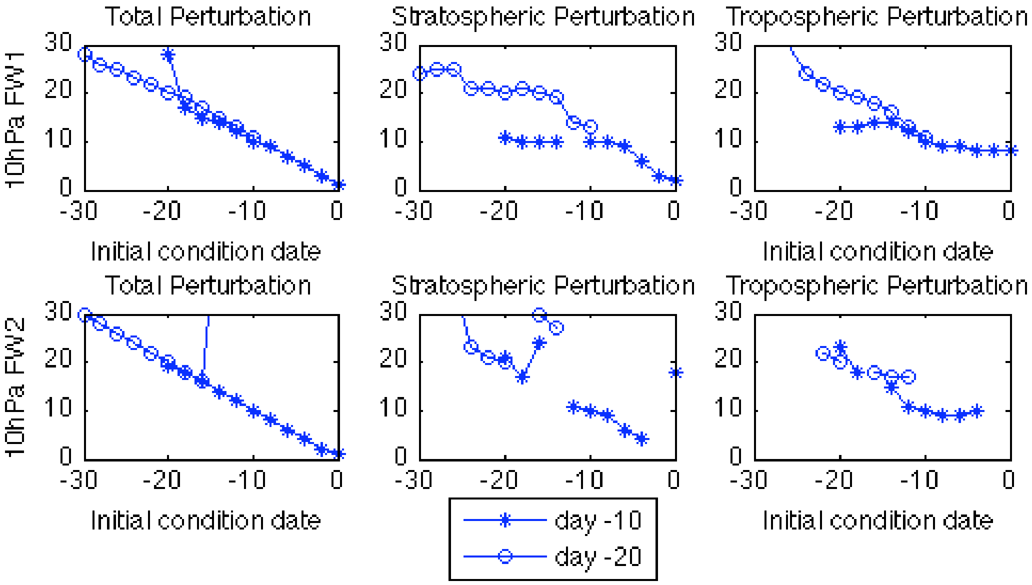

Figure 5.11: As in Fig. 5.10, but the final warming is defined at 10 hPa.

the predictability close to the onset date, while the troposphere is more important earlier. Our predictability studies indicate that the troposphere is important in determining the predictability of the stratospheric sudden and final warming events. The tropospheric precursors, whether for the final warmings or sudden warmings (e.g. the tropospheric blocking in Martius et al. (2009)), are the keys to understand and to make better predictions of stratospheric warming events.

Chapter 6

WACCM final warming analysis

6.1 Introduction to WACCM

In the previous chapters, an idealized dynamical core model has been used to simulate final warming events with different topographic forcing and vortex strengths. The main features of final warmings with strong (weak) topographic forcing resemble the Northern (Southern) Hemisphere observations. Due to the simplicity of the dynamical core model, however, we cannot expect the results to be exactly the same as our current climate; this model is more appropriate for mechanistic studies intended to produce dynamical understanding. In addition, without considering the complex chemical compositions of the atmosphere and their transport, the dynamical core model cannot simulate the changes in the climate systems, such as ozone depletion and recent climate change due to the emissions of greenhouse gases. In order to get more realistic results, a complete global climate model is needed. A complete climate model incorporates almost all of the important processes within the climate system and can give a more realistic simulation. Here we use the Whole-Atmosphere Community Climate Model (WACCM) as an example to look at the final warming events and their dynamics.

WACCM3 is based on the new version of the NCAR Community Atmospheric Model 3 (CAM3), including all the physical parameterizations in that model. Interactive chemistry package in WACCM3 is from the three-dimensional chemical transport Model for Ozone and Related chemical Tracers (MOZART), which includes the chemistry and transport of 51 neutral species. Long-wave and short-wave heating formulations are from CAM3. A suite of long-wave parameterization is added, however, for modeling the mesosphere and lower thermosphere, and at altitudes higher than 70 km additional treatments of short-wave radiations are included. In addition to the long-wave and short-wave radiation computation for high altitudes, an auroral parameterization, based on NCAR's Thermosphere Ionosphere Mesosphere Electrodynamics General Circulation Model (TIME-GCM), is incorporated in WACCM3. The effects of momentum forcing by ion drag and of Joule heating associated with electric fields are implemented. Molecular diffusion, which is more important above the middle atmosphere, is also included in WACCM3. This model incorporates a parameterization for a spectrum of vertically propagating internal gravity waves. Both the orographic and spectral components of the parameterization take into account the rapid increase with altitude of molecular diffusion, which leads to diffusive separation and becomes the principal dissipation mechanism for upward propagating waves. Detailed discussion of the physical processes and parameterizations in WACCM3 can be found in Sassi et al. (2003) and Richter et al. (2008).

WACCM3 has a finite volume dynamical core. It has 66 vertical levels from the ground to 4.5×10^{-6} hPa (about 145 km). Above 100 hPa, the vertical coordinate is purely isobaric, but is hybrid below that level. The vertical resolution is 3.5 km above about 65 km, 1.75 km around the stratopause (50 km), 1.1 – 1.4 km in the lower stratosphere (below 30 km), and 1.1 km in the troposphere. The horizontal resolution for this run is $4^o \times 5^o$ (latitude × longitude). The upper boundary condition for momentum and most constituents are the usual zero flux conditions used in CAM3. The temperature at the top boundary changes as a function of the season and the phase of the solar cycle using results from the Mass Spectrometer-Incoherent Scatter (MSIS) model instead of using zero flux on heat. The Sea-Surface Temperature (SST) data are from the global HadISST dataset prior to 1981 and from the Smith/Reynolds dataset after 1981.

Three realizations of the period 1950 – 2003 trend run are carried out (Two of them are published in the Community Data Portal (CDP)). Our final warming analysis is based on one realization. The variables we use are the zonal wind and sea-level pressure. In this chapter, following the introduction, section 6.2 compares the WACCM climatological zonal wind with NCEP/NCAR reanalysis data. The WACCM final warming evolutions are shown in Section 6.3, followed by the discussion and conclusion.

6.2 Climatological zonal wind variability

The climatological zonal mean zonal winds in December, January, February (DJF) and June, July, August (JJA) are first obtained and compared with the NCEP/NCAR reanalysis data, as shown in Fig. 6.1. The WACCM zonal winds are similar to observations in the Northern Hemisphere, in the Southern Hemisphere, however, they are approximate 10 m s^{-1} larger in the winter. And in the summer of the Southern Hemisphere, the zero-wind line altitude is close to 3 hPa in high-latitudes, in contrast with 50 hPa in observations. In the Northern Hemisphere summer, the zero-wind line altitude in WACCM is again higher than NCEP/NCAR dataset.

The climatological 50-hPa zonal-wind evolutions for WACCM and for the NCEP/NCAR reanalysis are shown in Fig. 6.2. Consistent with Fig. 6.1, the zonal winds in WACCM are always larger in the Southern Hemisphere, especially in the spring of the Southern Hemisphere. Garcia et al. (2007) found that the deficiency of too strong stratospheric zonal winds is most evident in the last two decades of the simulation, when the lower stratosphere is affected by the formation of the ozone hole. The cold temperatures in the high-latitudes of the lower stratosphere, due to the loss of ozone, strengthen the westerlies between 50 and 10 hPa and delay their spring transition. Richter et al. (2010) found this deficiency is connected to the parameterization of gravity waves. After replacing the arbitrarily specified gravity-wave source spectrum with source parameterizations, the middle atmospheric circulation improves. Specifically stratospheric zonal winds in the Southern Hemisphere are weaker. In addition, the frequency of the sudden warming in the Northern Hemisphere increases to 0.6 per year, similar to the Northern Hemisphere observations (Charlton and Polvani, 2006).

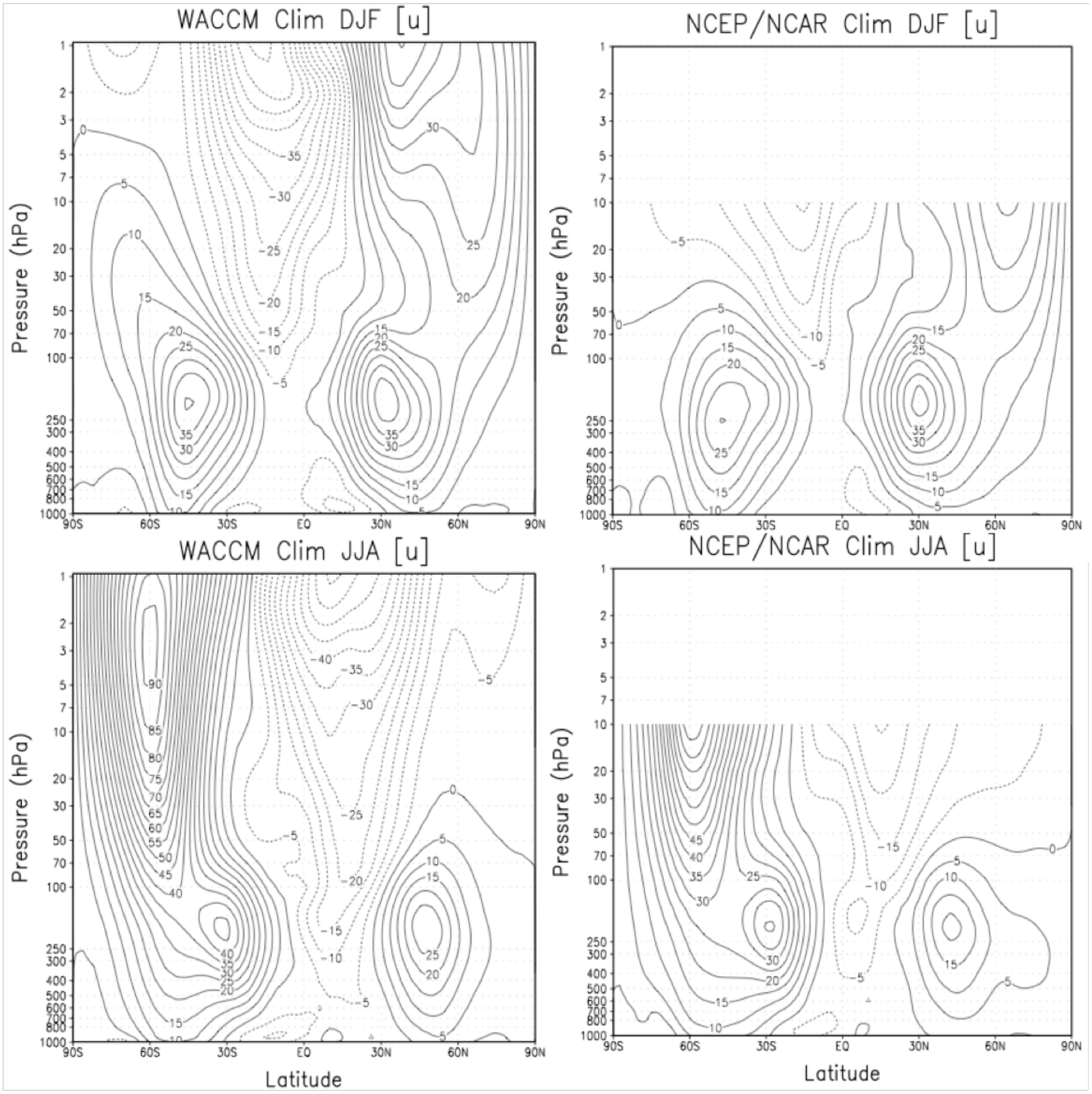

Figure 6.1: Climatological zonal mean zonal wind comparison between WACCM and NCEP/NCAR reanalysis data in December, January, February (DJF) and June, July, August (JJA). The contour interval is 5 m s^{-1}. Note the top of the NCEP/NCAR data is 10 hPa.

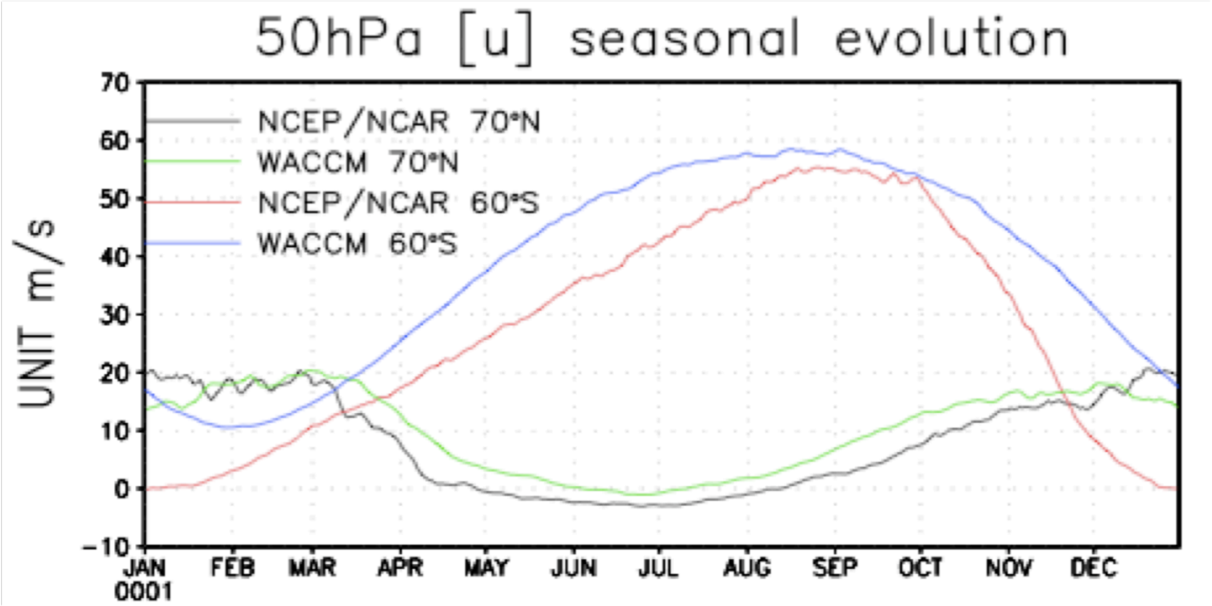

Figure 6.2: Climatological 50-hPa zonal mean zonal wind seasonal transition at 70°N and 60°S for WACCM and NCEP/NCAR reanalysis data.

6.3 Final warming evolutions

6.3.1 Onset dates

Similar to the observational analysis in Black et al. (2006) and Black and McDaniel (2007b), we define the onset of the final warming as the final time that zonal-mean zonal wind at 70^{o}N drops below 0 m s^{-1} without returning to a specific threshold until the fall. By applying the criterion to 5-day average zonal winds at 50 hPa, each onset time of the final warming can be determined. Table 6.1 shows the WACCM mean onset date for both hemispheres. The mean onset date in the Northern Hemisphere is about one month late than the observations. In the Southern Hemisphere, due to the much stronger westerlies in WACCM, if according to 5 m s^{-1} criterion, final warmings do not occur in many years, especially in the last two decades (1983 - 2003). The mean onset time in the Southern Hemisphere is more than 30 days later than in the observations. It takes about 18 days for the zero wind line to descend from 10 hPa to 50 hPa, also much larger than 7 days in the Northern Hemisphere observations.

The WACCM onset dates from 1950 -2003 are shown in Fig. 6.3, together with the observations for comparison. In the NCEP/NCAR reanalysis data, there is a trend toward

	Definition	**10 hPa**	**20 hPa**	**30 hPa**	**50 hPa**
Northern Hemisphere	70°N (0 m s^{-1})	+126	+141	+134	+144[1]
Southern Hemisphere	60°S (0 m s^{-1})	*	*	*	*
Southern Hemisphere	60°S (5 m s^{-1})	*	*	*	*
Southern Hemisphere	60°S (10 m s^{-1})	+182	*	*	*
Southern Hemisphere	60°S (15 m s^{-1})	+176	*	*	*

Table 6.1: WACCM final warming mean onset dates according to different criteria in both hemispheres. * means some final warmings do not occur according to the criterion.

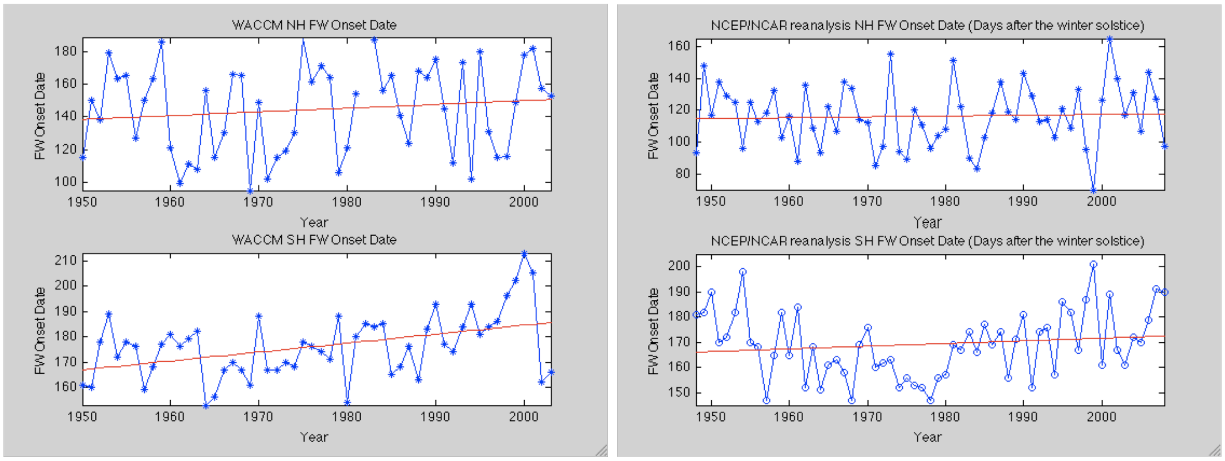

(a) (b)

Figure 6.3: Comparison of final warming onset date evolution between WACCM and NCEP/NCAR reanalysis dataset. The WACCM final warming is from 1950 to 2003, while the NCEP/NCAR reanalysis is from 1948 to 2008. The definition of final warming in the Northern Hemisphere is the same as (Black et al., 2006). In the Southern Hemisphere, NCEP/NCAR final warming adopts 50 hPa 7 m s^{-1} criterion, while WACCM adopts 10 hPa 10 m s^{-1} criterion.

later warming, especially in the Southern Hemisphere where the final warming is at least five day later from 1948 to 2008. A similar trend is found in the WACCM output, with a larger magnitude. From 1950 to 2003, the final warming is about 15 days later in the Northern Hemisphere and about 20 days later in the Southern Hemisphere.

6.3.2 High-latitude zonal wind evolutions

The climatological and composite evolutions of the zonal winds for both hemispheres are shown in Fig. 6.4. Comparing with the NCEP/NCAR final warming results from Black et al. (2006) and Black and McDaniel (2007b), the zonal wind evolutions resemble the observations

---

[1] Note that although according to the 50-hPa 0 m s^{-1} criterion, there is one final warming missing in the Northern Hemisphere in 1982. We still calculate the mean onset date based on others, in order to compare with the observations.

in both hemispheres. The composite evolution is much more abrupt than the climatology in the Northern Hemisphere, while they resemble each other in the Southern Hemisphere. The anomaly evolutions are shown in Fig. 6.5. The patterns are still similar to the observations. In the Northern Hemisphere, coherent zonal wind anomalies extend from the stratosphere downward to the surface. In the Southern Hemisphere, only weak positive and negative anomalies are separated by the onset time, and most of the anomaly signals are confined to the stratosphere. The altitudes of the anomalies in the NCEP/NCAR final warmings are slightly lower than WACCM, but the pattern is similar.

6.3.3 Sea-level pressure evolution in the Northern Hemisphere

In the Northern Hemisphere, similar to the observations, the statistically significant positive (negative) anomalies prior to (after) the onset extend from the stratosphere to the surface. Therefore, it is meaningful to look at how the surface circulation changes across the final warming and compare with the observations. In the Southern Hemisphere, since only marginally significant anomaly signals are observed in the troposphere, the changes in circulation are also weak. Fig. 6.6 (a) (b) shows the sea-level pressure anomalies averaged over day -20/-10 and day +5/+10 in the Northern Hemisphere. Similar to the 1000-hPa geopotential height observations by Black et al. (2006), day -20/-10 and day +5/+10 sea-level pressure anomalies are characterized by similar but oppositely signed patterns. Prior to the final warming, there are negative anomalies in the polar region with the two positive anomalies in the Pacific and Atlantic regions. After that, the dipole pattern remains, with the positive anomalies in the high-latitudes and negative anomalies in the Atlantic and northeast of Europe. The difference between WACCM and Northern Hemisphere observations is in the Atlantic region: the positive sea-level pressure anomalies in WACCM prior to the final warming are not as strong as the Pacific region, but the negative anomalies after the final warming onset are very strong, and the whole dipole pattern is a typical NAO pattern.

The composite sea-level pressure changes in Fig.6.6 (c) indicate that as the final warming approaches, the sea-level pressure increases in the polar region and decreases in the Atlantic

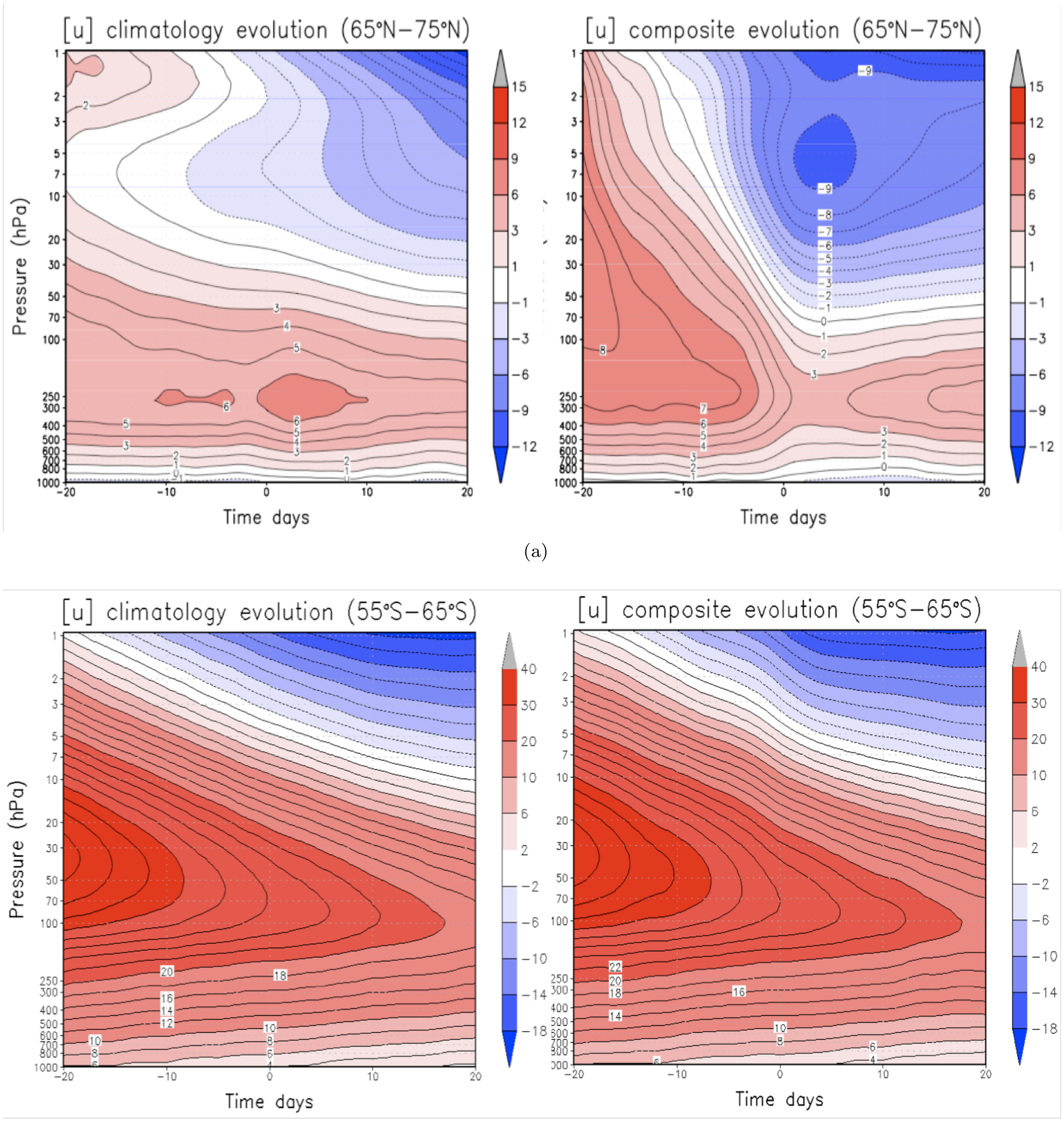

(a)

(b)

Figure 6.4: Climatological and composite time evolutions of the zonal wind averaged over (a) 65°N - 75°N in the Northern Hemisphere and (b) 55°S - 65°S in the Southern Hemisphere for the WACCM final warming events. 50 hPa 0 m s^{-1} criterion is used to define the final warming onset in the Northern Hemisphere, 10 hPa 10 m s^{-1} criterion is used to define the final warming onset in the Southern Hemisphere. The contour interval is 1 m s^{-1} in the Northern Hemisphere and 2 m s^{-1} in the Southern Hemisphere.

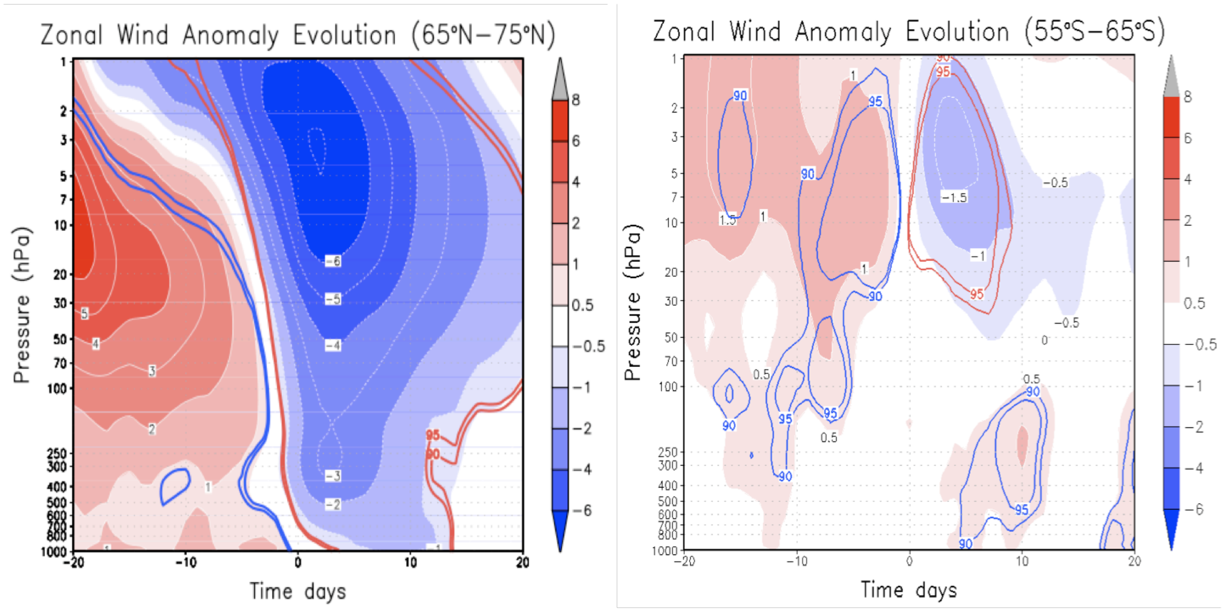

(a)

(b)

Figure 6.5: Time evolutions of the anomalous zonal wind averaged over (a) 65°N - 75°N in the Northern Hemisphere and (b) 55°S - 65°S in the Southern Hemisphere for the WACCM final warming events. Colored contours indicate the 90% and 95% confidence levels from a two-sided Student's t-test.

and Pacific regions, similar to the typical AO/NAO pattern. The climatological changes, however, show a different pattern, characterized by the decrease over the extratropical continents and increase over the oceans, due to the asymmetry in heating between them. The typical Northern Hemisphere winter has two semi-permanent lower-pressure centers: Aleutian Low and Iceland Low with the high-pressure center in the northern regions of Asia and North America. In the spring, when the solar radiation heats the surface asymmetrically, the warming continent and still-cooling ocean will cause these pressure-centers to weaken, which is what we observed in the climatological sea-level pressure changes. This difference between the composite and climatology is similar to the observations and reflects the fact that the stratospheric influence in the final warmings is not well expressed in the climatology. It also suggests that the spring transition in the troposphere is not characterized only by the asymmetry in heating due to the solar radiation, but also affected by the influences downward from the stratosphere.

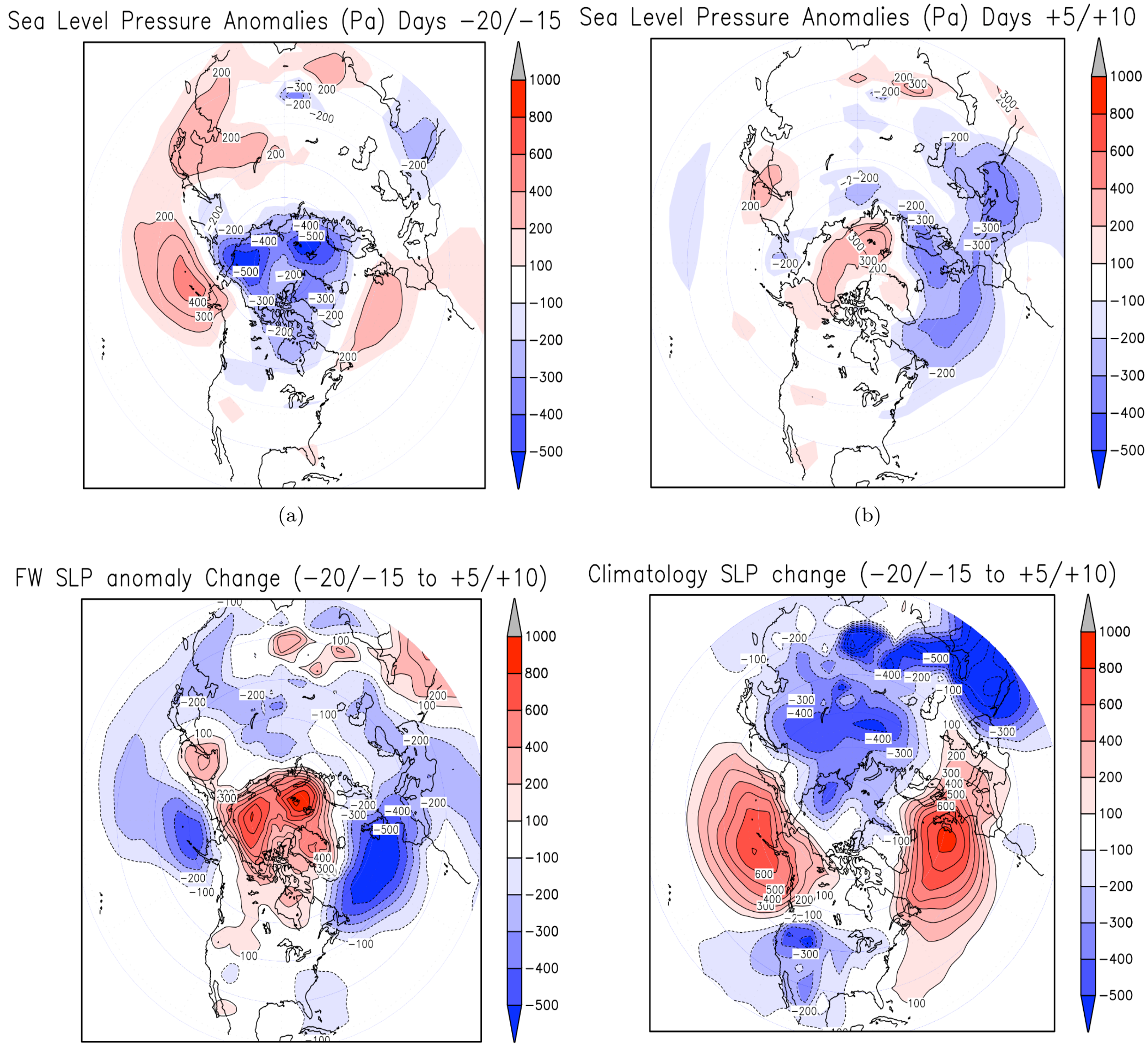

(a)

(b)

(c)

(d)

Figure 6.6: Composite sea-level pressure anomalies averaged over (a) day -20/-15 and (b) day +5/+10 with respect to the final warming onset in the Northern Hemisphere. (c): Composite sea-level pressure anomaly changes from day -20/-15 to day +5/+10. (d) Climatological sea-level pressure changes within the period of (c). The contour interval is 100 Pa.

6.3.4 Summary and discussion

In this chapter, results from the WACCM 1950 - 2003 trend run are used to analyze the final warmings in both hemispheres. Comparing with the dynamical core model results, WACCM can simulate the stratospheric cooling trend due to ozone depletion, and the resulting trend in the timing of the final warmings. In addition, since WACCM considers the tropospheric seasonal transition, the tropospheric zonal wind evolution is more realistic. For example, in the Southern Hemisphere, there are clear zonal-wind decelerations across the final warmings due to the tropospheric seasonal transition, but these are much weaker in the dynamical core model. These deceleration signals are from the tropospheric seasonal transitions and have almost the same magnitudes for the climatology and composite, so that they disappear in the anomaly fields. This suggests that in reality, the tropospheric spring transition is controlled by two factors: tropospheric thermal forcing, and the stratospheric influence. When the tropospheric topographic forcing is weak (Southern Hemisphere), the transition is mostly controlled by the troposphere itself. When the forcing is stronger (Northern Hemisphere), however, the stratospheric influence becomes much more important.

The simplicity of the dynamical core comparing with the WACCM, such as the absence of some physical parameterizations, might also lead to some differences in the final warming results. Changes in orographic gravity waves have been found to be primarily responsible for the projected strengthening of Brew-Dobson circulation in the Northern Hemisphere (Li et al., 2008). Gravity wave parameterizations are incorporated in WACCM, but not in the dynamical core. This might have an impact on the simulation of the final warming events.

In short summery, although WACCM has zonal winds that are too strong in the spring, which causes the mean onset dates to be delayed at least one month with respect to the observations, the zonal wind evolutions resemble the observations in both hemispheres. In Chapter 3, we obtained similar zonal wind evolutions in the dynamical core model, so the similarity between the models and observations suggests that the downward influence of the stratospheric final warming on the tropospheric circulation is real and substantial, especially in the Northern Hemisphere.

Chapter 7

Conclusions

In this thesis, we use an idealized dynamical core model to investigate the downward influence of the stratospheric final warming on the tropospheric circulation. The goal of our study is to understand the dynamical coupling between the stratosphere and troposphere during the stratospheric final and sudden warmings. The contributions of our work to atmospheric science can be summarized as follows:

First, we perform a clean test of the hypothesis that much of the observed tropospheric signal in the final warming is initiated from the stratosphere. Before our work, most studies of downward influence focused on the wintertime intraseasonal polar vortex breaking (sudden warming) and strengthening (e.g. Baldwin and Dunkerton (2001); Limpasuvan et al. (2004, 2005)). These events are closely connected to the propagation of wave activity, and diabatic processes are less important. Although observations of the Northern Hemisphere final warmings suggested that the stratosphere makes a significant contribution to the springtime transition in the lower troposphere (Black et al., 2006), it is impossible using observations to unambiguously separate the stratospheric influence from that controlled by tropospheric processes alone. Thus our understanding of the downward influence during the final warming is limited. In this modeling study, by fixing the tropospheric equilibrium temperature and imposing the thermal forcing to induce a springtime transition - a final warming - only in the stratosphere, the resulting tropospheric changes are then unquestionably attributed to the stratospheric final warming, and the stratospheric downward influence on the tropospheric circulation is readily observed. Large ensembles of simulated final warmings indicate that with sufficient topographic forcing the stratospheric anomaly signals across the final warming can coherently extend downward to the surface, similar to the Northern Hemisphere observations. These results suggest that a substantial fraction of the observed tropospheric changes that occur in conjunct with the final warming are induced from the stratosphere. This further implies that the role of the stratosphere in the climate, and more practically, the value of including a well-resolved stratosphere in climate models, should be considered in the context of the full seasonal cycle. Fixing the tropospheric T_{eq} can help us to test our hypothesis, but without the tropospheric seasonal transition, it is hard to compare the tropospheric transition due to stratospheric influence with that due only to the tropospheric seasonal transition. In our continuing research, final warming runs with the seasonal transition only in the troposphere, and in the whole stratosphere and troposphere can be carried out. Comparisons among three simulations can help us to understand how much of the tropospheric change in the final warming is due to stratospheric influence, and how much is due only to the tropospheric seasonal transition. We can also see if there are nonlinear interactions between these two processes.

Secondly, by diagnosing the tropospheric response to the stratospheric final warming, we find that when the planetary waves are sufficiently strong, they are crucial in determining the downward influence of the final warming. Previous downward influence studies often emphasize the importance of the residual circulation induced by stratospheric wave driving (Haynes et al., 1991) and tropospheric synoptic-eddy feedback (Kushner and Polvani, 2004) in the downward influence processes. Song and Robinson (2004) found that the planetary waves can also transmit the stratospheric signals to the troposphere. They suggested that the role of planetary waves in coupling the troposphere to the stratosphere would increase in importance in the presence of strong planetary waves. In this study, we simulate the final warming with sufficient topographic forcing so that there are strong planetary waves. We find that, unlike the previous studies, the tropospheric synoptic-eddy feedback is not important in the downward influence of final warmings. One reason is the decorrelation time of the annular mode becomes shorter in the presence of topography or other stationary wave forcing (Gerber et al., 2008). This implies a weak transient-eddy feedback. Moreover, the responses of Song and Robinson (2004); Kushner and Polvani (2004) are both in steady state simulations, while the final warming is a transient event. As a transient event, the final warming might not allow enough time for the synoptic eddies to respond systematically, so that the mechanism of the tropospheric eddy feedback is much weaker in the presence of topography. Results from our zonally symmetric model clearly indicate that it is the tropospheric planetary waves that amplify near the final warming and cause the tropospheric zonal wind to respond to the stratospheric transition. This reflects the important roles of planetary waves in the downward influence of stratospheric final warmings. It suggests that the mechanisms associated with the planetary wave propagation, including wave reflection (Perlwitz and Harnik, 2003, 2004), wave trapping (Chen and Robinson, 1992; Black and McDaniel, 2007a), and wave resonance (Plumb, 2009), may be more important, and therefore motivates a continued effort to understand the essence of tropospheric planetary wave amplifications during the final warmings. In our further research, the mechanism of the tropospheric planetary wave amplification will be investigated. Since, in our model, wave number 1 is most important in determining the downward influence, a wave-1 model can be used to re-simulate the final warming. In the full model, the wave number 1 forcing comes from two sources: topographic forcing and the wave-wave interactions from higher wave numbers. In the wave-1 model, the latter contribution can be calculated as a residual in the wave-1 equation and averaged over time, from the full model. This can give a better simulation of wave number 1 behavior during the final warmings and allow us to study the mechanisms associated with wave amplification.

Thirdly, we find the troposphere can be very important in determining the predictability of the stratospheric sudden and final warmings. Previous observational studies have found the timing of the final warming depends strongly on the planetary waves (Waugh et al., 1999; Waugh and Rong, 2002). Modeling studies also revealed the coupled stratosphere-troposphere response to the tropospheric impulse (Reichler et al., 2005; Fletcher et al., 2007; Gerber et al., 2009), however, the stratosphere is not only affected by the tropospheric planetary waves, it has its own internal vacillation. Whether the troposphere or the stratosphere is more important in determining the predictability of the sudden warming is not clear. In the seasonal transition, in which the diabatic heating is involved, such as the final warming, the situation is even more complex. In our study, through a series of perturbation experiments, we test the relative roles of the stratosphere and the troposphere in determining the predictability of stratospheric warmings. For the late final warming, almost all of the predictability comes from the troposphere. For the remaining final warmings and for sudden warmings, however, the troposphere decides the predictability until very close to the time of warming onset. This finding, consistent with the conventional view of the warming, reflects that roles of the troposphere in determining the stratospheric warmings. It suggests that, in order to predict the stratospheric warming, a better tropospheric condition is necessary. It also suggests that more studies of tropospheric precursors are needed. Recent studies (Martius et al., 2009; Colucci, 2009) have found connections between sudden warmings and tropospheric blocking, but the dynamical mechanism is still not well understood. In our model, with sufficient topographic forcing, the sudden warming occurs frequently, as does tropospheric blocking, so we can continue to study the interactions between them and expect to understand more about the dynamics of their connections.

Overall, in this thesis, our idealized final warming modeling results are supported by observations and are also consistent with the conventional view of stratosphere-troposphere coupling. They help us to understand the mechanisms of the stratospheric final warming and sudden warming, and their downward influence on the tropospheric circulation.

Appendix

A: TEM equations in σ and spherical coordinates

From Holton (2004), we know the momentum, thermodynamic and continuity equations under the σ and spherical coordinates are:

$$\frac{\partial u}{\partial t} = -A(u) + fv + \frac{uv\tan\phi}{a} - \frac{1}{a\cos\phi}\frac{\partial\Phi}{\partial\lambda} - \frac{RT}{a\cos\phi}\frac{\partial\ln P_s}{\partial\lambda} \tag{.1}$$

$$\frac{\partial v}{\partial t} = -A(v) - fu - \frac{u^2\tan\phi}{a} - \frac{1}{a}\frac{\partial\Phi}{\partial\phi} - \frac{RT}{a}\frac{\partial\ln P_s}{\partial\phi} \tag{.2}$$

$$\frac{\partial T}{\partial t} = -A(T) + \frac{\kappa T\omega}{p} + Q \tag{.3}$$

$$\frac{\partial P_s}{\partial t} = -\frac{1}{a\cos\phi}\frac{\partial P_s u}{\partial\lambda} - -\frac{1}{a\cos\phi}\frac{\partial P_s v\cos\phi}{\partial\phi} - \frac{\partial P_s\dot{\sigma}}{\partial\sigma} \tag{.4}$$

where

$$A(x) = \frac{u}{a\cos\phi}\frac{\partial x}{\partial\lambda} + \frac{v}{a}\frac{\partial x}{\partial\phi} + \dot{\sigma}\frac{\partial x}{\partial\sigma}$$

In the GFDL spectral model, the diabatic heating is parameterized by Newton cooling so that $Q = -(T - T_{eq})/\tau$. κ is the ratio of the gas constant to the heat capacity at constant pressure and

$$\frac{\omega}{p} = \frac{\dot{\sigma}}{\sigma} + (v - \tilde{v})\cdot\nabla\ln P_s - D$$

where ω is the pressure vertical velocity, p is the pressure, $\dot{\sigma}$ is the σ vertical velocity, D is the divergence. The tilde represents vertical averages. a is the radius of the Earth and P_s is the surface pressure.

Now we first compute the time derivative of $P_s u$ and substitute (.1) and (.4) into it, so that

$$\begin{aligned}\frac{\partial P_s u}{\partial t} &= u\frac{\partial P_s}{\partial t} + P_s\frac{\partial u}{\partial t} \\ &= -\frac{1}{a\cos\phi}\frac{\partial(P_s u^2)}{\partial\lambda} - \frac{1}{a\cos\phi}\frac{\partial(P_s vu\cos\phi)}{\partial\phi} - \frac{\partial(P_s\dot{\sigma}u)}{\partial\sigma} \\ &\quad + fP_s v + \frac{P_s vu\tan\phi}{a} - \frac{P_s}{a\cos\phi}\frac{\partial\Phi}{\partial\lambda} - \frac{RT}{a\cos\phi}\frac{\partial P_s}{\partial\lambda} \qquad (.5)\end{aligned}$$

We do zonal mean for equation (.5) and substitute equation (.4) into it, so that

$$\begin{aligned}\frac{\partial\overline{P_s u}}{\partial t} &= \overline{P_s}\frac{\partial\bar{u}}{\partial t} + \bar{u}\frac{\partial\overline{P_s}}{\partial t} + \frac{\overline{P_s' u'}}{\partial t} \\ &= \overline{P_s}\frac{\partial\bar{u}}{\partial t} + \frac{\overline{P_s' u'}}{\partial t} - \frac{\bar{u}}{a\cos\phi}\frac{\partial(\overline{P_s v}\cos\phi)}{\partial\phi} - \bar{u}\frac{\partial(\overline{P_s\dot{\sigma}})}{\partial\sigma} \\ &= -\frac{1}{a\cos\phi}\frac{\partial(\overline{P_s vu\cos\phi})}{\partial\phi} - \frac{\partial(\overline{P_s\dot{\sigma}u})}{\partial\sigma} \\ &\quad + f\overline{P_s v} + \frac{\overline{P_s vu}\tan\phi}{a} - \frac{1}{a\cos\phi}\overline{P_s\frac{\partial\Phi}{\partial\lambda}} - \frac{1}{a\cos\phi}\overline{RT\frac{\partial P_s}{\partial\lambda}}\end{aligned}$$

then we could get that

$$\begin{aligned}\overline{P_s}\frac{\partial\bar{u}}{\partial t} + (\overline{P_s v})\Big(\frac{1}{a\cos\phi}\frac{\partial(\bar{u}\cos\phi)}{\partial\phi} - f\Big) + (\overline{P_s\dot{\sigma}})\frac{\partial\bar{u}}{\partial\sigma} &= -\frac{1}{a\cos^2\phi}\frac{\partial[\overline{(P_s v)' u'}\cos^2\phi]}{\partial\phi} - \frac{\partial\overline{(P_s\dot{\sigma})' u'}}{\partial\sigma} \\ &\quad - \frac{1}{a\cos\phi}\overline{P_s'\frac{\partial\Psi'}{\partial\lambda}} - \frac{\partial(\overline{P_s' u'})}{\partial t} \qquad (.6)\end{aligned}$$

where $\Psi = \Phi - RT$.

In a similar way, we could obtain the other zonal mean momentum and thermodynamics equations as follows:

$$\begin{aligned}\overline{P_s}\frac{\partial\overline{v}}{\partial t} + \overline{P_s u}\Big(f + \frac{\bar{u}\tan\phi}{a}\Big) + \frac{\overline{P_s v}}{a}\frac{\partial\overline{v}}{\partial\phi} + (\overline{P_s\dot{\sigma}})\frac{\partial\overline{v}}{\partial\sigma} &= -\frac{1}{a\cos\phi}\frac{\partial[\overline{(P_s v)' v'}\cos\phi]}{\partial\phi} - \frac{\partial\overline{(P_s\dot{\sigma})' v'}}{\partial\sigma} \\ &\quad - \frac{\overline{(P_s u)' u'}}{a}\tan\phi - \frac{1}{a}\frac{\partial}{\partial\sigma}\overline{[(P_s\sigma)'\frac{\partial\Phi'}{\partial\phi}]} \\ &\quad - \frac{\partial(\overline{P_s' v'})}{\partial t} \qquad (.7)\end{aligned}$$

$$\overline{P_s}\frac{\partial\overline{T}}{\partial t} + \frac{\overline{P_s v}}{a}\frac{\partial\overline{T}}{\partial\phi} + (\overline{P_s\dot{\sigma}})\frac{\partial\overline{T}}{\partial\sigma} - \kappa\overline{P_s(\frac{\omega}{p})}\overline{T} = -\frac{1}{a\cos\phi}\frac{\partial[\overline{(P_s v)'T'\cos\phi}]}{\partial\phi} - \frac{\partial\overline{(P_s\dot{\sigma})'T'}}{\partial\sigma}$$
$$+\,\kappa\overline{[P_s(\frac{\omega}{p})]'T'} + \overline{P_s Q} - \frac{\partial(\overline{P_s'T'})}{\partial t} \qquad (.8)$$

$$\frac{\partial\overline{P}_s}{\partial t} = -\frac{1}{a\cos\phi}\frac{\partial(\overline{P_s v}\cos\phi)}{\partial\phi} - \frac{\partial\overline{P_s\dot{\sigma}}}{\partial\sigma} \qquad (.9)$$

(.6), (.7) (.8) and (.9) are the zonal mean momentum, thermodynamic and continuity equations in σ and spherical coordinates.

Similar to Andrews et al. (1987), we define a mean meridional circulation (0, $\bar{v}^*$, $\bar{\omega}^*$) by

$$\bar{v}^* = \overline{P_s v} - \psi_\sigma$$

$$\bar{\omega}^* = \overline{P_s\dot{\sigma}} + \frac{1}{a\cos\phi}\frac{\partial(\psi\cos\phi)}{\partial\phi}$$

where

$$\psi = \frac{\overline{(P_s v)'\theta'}}{\bar{\theta}_\sigma}$$

The Transformed Eulerian Mean momentum equation becomes,

$$\overline{P_s}\frac{\partial\bar{u}}{\partial t} + \alpha\,\bar{v}^* + \beta\,\bar{\omega}^* = -\nabla\cdot\mathrm{F} - \frac{\partial(\overline{P_s'u'})}{\partial t} \qquad (.10)$$

where

$$\alpha = \frac{1}{a\cos\phi}\frac{\partial(\bar{u}\cos\phi)}{\partial\phi} - 2\Omega\cos\phi$$

$$\beta = \bar{u}_\sigma$$

The Eliassen-Palm flux and its divergence are as follows:

$$\text{Horizontal Eliassen-Palm flux: } \mathrm{F}^{(\phi)} = [\overline{(P_s v)'u'} - \beta\psi]\cos^2\phi$$

$$\text{Vertical Eliassen-Palm flux: } \mathrm{F}^{(\sigma)} = [\overline{(P_s\dot{\sigma})'u'} + \alpha\psi]\cos\phi$$

$$-\nabla\cdot\mathrm{F} = -\frac{1}{\cos\phi}\{\frac{1}{a\cos\phi}\frac{\partial[\mathrm{F}^{(\phi)}]}{\partial\phi} + \frac{\partial[\mathrm{F}^{(\sigma)}]}{\partial\sigma} + \frac{1}{a}\overline{P_s'\frac{\partial\Psi'}{\partial\lambda}}\}$$

Note there is an extra term in the right hand-side of the momentum equation which could not be explained as the divergence of a flux. The residual circulation streamfunction is defined as:

$$\psi^* = \psi \cos\phi - \int \overline{P_s v} \cos\phi d\sigma$$

The continuity equation is still:

$$\frac{\partial \overline{P}_s}{\partial t} = -\frac{1}{a\cos\phi}\frac{\partial(\bar{v}^* \cos\phi)}{\partial\phi} - \frac{\partial\bar{\omega}^*}{\partial\sigma}$$

Appendix

B: Zonally symmetric model

The zonal symmetric version of the GFDL model is derived from the full model and only zonal mean parts of the ζ, D, T and $\ln P_s$ are integrated every time step. Since in the quasi-geostrophic approximation, the dominant terms are the Coriolis term fu and pressure gradient force $\dfrac{\partial\Phi}{\partial y}$ and the scale is about 10^{-3} m s^{-2}, the eddy forcing associated with the y momentum equation only has a scale of 10^{-4} m s^{-2} and its effect on the u is less than 1 m s^{-1}. So in the zonally symmetric model, the eddy forcing in the y momentum equation can be neglected and we only consider the eddy forcing for the u, T and $\ln P_s$ equations, represented by F_u, F_T and $F_{\ln P_s}$, repectively.

From equation (.6) and (.8), we can approximately use the right hand-side as the eddy forcing to drive the zonally symmetric model and the result will be similar to the full model. This did work when topography does not exist. When there is topography, this approximation is not valid because P_s varies a lot for different region. At this time, the model cannot compute the left hand-side of the two equations accurately and the resulting zonal wind pattern will be different from the full model.

We need first break down the terms into separate ones in the left hand-side, e.g. $\overline{P_s u} = \overline{P_s}\bar{u} + \overline{P_s' u'}$ and move the prime terms into right hand-side since the zonally symmetric model cannot get that automatically. Secondly, the σ vertical velocity $\dot{\sigma}$ is diagnosed instead of forecasted every time step, we also need to adjust it to the zonally symmetric model in the left hand-side of the equation (.6) and (.8). The resulting new zonal mean momentum and thermodynamics equations are as follows:

$$\overline{P_s}\frac{\partial\overline{u}}{\partial t}+(\overline{P_s}\overline{v}-f)(\frac{1}{a\cos\phi}\frac{\partial(\overline{u}\cos\phi)}{\partial\phi})+(\overline{P_s}\,\overline{\dot{\sigma}}_{new})(\frac{\partial\overline{u}}{\partial\sigma})=-\frac{\partial(\overline{P_s'u'})}{\partial t}+\overline{P_s}F_u \tag{.1}$$

$$\overline{P_s}\frac{\partial\overline{T}}{\partial t}+\frac{\overline{P_s}\,\overline{v}}{a}\frac{\partial\overline{T}}{\partial\phi}+\overline{P_s}\,\overline{\dot{\sigma}}_{new}\,\frac{\partial\overline{T}}{\partial\sigma}-\kappa\,\overline{P_s}\,\overline{T}\,(\frac{\overline{\dot{\sigma}}_{new}}{\sigma}+\overline{\tilde{v}}\,\frac{\partial\overline{\ln(P_s)}}{\partial y}-\overline{\tilde{D}})=-\frac{\partial(\overline{P_s'T'})}{\partial t}+\overline{P_s}\,F_T \tag{.2}$$

where the $\overline{\dot{\sigma}}_{new}$ is the zonal mean of the σ velocity in the zonally symmetric model. The diagnose equation is

$$\frac{\partial\overline{\dot{\sigma}}_{new}}{\partial\sigma}=-(\overline{v}-\overline{\tilde{v}})\,\frac{\partial\overline{\ln(P_s)}}{\partial y}-(\overline{D}-\overline{\tilde{D}})$$

Since in the zonally symmetric model, the vertical velocity is diagnosed, so we need to do that, too in the left hand-side of the F_u and F_T equation. The F_u and F_T in the right hand-side of the equations are:

$$F_u=\frac{1}{\overline{\overline{P_s}}}\{-\frac{1}{a\cos^2\phi}\,\frac{\partial[\overline{(P_sv)'u'}\cos^2\phi]}{\partial\phi}-\frac{\partial\overline{(P_s\dot{\sigma})'u'}}{\partial\sigma}-\frac{1}{a\cos\phi}\,\overline{P_s'\frac{\partial(\Phi-RT)'}{\partial\lambda}}+G_u\} \tag{.3}$$

$$F_T=\frac{1}{\overline{\overline{P_s}}}\{-\frac{1}{a\cos\phi}\,\frac{\partial[\overline{(P_sv)'T'}\cos\phi]}{\partial\phi}-\frac{\partial\overline{(P_s\dot{\sigma})'T'}}{\partial\sigma}+\kappa\overline{[P_s(\frac{\omega}{p})]'T'}+G_{T_1}+G_{T_2}\} \tag{.4}$$

where

$$G_u=(\overline{P_sv}-\overline{P_s}\,\overline{v})\,(f-\frac{1}{a\cos\phi}\,\frac{\partial(\overline{u}\cos\phi)}{\partial\phi})-(\overline{P_s\dot{\sigma}}-\overline{P_s}\,\overline{\dot{\sigma}}_{new})(\frac{\partial\overline{u}}{\partial\sigma})$$

$$G_{T_1}=-(\overline{P_sv}-\overline{P_s}\,\overline{v})\,\frac{1}{a}\,\frac{\partial(\overline{T})}{\partial\phi})-(\overline{P_s\dot{\sigma}}-\overline{P_s}\,\overline{\dot{\sigma}}_{new})(\frac{\partial\overline{T}}{\partial\sigma})$$

$$G_{T_2}=[\overline{P_s\,(\frac{\dot{\sigma}}{\sigma}+(v-\tilde{v})\cdot\bigtriangledown\ln(P_s)-\tilde{D})}-\overline{P_s}\,(\frac{\overline{\dot{\sigma}}}{\sigma}+(\overline{v}-\overline{\tilde{v}})\,\frac{\partial\overline{\ln(P_s)}}{\partial y}-\overline{\tilde{D}})]\cdot\kappa\overline{T}$$

where the $\overline{\dot{\sigma}}$ is the zonal mean of the σ vertical velocity in the full model, the diagnose equation is

$$\frac{\partial\overline{\dot{\sigma}}}{\partial\sigma}=-\overline{(v-\tilde{v})\cdot\bigtriangledown\ln(P_s)}-(\overline{D}-\overline{\tilde{D}})$$

In addition, when topography exists, we also need to consider the eddy forcing in the

$\ln(P_s)$ equation. Since the zonal mean tendency term is

$$\frac{\partial\overline{\ln(P_s)}}{\partial t} = -\overline{\tilde{v}\cdot\bigtriangledown\ln(P_s)} - \overline{\tilde{D}}$$

we need to consider the zonally symmetric model computation so that we change the equation to

$$\frac{\partial\overline{\ln(P_s)}}{\partial t} + \frac{\overline{\tilde{v}}}{a}\frac{\partial\overline{\ln(P_s)}}{\partial\phi} + \overline{\tilde{D}} = -[\overline{\tilde{v}\cdot\bigtriangledown\ln(P_s)} - \frac{\overline{\tilde{v}}}{a}\frac{\partial\overline{\ln(P_s)}}{\partial\phi}] = F_{\ln P_s} \qquad (.5)$$

In reality, before the zonally symmetric run, F_u, F_T and $F_{\ln P_s}$ are first diagnosed from the full model based on equation (.3), (.4) and (.5), respectively. When running the zonally symmetric model, we transfer F_u, F_T and $F_{\ln P_s}$ into spectral fields (note u forcing will appear in the ζ and D forcing in the spectral field), then add the spectral eddy forcing to the ζ, T and $\ln P_s$ tendency term every time step. The resulting evolution of zonal winds will be very similar to the full model.

References

Andrews, D. G., J. R. Holton, and C. B. Leovy, 1987: *Middle Atmosphere Dynamics*. Academic Press, 489 pp.

Ayarzaguena, B. and E. Serrano, 2009: Monthly characterization of the tropospheric circulation over the Euro-Atlantic area in relation with the timing of stratospheric final warmings. *J. Climate*, **22**, 6313–6324.

Baldwin, M. P. and T. J. Dunkerton, 1999: Propagation of the Arctic Oscillation from the stratosphere to the troposphere. *J. Geophys. Res.*, **104**, 30 937–30 946.

Baldwin, M. P. and T. J. Dunkerton, 2001: Stratospheric harbingers of anomalous weather regimes. *Science*, **104**, 581–584.

Baldwin, M. P., D. B. Stephenson, D. W. J. Thompson, T. J. Dunkerton, A. J. Charlton, and A. O'Neill, 2003: Stratospheric memory and extended-range weather forecasts. *Science*, **301**, 636–640.

Black, R. X., 2002: Stratospheric forcing of surface climate in the Arctic Oscillation. *J. Climate*, **15**, 268–277.

Black, R. X. and B. A. McDaniel, 2004: Diagnostic case studies of the Northern Annular Mode. *J. Climate*, **17**, 1941–1959.

Black, R. X. and B. A. McDaniel, 2007a: The dynamics of Northern Hemisphere stratospheric final warming events. *J. Atmos. Sci.*, **64**, 2932–2946.

Black, R. X. and B. A. McDaniel, 2007b: Interannual variability in the Southern Hemisphere circulation organized by stratospheric final warming events. *J. Atmos. Sci.*, **64**, 2968–2975.

Black, R. X., B. A. McDaniel, and W. A. Robinson, 2006: Stratosphere-troposphere coupling during spring onset. *J. Climate*, **19**, 4891–4901.

Chan, C. J. and R. A. Plumb, 2009: The response to stratospheric forcing and its dependence on the state of the troposphere. *J. Atmos. Sci.*, **66**, 2107–2115.

Charlton, A. J., A. O'Neill, D. B. Stephenson, W. A. Lahoz, and M. P. Baldwin, 2003: Can knowledge of the state of the stratosphere be used to improve statistical forecasts of the troposphere? *Q. J. R. Meteorol. Soc.*, **129**, 3205–3224.

Charlton, A. J. and L. M. Polvani, 2006: A new look at stratospheric sudden warmings. Part I: climatology and modeling benchmarks. *J. Climate*, **20**, 449–469.

Charney, J. G. and P. G. Drazin, 1961: Propagation of planetary scale disturbances from the lower into the upper atmosphere. *J. Geophys. Res.*, **66**, 83–110.

Chen, G. and I. M. Held, 2007: Phase speed spectra and the recent poleward shift of southern hemisphere surface westerlies. *Geophys. Res. Lett.*, **34**, L21 805, doi: 10.1029/2007GL031200.

Chen, G., I. M. Held, and W. A. Robinson, 2007: Sensitivity of the latitude of the surface westerlies to surface friction. *J. Atmos. Sci.*, **64**, 2899–2915.

Chen, P. and W. A. Robinson, 1991: The effects of transience on the propagation of stratospheric planetary waves. *J. Atmos. Sci.*, **48**, 1078–1092.

Chen, P. and W. A. Robinson, 1992: Propagation of planetary waves between the troposphere and stratosphere. *J. Atmos. Sci.*, **49**, 2533–2545.

Christiansen, B., 1999: Stratospheric vacillation in a general circulation model. *J. Atmos. Sci.*, **56**, 1858–1872.

Christiansen, B., 2000: Chaos, quasiperiodicity, and interannual variability: studies of a stratospheric vacillation model. *J. Atmos. Sci.*, **57**, 3161–3173.

Colucci, S. J., 2009: Stratospheric influences on tropospheric systems. *J. Atmos. Sci.*, **67**, 324–344.

Farman, J. C., B. G. Gardiner, and J. D. Shanklin, 1985: Large losses of total ozone in antarctic reveal seasonal cio x/no x interaction. *Nature*, **315**, 207–210.

Farrara, J. D. and C. R. Mechoso, 1986: An observational study of the final warming in the Southern Hemisphere stratosphere. *Geophys. Res. Lett.*, **13**, 1232–1235.

Fletcher, C. G., P. J. Kusher, and J. Cohen, 2007: Stratospheric control of the extratropical circulation response to surface forcing. *Geophys. Res. Lett.*, **34**, L21 802, doi: 10.1029/2007GL031626.

Garcia, R. R., D. R. Marsh, D. E. Kinnison, B. A. Boville, and F. Sassi, 2007: Simulation of secular trends in the middle atmosphere, 1950-2003. *J. Geophys. Res.*, **112**, D09 301.

Gerber, E. P., C. Orbe, and L. M. Polvani, 2009: Stratospheric influence on the tropospheric circulation revealed by idealized ensemble forecasts. *Geophy. Res. Lett.*, **36**, L24 801, doi: 10.1029/2009GL040913.

Gerber, E. P. and L. M. Polvani, 2009: Stratosphere-troposphere coupling in a relatively simple AGCM: The importance of stratospheric variability. *J. Climate*, **22**, 1920–1933.

Gerber, E. P., S. Voronin, and L. M. Polvani, 2008: Testing the Annular Mode autocorrelation timescale in simple atmospheric general circulation models. *Monthly Weather Review*, **136**, 1523–1536.

Gordon, C. T. . and W. F. Stern, 1982: A description of the GFDL global spectral model. *Monthly Weather Review*, **110**, 625–644.

Hardiman, S., 2006: Stratosphere-troposphere coupling. Ph.D. thesis, Cambridge University, 166 pp.

Haynes, P. H., 2005: Stratospheric dynamics. *Annu. Rev. Fluid Mech.*, **37**, 263–293, doi:10.1146/annurev.fluid.37.061903.175710.

Haynes, P. H., C. J. Marks, M. E. McIntyre, T. G. Shepherd, and K. P. Shine, 1991: On the "downward control" of extratropical diabatic circulations by eddy-induced mean zonal forces. *J. Atmos. Sci.*, **48**, 651–678.

Held, I. M. and M. J. Suarez, 1994: A proposal for the intercomparison of the dynamical cores of atmospheric general circulation models. *Bull. Amer. Meteor. Soc.*, **75**, 1825–1830.

Holton, J. R., 2004: *Introduction to dynamic meteorology.* Elsevier Academic Press, 535 pp.

Holton, J. R., P. H. Haynes, M. E. McIntyre, A. R. Douglass, R. B. Rood, and L. Pfister, 1995: Stratosphere-troposphere exchange. *Rev. Geophys.*, **33**, 403–439.

Holton, J. R. and C. Mass, 1976: Stratospheric vacillation cycle. *J. Atmos. Sci.*, **33**, 2218–2225.

Kuroda, K. and K. Kodera, 1999: Roles of planetary waves in the stratosphere-troposphere coupled variability in the Northern Hemisphere winter. *Geophys. Res. Lett.*, **26**, 2375–2378.

Kuroda, Y., 2008: Role of the stratosphere on the predictability of medium-range weather forecast: A case study of winter 2003 -2004. *Geophys. Res. Lett.*, **35**, L19 701, doi:10.1029/2008GL034902.

Kushner, P. J. and L. M. Polvani, 2004: Stratosphere-troposphere coupling in a relatively simple AGCM: The role of eddies. *J. Climate*, **17**, 629–639.

Labitzke, K. G., 1977: Interannual variability of the winter stratosphere in the Northern Hemisphere. *Mon. Wea. Rev.*, **105**, 762–770.

Labitzke, K. G. and H. v. Loon, 1999: *The stratosphere: phenomena, history and relevance.* Springer, 179 pp.

Li, F., J. Austin, and J. Wilson, 2008: The strength of the Brewer-Dobson circulation in a changing climate: Coupled chemistry-climate model simulations. *J. Climate*, **21**, 40–57.

Limpasuvan, V., D. L. Hartmann, D. W. J. Thompson, K. Jeev, and Y. L. Yung, 2005: Stratosphere-troposphere evolution during polar vortex intensification. *J. Geophys. Res.*, **110**, D24 101, doi:10.1029/2005JD006302.

Limpasuvan, V., D. W. J. Thompson, and D. L. Hartmann, 2004: The life cycle of the Northern Hemisphere sudden stratospheric warmings. *J. Climate*, **13**, 2584–2596.

Martius, O., C. Schwierz, and H. C. Davies, 2009: Blocking precursors to stratospheric sudden warming events. *Geophy. Res. Lett.*, **36**, L14 806, doi:10.1029/2009GL038776.

Matsuno, T., 1971: A dynamical model of the stratospheric sudden warming. *J. Atmos. Sci.*, **28**, 1479–1494.

Mattewman, N. J., 2009: A vortex dynamics perspective on stratospheric sudden warmings. Ph.D. thesis, University College London, 326 pp.

O'Neill, A. and B. F. Taylor, 1979: A study of the major stratospheric warming of 1976/77. *Q. J. R. Meteorol. Soc.*, **105**, 71–92.

Perlwitz, J. and N. Harnik, 2003: Observational evidence of a stratospheric influence on the troposphere by planetary wave reflection. *J. Climate*, **16**, 3011–3026.

Perlwitz, J. and N. Harnik, 2004: Downward coupling between the stratosphere and troposphere: The relative roles of wave and zonal mean processes. *J. Climate*, **17**, 4092–4909.

Plumb, R. A., 2009: Planetary waves and the extratropical winter stratosphere. *J. Geophys. Res.*, in press.

Plumb, R. A. and J. Eluszkiewicz, 1999: The Brewer-Dobson circulation: Dynamics of the tropical upwelling. *J. Atmos. Sci.*, **56**, 868–890.

Plumb, R. A. and K. Semeniuk, 2003: Downward migration of extratropical zonal wind anomalies. *J. Geophys. Res.*, **108**, 4223, doi:10.1029/2002JD002773.

Polvani, L. M. and D. W. Waugh, 2003: Upward wave activity flux as a precursor to extreme stratospheric events and subsequent anomalous surface weather regim. *J. Climate*, **17**, 3548–3554.

Polvani, L. M. and D. W. Waugh, 2004: Upward wave activity flux as precursor to extreme stratospheric events and subsequent anomalous surface weather regimes. *J. Climate*, **17**, 3548–3554.

Quiroz, R. S., 1986: The association of stratospheric warmings with tropo- spheric blocking. *J. Geophys. Res.*, **91**, 5277–5285.

Randel, W. J., 1988: The seasonal evolution of planetary waves in the Southern Hemisphere stratosphere and troposphere. *Q. J. R. Meteorol. Soc.*, **114**, 1385–1409.

Randel, W. J., R. Garcia, and F. Wu, 2008: Dynamical balances and tropical stratospheric upwelling. *J. Atmos. Sci.*, **65**, 3584–3595.

Reichler, T., P. J. Kushner, and L. M. Polvani, 2005: The coupled stratosphere-troposphere response to impulsive forcing from the troposphere. *J. Atmos. Sci.*, **62**, 3337–3352.

Richter, J. H., F. Sassi, and R. R. Garcia, 2010: Toward a physically based gravity waves source parameterization in a general circulation model. *J. Atmos. Sci.*, **67**, 136–156.

Richter, J. H., F. Sassi, R. R. Garcia, K. Matthes, and C. A. Fischer, 2008: Dynamics of the middle atmospehre as simulated by the Whole Atmosphere Community Climate Model, version 3 (WACCM3). *J. Geophy. Res.*, **113**, D08 101, doi:10.1029/2007JD009269.

Robinson, W. A., 1991: The dynamics of the zonal index in a simple model of the atmosphere. *Tellus*, **43A**, 295–305.

Robinson, W. A., 1994: Eddy feedbacks on the zonal index and eddy-zonal flow interactions induced by zonal flow transience. *J. Atmos. Sci.*, **51**, 2553–2562.

Robinson, W. A., 1996: Does eddy feedback sustain variability in the zonal index? *J. Atmos. Sci.*, **53**, 3556–3569.

Robinson, W. A., 1997: Dissipation dependence of the jet latitude. *J. Climate*, **10**, 176–182.

Robinson, W. A., 2000: A baroclinic mechanism for the eddy feedback on the zonal index. *J. Atmos. Sci.*, **57**, 415–422.

Sassi, F., B. A. Boville, B. Eaton, R. Garca, and R. G. Roble, 2003: Model description and user guide for waccm1b. *National Center for Atmospheric Research (NCAR)*, http://waccm.acd.ucar.edu/Downloads/WACCM1b.pdf.

Scaife, A. A., J. R. Knight, G. K. Vallis, and C. K. Folland, 2005: Stratospheric vacillations and the major warming over Antarctica in 2002. *Geophys. Res. Lett.*, **32**, L18 715, doi: 10.1029/2005GL023226.

Scherhag, R., 1952: Die explosionsartigen stratospharenerwarmungen des spatwinters 1951/52. *Berichte des Deutschen Wetterdienstes der US-Zone 6*, **38**, 51–63.

Scinocca, J. F. and P. H. Haynes, 1998: Dynamical forcing of stratospheric planetary waves by tropospheric baroclinic eddies. *J. Atmos. Sci.*, **55**, 2361–2392.

Scott, R. K. and P. H. Haynes, 1998: Internal interannual variability of the extratropical stratospheric circulation: the low-latitude flywheel. *Q. J. R. Meteorol. Sco*, **124**, 2149–2173.

Scott, R. K. and P. H. Haynes, 2002: The seasonal cycle of planetary waves in the winter stratosphere. *J. Atmos. Sci.*, **59**, 803–822.

Scott, R. K. and L. Polvani, 2006: Internal variability of the winter stratosphere. Part I: Time independent forcing. *J. Atmos. Sci.*, **63**, 2578–2776.

Scott, R. K. and R. K. Polvani, 2004: Stratospheric control of upward wave flux near the tropopause. *Geophys. Res. Lett.*, **31**, L02 115, doi:10.1029/2003GL017965.

Shaw, T. A., J. Perlwitz, and N. Harnik, 2010: Downward wave coupling between the stratosphere and troposphere: the importance of meridional wave guiding and comparison with zonal-mean coupling. *J. Climate*, submitted.

Song, Y. and W. A. Robinson, 2004: Dynamical mechanisms for stratospheric influences on the troposphere. *J. Atmos. Sci.*, **61**, 1711–1725.

Sun, L. and W. A. Robinson, 2009: Downward influence of stratospheric final warming events in an idealized model. *Geophy. Res. Lett.*, **36**, L03 819, doi:10.1029/2008GL036624.

Taguchi, M., , and S. Yoden, 2002: Internal variability of the tropospherestratosphere coupled system simulated in a simple global circulation model. part ii: Millennium integrations. *J. Atmos. Sci.*, **59**, 3037–3050.

Taguchi, M., 2008: Is there a statistical connection between stratospheric sudden warming and tropospheric blocking events? *J. Atmos. Sci.*, **65**, 1442–1454.

Taguchi, M., T. Yamaga, and S. Yoden, 2001: Internal variability of the tropospherestratosphere coupled system simulated in a simple global circulation model. *J. Atmos. Sci.*, **58**, 3184–3203.

Thompson, D. W. J., J. C. Furtado, and T. G. Shepherd, 2006: On the tropospheric response to anomalous stratospheric wave drag and radiative heating. *J. Atmos. Sci.*, **63**, 2616–2629, doi:10.1175/JAS3771.1.

Thompson, D. W. J. and J. M. Wallace, 2000: Annular modes in the extratropical circulation. Part I: Month-to-month variability. *J. Climate*, **13**, 1000–1016.

Waugh, D. W., W. J. Randel, S. Pawson, P. A. Newman, and E. R. Nash, 1999: Persistence of the lower stratospheric Arctic vortices. *J. Meteo. Soc. Japan*, **104**, 27 191–27 201.

Waugh, D. W. and P. Rong, 2002: Interanual variability in the decay of lower stratospheric arctic vortices. *J. Meteo. Soc. Jap.*, **80**, 997–1012.

WMO, 2006: *Scientific assessment of ozone depletion: 2006*. No. 50, Global ozone research and monitoring project, Geneva, Switzerland.

Yoden, S., 1987: Bifurcation properties of a stratospheric vacillation model. *J. Atmos. Sci.*, **44**, 1723–1733.